

Structure-property Relationships of Ligand-protected Metal Nanoclusters

by

Michael James Cowan

MEng Chemical Engineering, University at Buffalo, 2016

BS Chemistry, Binghamton University, 2015

Submitted to the Graduate Faculty of
the Swanson School of Engineering in partial fulfillment
of the requirements for the degree of

Doctor of Philosophy

University of Pittsburgh

2022

UNIVERSITY OF PITTSBURGH
SWANSON SCHOOL OF ENGINEERING

This dissertation was presented

by

Michael James Cowan

It was defended on

December 15, 2021

and approved by

Giannis Mpourmpakis, PhD, Associate Professor, Chemical and Petroleum Engineering

Jill Millstone, PhD, Professor, Chemical and Petroleum Engineering

Christopher Wilmer, PhD, Associate Professor, Chemical and Petroleum Engineering

Rongchao Jin, PhD, Professor, Chemistry, Carnegie Mellon University

Dissertation Director: Giannis Mpourmpakis, PhD, Associate Professor, Chemical and
Petroleum Engineering

Copyright © by Michael James Cowan
2022

Structure-property Relationships of Ligand-protected Metal Nanoclusters

Michael James Cowan, PhD

University of Pittsburgh, 2022

Although nanomaterials find use in most technologies, a complete fundamental understanding of their property origins is missing. Solving this problem goes hand-in-hand with achieving structural determination of nanomaterials down to atomic-level precision, which would enable the use of theory to unravel important structure-property relationships (SPRs). Thiolate-protected metal nanoclusters (TPNCs) have attracted tremendous interest as a unique class of atomically precise nanomaterials. Since TPNC structures can be modulated through heterometal doping, the field offers an ideal space to systematically formulate new SPRs. Additionally, TPNCs exhibit physicochemical properties that are favorable for many applications, such as imaging cancer cells and catalysis. Thus, leveraging these “nano-models” for SPR development can directly impact many fields while simultaneously advancing our fundamental understanding of nanomaterials properties.

This work aims to develop, expand, and apply SPRs towards improved TPNC design for targeted applications. First, we demonstrated the application of the Thermodynamic Stability Model across all TPNC sizes. After introducing new ionization potential (IP) and electron affinity (EA) SPRs, we applied these models to a M_{21} - M_{24} series of TPNCs, rationalizing the dopant-based stability observed under experiment. Next, we developed a simple framework that captures TPNC solubility behavior through molecular-like TPNC properties. We then used these properties to rationalize crystallization behavior in a series of TPNCs. Shifting focus to alloy systems, we extended our IP/EA SPRs to capture trends across AgAu TPNCs. Finally, we expanded the application of the Bond-Centric Model to capture stability of TPNCs. Remarkably, the new model rationalized the relative stability between experimentally determined TPNC isomers, revealing its promise as a tool to aid TPNC structure prediction. Overall, this dissertation provides new insights through SPRs that will fuel TPNC discovery towards property-and-application-targeted structure design.

Table of Contents

Preface	xiii
1.0 Introduction	1
1.1 Thiolate-protected Metal Nanoclusters (TPNCs)	1
1.2 TPNC Structural Rules	3
1.3 TPNC Stability Theories	4
1.4 Alloy TPNCs	7
2.0 Rationalizing TPNC Stability Through SPRs	8
2.1 Expanding the Thermodynamic Stability Model (TSM)	8
2.1.1 Computational Details	8
2.1.2 Applying the TSM	10
2.1.3 EA and IP SPRs	11
2.1.4 Towards Targeted TPNC Design	14
2.2 Capturing Stability with IP and EA Trends	14
2.2.1 Computational Details	15
2.2.2 Electronic Stability of the TPNC Series	15
2.2.3 Comparing IP and EA of TPNC Series to Known SPRs	18
2.3 Conclusions	19
3.0 Unraveling Distinct TPNC Properties Through Dipole Moments	20
3.1 Understanding TPNC Solubility Behavior	20
3.1.1 Computational Details	21
3.1.2 Typical <i>vs.</i> Atypical TPNC Solubility	22
3.1.3 Structural Observations	24
3.1.4 Connecting Molecular Properties to Solubility Behavior	26
3.2 Towards TPNC Self-Assembly: Rationalizing Large Dipoles in a M_{23} Series	32
3.2.1 Computational Details	32
3.2.2 Large Dipole Moments	33

3.2.3	Connecting to Crystalline Alignment and Solvatochromism	35
3.3	Conclusions	36
4.0	Decoding Chemical Ordering in Alloy TPNCs	37
4.1	Correlating Structural Rules with IP and EA of Alloy TPNCs	37
4.1.1	Computational Details	38
4.1.2	Generating the Bimetallic TPNC Dataset	38
4.1.3	Exploring IP/EA Trends	39
4.1.4	Extending IP/EA SPRs to capture AgAu TPNCs	41
4.2	Towards a Universal Stability Model for Alloy TPNCs	48
4.2.1	Computational Details	48
4.2.1.1	TPNC Formation Energy (E_f)	48
4.2.1.2	Bond-Centric Model (BCM)	49
4.2.2	Curating a TPNC Dataset	50
4.2.3	Extending the BCM to TPNCs (E_f Model)	51
4.2.4	Applying the E_f Model to $\text{Au}_{38}(\text{PET})_{24}$ Isomers	55
4.3	Conclusions	59
5.0	Future Work	60
5.1	Capture Role of Ligand Effects on TPNC IP and EA	60
5.2	Improved E_f Model that Distinguishes TPNC Core and Shell	61
6.0	Summary of Publications from PhD	62
	Appendix A. Abbreviations and Nomenclature	64
	Appendix B. Rationalizing TPNC Stability Through SPRs	66
	Appendix C. Unraveling Distinct TPNC Properties Through Dipole Moments	67
	Appendix D. Decoding Chemical Ordering in Alloy TPNCs	71
	Bibliography	77

List of Tables

3.1	Experimental solubility behavior of ten TPNCs (including neutral and anionic forms of $\text{Au}_{25}(\text{PET})_{18}$). Ben: benzene, Tol: toluene, DCM: dichloromethane, MeOH: methanol, EtOH: ethanol, ACN: acetonitrile, ACE: acetone, THF: tetrahydrofuran. <i>*Described as “slightly soluble”</i>	24
3.2	Comparing a theoretical $\text{Au}_{29}\text{Ag}_1(\text{SAdm})_{18}$ and its monometallic counterpart.	32
4.1	Summary of TPNCs included in this study grouped by experimental ligand type or hypothetical ligand/doping (denoted with *).	50
C.1	Dipole moment calculations. μ_i corresponds to the i th (x, y, z) component of the dipole vector. magnitude of dipole moment vector (μ) is the magnitude of each vector. All values are in units of Debye.	67
D.1	Exact compositions generated for the bimetallic TPNC dataset from Chapter 4.	71
D.2	Core-shell details of the four Au TPNC used to generate the AgAu TPNC dataset generated in Chapter 4.	72
D.3	List of structural properties explored for EA/IP SPRs for AgAu TPNCs.	73
D.4	Complete list of values used to parameterize the BCM for TPNCs in Section 4.2. CE_{bulk} for Ag and Au are Perdew-Burke-Ernzerhof (PBE)-calculated values taken from literature.	75

List of Figures

1.1	Timeline scheme of the first TPNC structures determined experimentally. Both the anionic ($q = -1$) and neutral ($q = 0$) $\text{Au}_{25}(\text{PET})_{18}$ structures were determined in 2008. Gold and yellow balls represent Au and S atoms, respectively. Red, gray, and light gray sticks represent O, C, and H atoms of the organic ligands, respectively.	3
1.2	Illustration of the divide and protect theory using the $\text{Au}_{25}(\text{PET})_{18}$ structure (left), which can be decomposed into a Au_{13} icosahedron core (top right) protected by a shell of six dimeric staple motifs, RS-Au-SR-Au-SR (bottom right). Gold and yellow balls correspond to Au and S atoms, respectively. R groups are represented as sticks.	5
2.1	Fully optimized TPNC structures ranging from $\text{Au}_{18}(\text{SR})_{14}$ to $\text{Au}_{279}(\text{SR})_{84}$, where the R groups have been simulated with methylthiolate ligands. White, gray, yellow, and gold correspond to H, C, S, and Au atoms, respectively.	9
2.2	Parity of shell-to-core binding energy (BE) and core cohesive energy (CE) of experimentally determined TPNCs. The solid black line indicates perfect parity between cohesive energy (CE) and binding energy (BE). An energy balance is maintained over a large size range of TPNCs further supporting the TSM. The stars denote the largest experimentally synthesized TPNCs, a size regime where the model had not been previously applied.	12
2.3	Electronic property prediction models as a function of number of metal atoms (n) ^{-1/3} , where number of metal atoms (n) is the number of metal atoms. Solid black lines indicate linear fits, whereas shaded regions show 95% confidence intervals. Data points represent vertical IP and EA of TPNCs, in kcal mol ⁻¹ . A red and blue point with the same x-value corresponds to the same structure (only one is labeled). $\text{Au}_{38}(\text{SCH}_3)_{24q}$ and $\text{Au}_{38}(\text{SCH}_3)_{24t}$ were found to have almost exact IPs and EAs with both differences under 0.1 kcal mol ⁻¹	13

2.4	Optimized TPNC structures for IP and EA calculations. R groups (C and H atoms of 1-adamantanethiolate (SAdm) ligands) are removed for clarity.	16
2.5	IP and EA (given in kcal mol ⁻¹ of the Au _n Cd _x (SAdm) _m ($x = 0, 1$) TPNC series (blue circles) and theoretical 7e TPNCs (red squares) plotted against number of metal atoms (n) ^{-1/3} . The results are compared to our previously reported SPRs for neutral TPNCs (gray dashed lines; Figure 2.3)	17
3.1	Comparing Au ₃₀ (SAdm) ₁₈ solubility behavior to Hansen solubility parameters of different solvents and nonsolvents. Different colors indicate experimentally observed solubility behavior. The Hansen solubility parameters, δH , δD , and δP , represent energy contributions from hydrogen bond, dispersion, and polar interactions, respectively. All axes are in intensive (energy per volume) units of MPa ^{1/2}	23
3.2	TPNCs fully optimized with Density Functional Theory (DFT). Gold and red balls correspond to Au and S atoms, respectively. Black and white sticks represent hydrocarbon ligands.	25
3.3	Magnitude of total electronic dipole moment vectors (in Debye, D) for (a) 10 neutral TPNCs (in the order of increasing number of Au) and (b) Au ₂₅ (PET) ₁₈ in the neutral and anionic charge states and in the presence of a tetraoctylammonium (TOA ⁺) counterion (inset structure). The structures exhibiting the minimum (Au ₂₅ (PET) ₁₈ and Au ₃₀ (SAdm) ₁₈) and maximum (Au ₃₈ S ₂ (SAdm) ₂₀) permanent dipoles are shown as insets in the left panel.	28
3.4	Anisotropy in polarizability ($\Delta\alpha$) of TPNCs in the order of increasing number of Au atoms. Anisotropy is given in units of Å ³	29
3.5	Comparing permanent dipole moment and anisotropy to TPNC solubility behavior. Data point colors indicate observed solvents for each TPNC (based on Table 3.1). Boxes represent regions of typical (green) and atypical (red) solubility behavior.	31
3.6	Optimized structures and calculated dipole moments (magnitude of dipole moment vector (μ)) of Au ₁₉ Ag ₄ (SR) ₁₅ , Au ₂₂ Cd ₁ (SR) ₁₅ Br, and Au ₁₉ Ag ₃ Cd ₁ (SR) ₁₅ Br (SR = SCH ₃).	33

3.7	Optimized structures with calculated magnitude of dipole moment vector (μ) and natural bond orbital (NBO) charge analysis for (a) $\text{Au}_{19}\text{Ag}_3\text{Cd}_1(\text{SR})_{15}\text{Br}$, (b) $\text{Au}_{22}\text{Cd}_1(\text{SR})_{15}\text{Br}$, and (c) $\text{Au}_{19}\text{Ag}_4(\text{SR})_{15}$. Ligands are omitted for clarity. natural bond orbital (NBO) charges are labeled (left) and marked by color (right, blue = positive and red = negative). Selected dipoles along the C_3 axis are indicated by green arrows which contribute to magnitude of dipole moment vector (μ) (magenta arrows); Local dipoles that are expected to cancel out are indicated by purple arrows.	34
4.1	Examples of the different TPNC sizes used in this study. The selected samples have 50% Ag composition and a randomly generated chemical ordering. Color scheme: Au: yellow, Ag: grey, S: red, C: black, H: white.	39
4.2	Demonstration of face-centered cubic (FCC) cores (top row) and shell motifs (bottom row; core atoms shown in light gray for contrast) of the four Au TPNCs used to generate the hypothetical AgAu TPNC dataset in Chapter 4 (see Section 4.1.2 for more details on the dataset). Color scheme: Au: yellow, S: red. R groups omitted for clarity.	40
4.3	Comparing EA and IP of hypothetical AgAu TPNCs. Data color corresponds to composition of Ag (X_{Ag}). Clusters of data labeled by TPNC size. Monometallic data points are highlighted with a black border. M denotes Ag and Au.	42
4.4	Comparing number of metal atoms to the power of $-1/3$ ($n^{-1/3}$) to a) EA and b) IP for our sample of hypothetical AgAu TPNCs. Data color corresponds to composition of Ag (X_{Ag}). Monometallic data points are highlighted with a black border. We note that the monometallic Au_{36} IP point is directly underneath the Ag_{36} point. Clusters of data labeled by TPNC size. Dotted lines represent previously reported EA/IP structure-property relationships for Au TPNCs (see Section 2.1.3).	44
4.5	Linear regression models (top of plots) that capture a) EA and b) IP of AgAu TPNCs based on simple structural descriptors. Clusters of data labeled by TPNC size. Mean absolute error (MAE) of models are inlaid.	45

4.6	Density Functional Theory (DFT)-calculated TPNC formation energy (E_f^{DFT}) <i>vs.</i> number of metal atoms (m). Data color separates by AgAu TPNCs (blue), PET-protected Au TPNCs: orange, SCH ₃ -protected Au TPNCs: green, TBBT-protected Au TPNCs: red.	52
4.7	Parity plot comparing extended BCM model performance to Density Functional Theory (DFT) based on TPNC formation energy (E_f).	54
4.8	TPNC formation energy (E_f in eV/ m , where m is the number of ligands) of two experimentally determined Au ₃₈ (PET) ₂₄ isomers: Q (left) and T (right). Blue bars = E_f^{DFT} , Green bars = E_f^{model}	57
4.9	TPNC structures (top row) of two experimentally determined Au ₃₈ (PET) ₂₄ isomers: Q (left) and T (right). MS motifs (middle row) and cores (bottom row) of each TPNC are shown to illustrate the structural differences between isomers. .	58
B.1	Metal-ligand relationship of experimentally determined TPNCs (labeled Au _{<i>n</i>} (SR) _{<i>m</i>}). Number of ligands (m) linearly correlates with $n^2/3$ (depicted by the solid black line) with an R ² of 0.995. The shaded orange region represents the 95% confidence interval of the linear regression fit.	66
C.1	Charge density maps of Au ₃₀ (SAdm) ₁₈ . a) Electrostatic potential map and b) atomic point charges calculated with Bader charge analysis. Blue and red colors correspond to positive and negative charge, respectively.	68
C.2	Average polarizability compared to number of electrons in each TPNC. Different colors correspond to different ligand type. A linear regression was calculated for all data (solid black line) as well as TPNCs protected by TBBT (dotted green line) and SAdm (dotted blue line).	69
C.3	TPNC dipole alignment in the crystal states of (a) Au _{22-<i>n</i>} Ag _{<i>n</i>} Cd ₁ (SAdm) ₁₅ Br ($n = 1-4$), (b) Au ₂₂ Cd ₁ (SAdm) ₁₅ Br, and (c) Au ₁₉ Ag ₄ (SAdm) ₁₅ . All TPNCs are marked with their dipole vectors, and the energy of attraction interactions between two NC dipoles are indicated in the unit of kJ/mol. Color labels: yellow = Au, light gray = Ag, pink = Au/Ag, blue = Cd, maroon = Br, green = Cl, light yellow = S, and gray = C.	70

D.1	Bond analysis of the optimized AgAu TPNC dataset from Chapter 4. Violin plots show the distribution of bond distances between different element pairs, including the range (capped lines) and relative frequency of bond lengths (shaded regions).	73
D.2	Comparing X_{Ag} (a, b) to core-shell descriptors (c, d) for capturing EA and IP trends in $M_{36}(SR)_{24}$.	74
D.3	TPNC formation energy (E_f) of $Au_{38}(SR)_{24}$ isomers, Q (left) and T (right), protected by SCH_3 as a theoretical substitution to phenylethanethiolate (PET). Blue bars = E_f^{DFT} , Green bars = E_f^{model} .	76

Preface

First and foremost, I am forever grateful for the opportunity to work with my advisor, Dr. Giannis Mpourmpakis, during my PhD tenure. Yanni, thank you for making me a better researcher, communicator, and overall person. Through your endless support and your many invaluable lessons, I know you have truly set me up for a successful future. Dr. Jin, thank you for your endless supply of fascinating questions and fascinating structures! I consider our collaborations a true privilege and I am beyond fortunate to have worked with you and your former students, Dr. Yingwei Li and Dr. Tatsuya Higaki, on many interesting problems. Dr. Millstone and Dr. Wilmer, thank you both for your kindness and the many fruitful discussions over the years, especially during my proposal examination. Your questions have always challenged me to think differently, and I know my work improved because of it.

To the Mpourmpakis Group (CANELa), from past and present, thank you for the countless discussions, debates, and laughs. I have formed many friendships that I know I will keep for the rest of my life. To my first mentor, Dr. Michael Taylor, thank you for your advice and guidance during my early years as a PhD student. To Dr. James Dean, Anantha Nagarajan, Dr. Rosalba Juarez-Mosqueda, Dr. Cristian Morales, and Denny Loevlie, thank you for the great collaborations. A special thanks to Maya Salem, Julia McKay, Ethan Holbrook, Brenno Ferreira, and Sean Cotton for showing me kindness and respect as a mentor. Thank you to the *many* other members of CANELa who I have had the privilege of working with and learning from. Also, I humbly acknowledge my funding resources. My work would not have been possible without support from the National Science Foundation under grant no. 1652694 and computational resources from Pitt's CRC and NSF XSEDE.

Finally, a huge thank you to my family. To my sister Kristen and her husband, Chris, and to my sister Amy, thank you for being supportive siblings throughout my life and especially during my graduate career. To my parents, Kim and Mark, I owe you the greatest thank you of all. Mom and Dad, you have always been my biggest fans and my biggest role models. Thank you for always pushing me to be the best form of myself. I would not be here today without your unconditional love and support.

1.0 Introduction

The content of this chapter is adopted, in part, from:

- M. J. Cowan and G. Mpourmpakis. Towards elucidating structure of ligand-protected nanoclusters. *Dalton Transactions*, 49:9191–9202, 2020.

As society advances, nanomaterials weave tighter into our everyday lives – demanding continued improvement to their properties for a breadth of applications. At the nanoscale, structure, or atomic arrangement, dramatically dictates materials properties. Thus, a long sought goal of nanomaterials research has been achieving complete atomic-level control over structure.[1] Through atomically precise synthesis and structure determination, one can leverage first principles calculations and systematic analysis across a series of structures to reveal nanomaterial structure-property relationships (SPRs).[2] Development of SPRs provides new insights into the origins of nanomaterials properties as well as enables application targeted design.

1.1 Thiolate-protected Metal Nanoclusters (TPNCs)

Thiolate-protected metal nanoclusters (TPNCs) have recently attracted great interest as a unique class of atomically precise nanomaterials.[3] Due to their high stability and distinct properties (spanning from molecular- to metallic-like characteristics), TPNCs are often regarded as inorganic-organic hybrid molecules, thus differentiating them from larger metal nanoparticles.[4] With a growing catalogue of structures achieved through ligand and metal variation,[5] TPNCs make up the ideal “playground” to formulate new SPRs. Furthermore, TPNCs exhibit intriguing properties ranging from structural, to optical, to electrochemical,[6–10] giving rise to vast potential for many applications over a broad range of fields. For instance, the luminescent properties of TPNCs have opened avenues for their use in detecting

biomolecules,[11] as well as imaging cancer cells[12,13] and bacteria.[14] Additionally, TPNCs have emerged as efficient and selective catalysts owing to their high surface-to-volume ratio and discrete electronic states (*i.e.*, molecular-like HOMO-LUMO gap rather than metallic character).[15] TPNCs can catalyze a variety of reactions, including among others the hydrogenation of nitrobenzaldehyde,[16] photocatalytic degradation of organic pollutants,[17] and the electrocatalytic reduction of CO₂. [18] With the ever-growing possibilities for practical nanotechnological applications, research interest for TPNCs continues to expand.

One of the most popular synthesis methods of TPNCs, and arguably the work that ignited the field, was introduced by Brust *et. al.* in 1994, where Au salts were reduced in the presence of organic thiols and a strong reducing agent (NaBH₄). [19] The synthesis of thiolate-protected Au nanoparticles was achieved, exhibiting a distribution of diameters ranging 1-3 nm, but structural characterization with atomic precision was still lacking. Over the next decade, improvements were made to the synthesis process such that TPNCs with exact molecular weights were discovered using separation methods and mass spectrometry.[20–22] True atomic precision, however, was not reached until 2007, where Jadzinsky and Calero *et. al.* were able to characterize the exact atomic positions of Au₁₀₂(p-MBA)₄₄ (p-MBA = *para*-mercaptobenzoic acid) within an unprecedented 1.1 Å resolution through single crystal X-ray diffraction.[23] With this pioneering work, the discovery of additional TPNC structures followed soon after, including both the anionic[24] and neutral[25] Au₂₅(PET)₁₈ (PET = phenylethanethiolate) in 2008, the Au₃₈(PET)₂₄ in 2010,[26] and the Au₃₆(TBBT)₂₄ (TBBT = 4-*tert*-butylbenzenethiolate) in 2012[27] (Figure 1.1).

TPNCs are also referred to as “magic size” nanoclusters, since they exhibit high stability at specific compositions (*i.e.*, at specific n and m of $M_n(SR)_m$ structures).[4] This emergence of magic sizes was primarily due to the development of a size focusing synthesis method.[28] According to the size focusing method, after the initial formation of polydisperse TPNCs, the solution is exposed to “harsh” conditions, such as excess thiol concentration and elevated temperatures. This process leads to only the most stable TPNC surviving in a monodisperse environment, thus “focusing” the TPNC distribution to a single TPNC structure. Additional methods to synthesize new magic sizes have also been developed, including ligand-based approaches to control TPNC size[29] and TPNC-TPNC transformations through ligand ex-

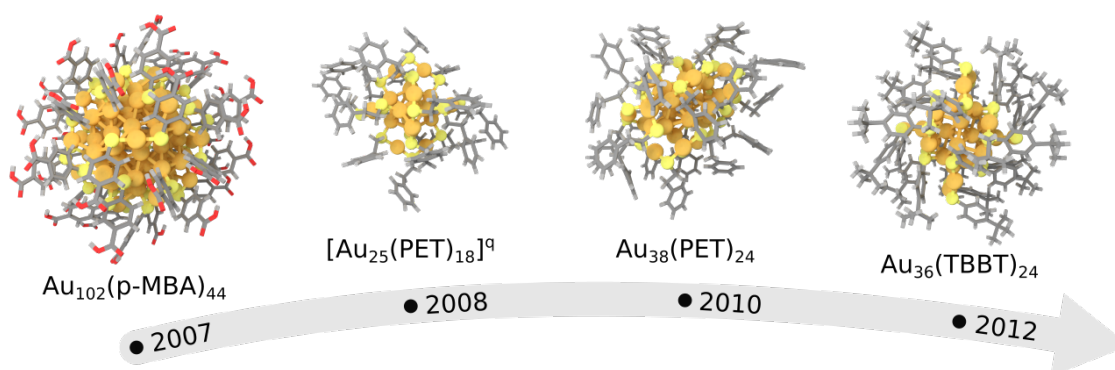


Figure 1.1: Timeline scheme of the first TPNC structures determined experimentally. Both the anionic ($q = -1$) and neutral ($q = 0$) $\text{Au}_{25}(\text{PET})_{18}$ structures were determined in 2008. Gold and yellow balls represent Au and S atoms, respectively. Red, gray, and light gray sticks represent O, C, and H atoms of the organic ligands, respectively.

change.[30] With the continuous advancement of synthesis and post-synthetic manipulation methods, there is practically no end in sight to the experimental discovery of new, atomically precise TPNCs.

1.2 TPNC Structural Rules

The experimental advances in TPNC synthesis and characterization have provided nanostructures with atomic-level precision to theory. In addition, developments in theory and increase in computational power have enabled the investigation of large systems, such as TPNCs, with accurate, first principles methods.[31,32] As a result, the combination of both ends has led to the detailed elucidation of TPNC properties. Although many structural rules and SPRs have been developed due to the expanding number of experimentally synthesized TPNCs, the first structural rule came as a prediction that was later confirmed through the determination of the $\text{Au}_{102}(\text{p-MBA})_{44}$. The “divide and protect” theory,[33] first introduced

by Häkkinen *et. al.* in 2006, states that the TPNC structure consists of two distinct regions: i) a highly symmetric core made solely of metal atoms, which is protected by ii) a shell of ligand-metal motifs (Figure 1.2). The protecting groups form as RS-(M-SR)_x units.[33] These units range in sizes, known as different x -Mers,[3] and include $x = 0$ (i.e. a bridging thiolate[34] or a μ_3 -coordinated sulfide group[35–37]). Additionally, protecting ring motifs have been observed (*e.g.*, octameric ring in the $\text{Au}_{20}(\text{TBBT})_{16}$ [38]) where metal-ligand units form a complete loop around the TPNC core. These RS-(M-SR)_x protecting groups became known as “staple” motifs due to the staple-like appearance of dimers (RS-(M-SR)_2) around the core of the first determined TPNC, the $\text{Au}_{102}(\text{p-MBA})_{44}$. [23,39] Remarkably, this simple yet powerful theory universally captures the structural makeup of all TPNCs.

A second structure-based rule captures the composition constraints of magic size TPNCs. The “nano-scaling law” [40] describes the number of metal atoms (n) and number of ligands (m) as analogues to the volume (V) and surface area (SA) of TPNCs, respectively. Through analysis of the known magic sizes, the TPNCs were found to follow the relationship $SA \propto aV^{2/3}$ (a = scaling factor), which is a known scaling law of primitive geometric shapes. In other words, stable $\text{M}_n(\text{SR})_m$ nanoclusters follow $n \propto m^{2/3}$, which rationalizes the specific n and m pairs that emerge in the magic sizes. Subsequent work found that the type of ligand affects the scaling factor.[41,42] The nano-scaling law reveals the power of population-based analyses, highlighting their effectiveness for developing SPRs.

1.3 TPNC Stability Theories

Since the early syntheses of TPNCs, a major topic of research focus has been determining what gives rise to their stable magic sizes. To rephrase, why can the $[\text{Au}_{25}(\text{SR})_{18}]^-$ be synthesized with high stability,[24, 25] but a $[\text{Au}_{26}(\text{SR})_{18}]^-$ cannot? Although structural rules can capture geometric trends in TPNCs, they do not provide a means of rationalizing the stability of these nanoscale systems. As a result, all stable TPNCs generally follow the divide and protect theory and nano-scaling law, but a theoretically predicted TPNC that adheres to these rules may not be stable. Thus, there has been extensive work on ratio-

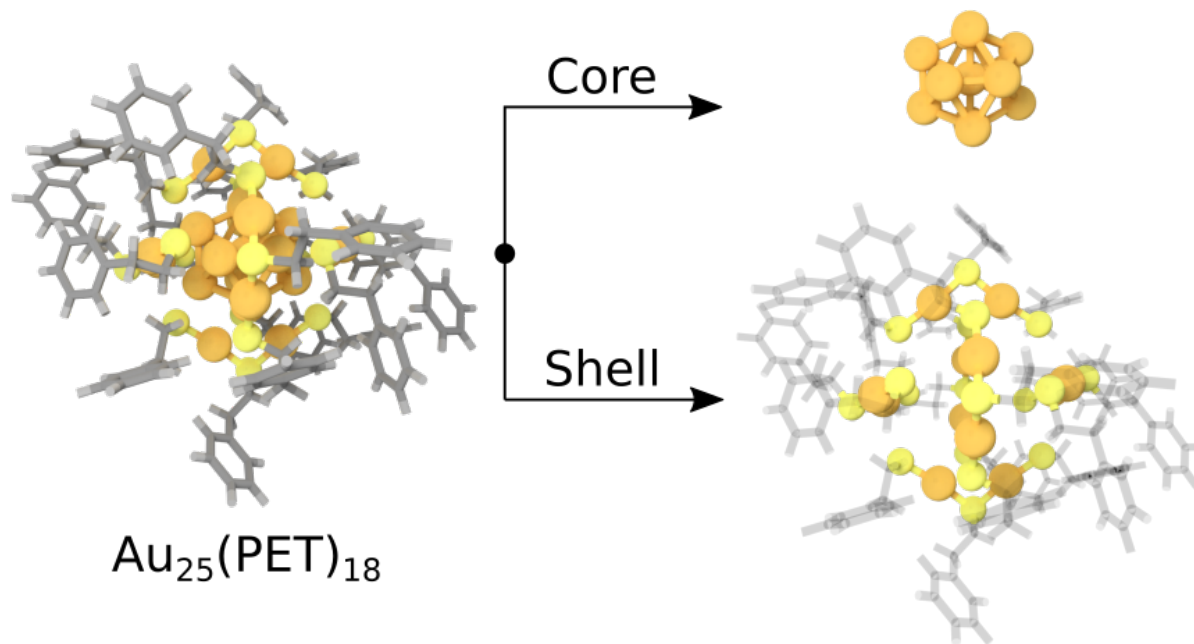


Figure 1.2: Illustration of the divide and protect theory using the $\text{Au}_{25}(\text{PET})_{18}$ structure (left), which can be decomposed into a Au_{13} icosahedron core (top right) protected by a shell of six dimeric staple motifs, RS-Au-SR-Au-SR (bottom right). Gold and yellow balls correspond to Au and S atoms, respectively. R groups are represented as sticks.

nalizing the stability of magic size TPNCs through both their geometric (atomic positions) and electronic (electron configuration) structures. The earliest method utilized an electron counting approach. Drawing from the jellium model, the superatom theory describes that stable TPNCs have a closed electronic valence shell and a relatively large HOMO-LUMO gap.[43] Due to metal-ligand bonding, the valence electron count (e) for $[M_n(SR)_m]^q$ can be calculated following $e = n\nu - m - q$, where ν is the atomic valence of the metals.[43] For example, the $[Au_{25}(SR)_{18}]^-$ has 8 valence electrons since $25(1) - 18 - (-1) = 8$. When first revealed, this theory captured the stability of most magic TPNCs. However, the continuous synthesis of new structures led to many cases that the superatom theory could not capture, thus limiting its application as a universal stability model.[44] Therefore, although instrumental in introducing fundamental concepts to the field, the superatom theory lacks universal predictive power of TPNC stability across their complete materials space.

Recently, Taylor and Mpourmpakis developed the Thermodynamic Stability Model (TSM). The TSM is the first model that not only captures the complete geometric and electronic TPNC structure (*i.e.*, exact atomic positions and electron configuration, respectively), but also incorporates fundamental thermodynamics to rationalize TPNC stability.[45] The model leverages the divide and protect theory[33] of a core-shell structure and builds on chemical potential contributions between the core and the shell region of the TPNCs. Given the harsh conditions undergone during size focusing synthesis,[28] a stable TPNC achieves chemical equilibrium between its core metal kernel and shell of staple motifs. This equilibrium of chemical potentials can be approximated by two electronic properties, *i.e.*, the core cohesive energy (CE) and shell-to-core binding energy (BE), which can both be calculated using Density Functional Theory (DFT). Core CE is the average bond strength between core metal atoms in the presence of the protecting shell motifs, whereas shell-to-core BE is the binding strength of the shell motifs to the core. When applied to a range of TPNCs, the TSM reveals a fine energy balance between the core CE and the shell-to-core BE for experimentally synthesized (stable) TPNCs. Importantly, the TSM is not constrained to electron counting rules, thus holding predictive power to test on any theoretical candidate structures.

1.4 Alloy TPNCs

In recent years, significant research has been done to introduce heterometals into TPNCs, forming a new class of alloy TPNC derivatives with distinct properties.[5] Alloy TPNCs can be synthesized by heterometal doping to form analogues of their monometallic counterparts,[46] or even entirely new structures.[47] Importantly, alloy TPNCs provide additional parameters, metal type and composition, that can be tuned for properties control.[5]. However, due to distributions in dopant concentrations,[47] atomic precision can be lost. To improve our understanding of favorable dopant concentration and location, one can apply computational methods like DFT to screen alloy TPNC candidates and compare their stability. Although effective for a sample of TPNCs, a major challenge becomes overcoming the curse of combinatorics – a problem also faced in the field of “unprotected” polymetallic nanoparticles.[48] The vast materials space that TPNCs exhibit is due to the many choices of metals and ligands. Imagine transforming from $\text{Au}_{25}(\text{SR})_{18}$ to $\text{Ag}_{25}(\text{SR})_{18}$ by doping one Ag atom at a time, giving only 26 unique compositions (including the two monometallic cases). Within this constrained example, there are actually 33,554,432 unique structures ($\sum_{i=0}^{25} 25\text{-choose-}i$, excluding symmetry) due to the distinct positions that each metal type can take (*i.e.*, different possible chemical orderings). The problem becomes even more challenging if we expand to a trimetallic $\text{M}_{25}(\text{SR})_{18}$ system, which has been reported in literature.[49] Moreover, removing the structure and single ligand constraints further opens the search space of candidate TPNCs. This ever-expanding materials space requires new computational frameworks that enable high throughput screening of TPNC candidates at reduced computational cost. Developing such tools would enhance our understanding of TPNC doping preference and provide actionable insight to experimentalists for alloy nanocluster design.

2.0 Rationalizing TPNC Stability Through SPRs

The content of this chapter is adopted, in part, from:

- M. J. Cowan and G. Mpourmpakis. Structure-property relationships on thiolate-protected gold nanoclusters. *Nanoscale Advances*, 1:184–188, 2019.
- Y. Li*, M. J. Cowan*, M. Zhou, Y. Song, T. Y. Luo, H. Wang, N. L. Rosi, G. Mpourmpakis, and R. Jin. Atom-by-atom evolution in the adamantanethiolate-protected Au₂₁ - Au₂₂ - Au₂₂Cd₁ - Au₂₄ nanocluster series. *Journal of the American Chemical Society*, 142(48):20426—20433, 2020.

2.1 Expanding the Thermodynamic Stability Model (TSM)

As previously mentioned in Section 1.3, in 2017, Taylor and Mpourmpakis introduced the TSM,[45] which connects core-shell structural characteristics with the thermodynamics of formation of TPNCs. Their work showed that the TSM accurately predicts stability for numerous experimentally synthesized TPNCs ranging in size, structure, and metal composition, laying the foundation for the theory’s applicability as a general stability model.[45,50] However, the original development of this model only tested structures $n \leq 102$. [45] In this study, we sought to expand the proven capabilities of the TSM by testing it across the complete range of experimentally determined TPNC structures (up to $n = 279$). [51]

2.1.1 Computational Details

We employed DFT calculations to examine fifteen experimentally determined TPNC structures.[23, 26, 35, 36, 38, 52–59] All calculations were performed with no symmetry constraints using the Perdew-Burke-Ernzerhof (PBE) exchange–correlation functional [60] with a double- ζ valence polarized (DZVP) basis set and Goedecker-Tetter-Hutter (GTH) pseu-

*Authors contributed equally.

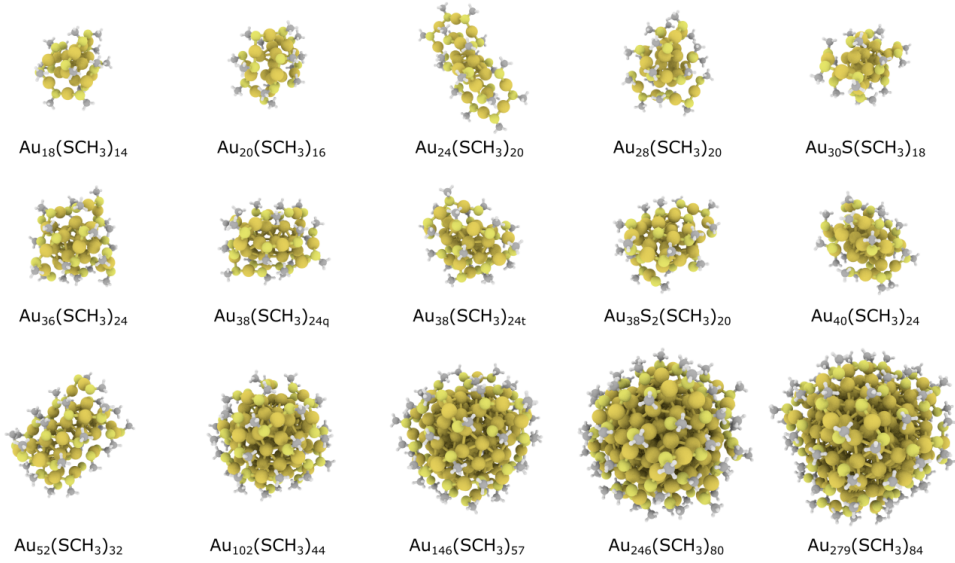


Figure 2.1: Fully optimized TPNC structures ranging from $\text{Au}_{18}(\text{SR})_{14}$ to $\text{Au}_{279}(\text{SR})_{84}$, where the R groups have been simulated with methylthiolate ligands. White, gray, yellow, and gold correspond to H, C, S, and Au atoms, respectively.

dopotentials,[61] as implemented in CP₂K.[62] All TPNCs were centered in a non-periodic cubic box with a 7 Å minimum offset between the structure and boundary. Similar to previous electronic structure studies,[39, 45] full ligands were replaced with methylthiolates to reduce computational cost. The TSM was applied based on previously reported methods.[45] In addition, the vertical ionization potential (IP) and electron affinity (EA) were calculated according to the following expressions:

$$IP = E_{TPNC}^{q+1} - E_{TPNC}^q \quad (2.1)$$

$$EA = E_{TPNC}^{q-1} - E_{TPNC}^q \quad (2.2)$$

where E_{TPNC}^x is the electronic energy of a TPNC with its original charge $x = q$ or in a perturbed charge state $x = q \pm 1$.

Figure 2.1 shows our fifteen fully optimized experimentally determined TPNCs, which includes various shapes and sizes (number of metal atoms, n , ranging from 18 to 279). We

note that methylthiolates (SCH_3) were used in place of full ligands. Prior studies have shown that full-to-methyl ligand change may affect nanocluster properties when there is significant reconstruction of the TPNC during relaxation (*i.e.*, deviation from crystal structure).[45] Thus, it is important to note that there was no reconstruction during optimization for any of the TPNCs presented in Figure 2.1. Additionally, recent work has demonstrated that the TSM also captures stability when using full ligands,[50] illustrating its effectiveness across different ligand types.

2.1.2 Applying the TSM

As previously stated, the divide and protect structural rule states that all TPNCs are made up of a highly symmetric metallic core protected by a shell of metal-ligand “staple” motifs.[33] Inspired by this rule, the TSM connects core-shell structural characteristics with the thermodynamics of colloidal TPNC formation. This is done by comparing the core cohesive energy (CE) and shell-to-core binding energy (BE) of a TPNC to determine stability. A balance between these energies (*i.e.*, parity) represents a thermodynamic chemical equilibrium achieved between the core and shell. In other words, a thermodynamically stable TPNC will exhibit a fine energy balance between core CE and shell-to-core BE.[45]

Based on the methodology previously reported,[33,45] each structure from Figure 2.1 was split into its respective core and shell regions and the core CE and shell-to-core BE were calculated. Figure 2.2 depicts the energy balance between core CE and shell-to-core BE for the TPNCs studied. Notably, the $\text{Au}_{38}\text{S}_2(\text{SCH}_3)_{20}$, $\text{Au}_{40}(\text{SCH}_3)_{24}$, $\text{Au}_{52}(\text{SCH}_3)_{32}$, $\text{Au}_{146}(\text{SCH}_3)_{57}$, $\text{Au}_{246}(\text{SCH}_3)_{80}$, and $\text{Au}_{279}(\text{SCH}_3)_{84}$ have never been analyzed with this theory. Interestingly, the three largest structures (denoted with stars in Figure 2.2), the $\text{Au}_{146}(\text{SCH}_3)_{79}$, $\text{Au}_{246}(\text{SCH}_3)_{80}$, and $\text{Au}_{279}(\text{SCH}_3)_{84}$, are in excellent agreement with the theory, falling very close to the parity line. The results of these larger TPNCs support the model’s capability as a tool for capturing stability of TPNCs approaching a few hundred metal atoms. It should again be noted that the TSM had been applied up to the $\text{Au}_{102}(\text{SCH}_3)_{44}$ TPNC and this is the first time we demonstrate that the theory is extendable to significantly larger systems, like the $\text{Au}_{279}(\text{SCH}_3)_{84}$. Along with these large TPNCs, $\text{Au}_{38}\text{S}_2(\text{SR})_{20}$, $\text{Au}_{40}(\text{SR})_{24}$

and $\text{Au}_{52}(\text{SR})_{32}$ were analyzed with this theory for the first time to further explore different core packing structures and size regions of TPNCs. The three structures were found to display a fine CE-to-BE energy balance. Though the remaining structures had been previously computationally investigated using the TSM,[45] our work herein has been performed using a different exchange-correlation functional, namely PBE.[60] As a result, utilizing different computational methods provides further evidence towards the legitimacy of the TSM, which is agnostic to functional choice, and is solely based on thermodynamics foundations.

2.1.3 EA and IP SPRs

Understanding electronic properties of TPNCs is essential for their use in catalysis and chemical sensing.[63,64] Moreover, unraveling simple relationships based on experimentally measurable properties could allow for the development of practical models that researchers can employ to screen the electronic properties of TPNCs as a function of their size. In consideration of this, the IP and EA for the fifteen TPNCs were calculated. As shown in Figure 2.3, it was found that there is a size effect for both IP and EA that is dominated by the number of metal atoms (n) within a nanocluster. As the TPNC size increases (*i.e.*, n increases), the IP decreases (becomes less endothermic). The EA follows the same trend, only that since the values are negative, as the TPNC size increases the EA becomes more exothermic. In other words, the larger TPNCs, like $\text{Au}_{279}(\text{SCH}_3)_{84}$, require the least amount of energy to remove an electron and exhibit the highest affinity to receive an electron. Previous work has indicated that certain ligands, especially ones with electron withdrawing character, can impact the EA and IP of TPNCs.[65,66] For this reason, we note that deviations from the models could potentially exist for TPNCs stabilized with electron withdrawing ligands (*e.g.*, *para*-mercaptobenzoic acid (p-MBA)), but the general trends (*i.e.*, size-effect) provided from the models will still remain valid. The results presented in Figure 2.3 trend with the general size dependence of HOMO-LUMO gaps previously reported for TPNCs.[67] Additionally, we note that the IP and EA models are indiscriminate of core packing structure, as the cores of the TPNCs studied herein include FCC-, HCP- and BCC-like packing.

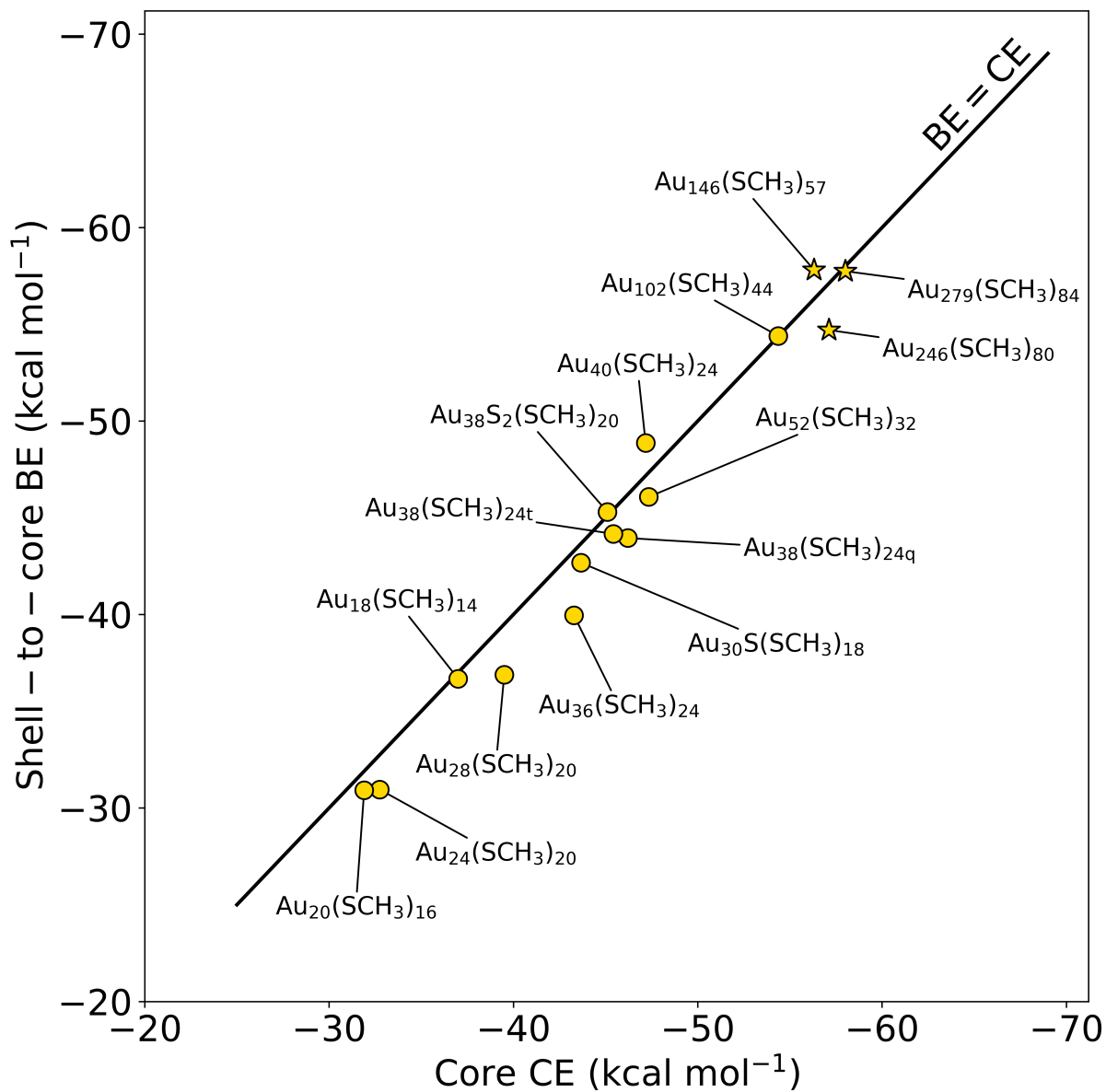


Figure 2.2: Parity of shell-to-core BE and core CE of experimentally determined TPNCs. The solid black line indicates perfect parity between CE and BE. An energy balance is maintained over a large size range of TPNCs further supporting the TSM. The stars denote the largest experimentally synthesized TPNCs, a size regime where the model had not been previously applied.

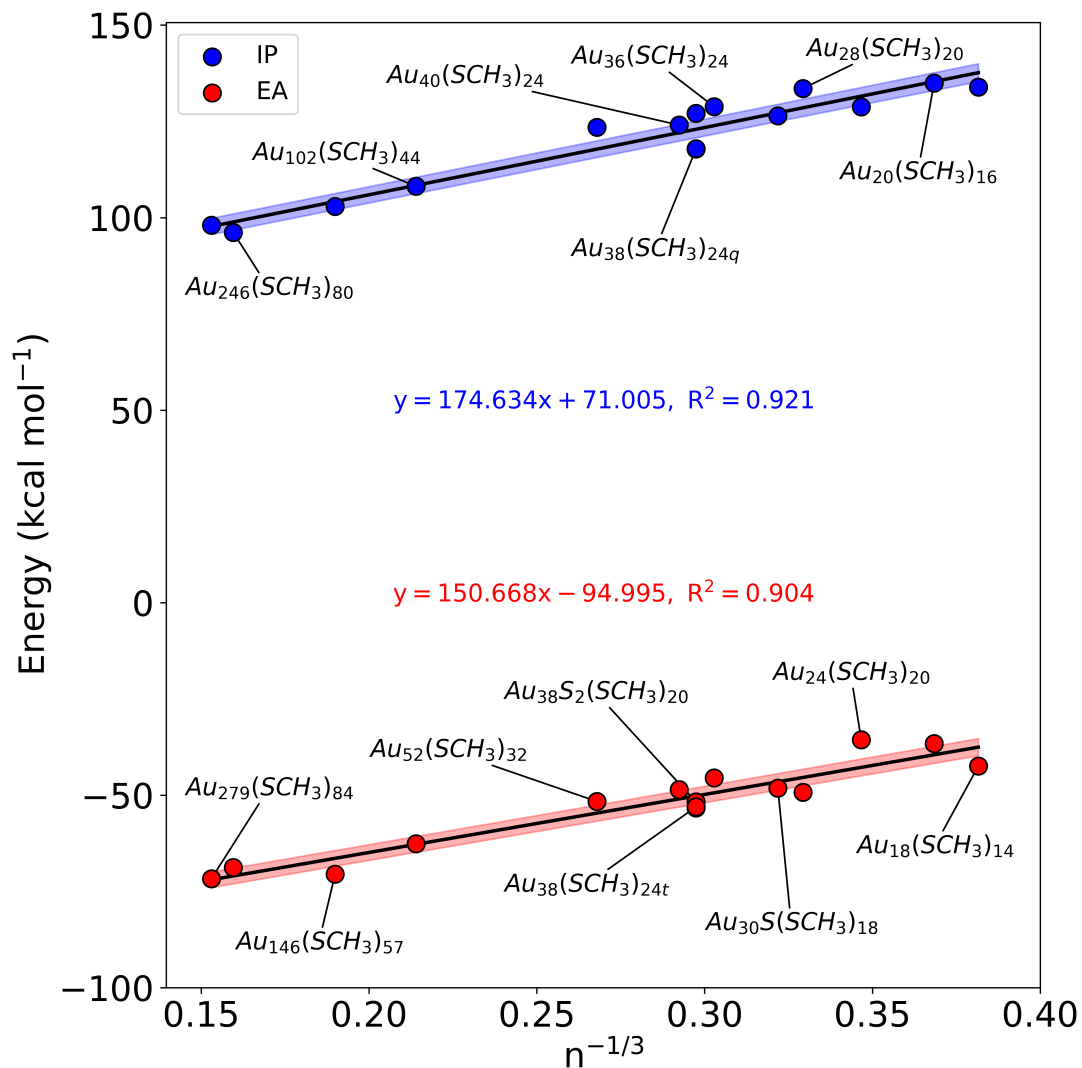


Figure 2.3: Electronic property prediction models as a function of $n^{-1/3}$, where n is the number of metal atoms. Solid black lines indicate linear fits, whereas shaded regions show 95% confidence intervals. Data points represent vertical IP and EA of TPNCs, in kcal mol^{-1} . A red and blue point with the same x-value corresponds to the same structure (only one is labeled). $\text{Au}_{38}(\text{SCH}_3)_{24q}$ and $\text{Au}_{38}(\text{SCH}_3)_{24t}$ were found to have almost exact IPs and EAs with both differences under $0.1 \text{ kcal mol}^{-1}$.

2.1.4 Towards Targeted TPNC Design

First introduced by Dass *et. al.*, [40] Figure B.1 shows the results of a nano-scaling law applied to the TPNCs studied in this work. Similar to Figure 2.3, the number of Au atoms is an important factor, in this case to describe the number of ligands present on each TPNC. Notably, even the largest $\text{Au}_{146}(\text{SR})_{57}$, $\text{Au}_{246}(\text{SR})_{80}$, and $\text{Au}_{279}(\text{SR})_{84}$ TPNCs are found to follow the model, providing strong evidence that virtually all magic-sized TPNCs scale with this simple structural relationship. Although the metal-ligand composition model cannot entirely predict new TPNCs, it still plays a significant role in the structure prediction process, identifying the number of ligands needed to stabilize a specific number of Au atoms. In fact, along with the IP and EA SPRs developed in this work, as well as the TSM, [45] one can start building a framework enabling a property-specific design of new TPNCs. Starting with a targeted application that requires a TPNC with a specific IP, the IP model portrayed in Figure 2.3 can be used in concert with the nano-scaling law (Figure B.1) to determine the appropriate TPNC composition needed. Previous work has revealed that the type of thiolate ligand (*i.e.*, the “R” group in $\text{Au}_n(\text{SR})_m$) plays a central role in metal-ligand composition of the stable nanocluster synthesized. [29, 68] Therefore, an experimentalist could utilize these ligand effects to control the number of metal atoms desired within the TPNC and thus, the resulting electronic properties. Additionally, the TSM can aid in screening the stability of potential TPNC candidates in a size-focused effort due to the composition constraint from the nano-scaling law. Overall, this approach, which utilizes computationally discovered structure-property (electronic and stability) relationships, could guide experimentation towards a property-targeted synthesis of TPNCs.

2.2 Capturing Stability with IP and EA Trends

Realizing TPNC electronic property trends not only award an accelerated means of property prediction, but also offer avenues towards systematic comparisons of synthetically accessible *vs.* inaccessible structures. That is, we can probe the stability of theoretical TP-

NCs by testing them against validated SPRs that were determined from a global analysis of stable structures. Our next work applied this methodology, using our IP and EA SPRs, to an incremental M_{21-24} nanocluster series all protected by 1-adamantanethiolate (SAdm).[69] Of note, this TPNC series is the first reported that exhibits an atom-by-atom growth evolution, following $Au_{21}(SAdm)_{15}$, $Au_{22}(SAdm)_{16}$, $Au_{22}Cd_1(SAdm)_{16}$, and $Au_{24}(SAdm)_{16}$. Our focus was to rationalize why these structures were synthesizable relative to other potential monometallic or heterometal-doped states.

2.2.1 Computational Details

DFT calculations were performed without any symmetry constraints using the PBE functional with def2-SV(P) basis sets[70] accelerated with the Resolution of Identities (RI) approximation,[71] as implemented in Turbomole v7.2.[72] Geometry optimizations were performed on each SAdm-protected TPNC in the series starting from their experimentally determined structures reported in our work[69] and in literature.[34, 53, 69] The structures were optimized using a quasi-Newton Raphson method and converged to successive energies under 10^{-6} Ha as well as interatomic forces under 10^{-3} Ha/Bohr. Theoretical 7e TPNCs were produced by replacing a single kernel Au with Cd within the optimized $Au_{21}(SAdm)_{15}$ and $Au_{22}(SAdm)_{16}$, or replacing the Cd with Au within the optimized $Au_{22}Cd_1(SAdm)_{16}$. Geometry optimizations were then performed on the new theoretical TPNCs under the aforementioned specifications. Finally, vertical IP and EA were calculated for each experimental and theoretical TPNC using Equations 2.1 and 2.2, respectively (where $q = 0$ for all cases).

2.2.2 Electronic Stability of the TPNC Series

An interesting issue to address for the $M_{21}-M_{24}$ series is related to the stability of the TPNCs based on free electron counting rules from the superatom theory[43] (discussed in Section 1.3). Despite the smooth, atom-by-atom transition exhibited by the TPNC series, there is a sharp transition in their free electron counts. As Figure 2.4 shows (blue dashed box), the series shifts from 6e for $Au_{21}(SAdm)_{15}$ and $Au_{22}(SAdm)_{16}$ (*i.e.*, $21-15 = 22-16 = 6e$) to 8e for $Au_{22}Cd_1(SAdm)_{16}$ and $Au_{24}(SAdm)_{16}$ ($22+2-16 = 24-16 = 8e$), skip-

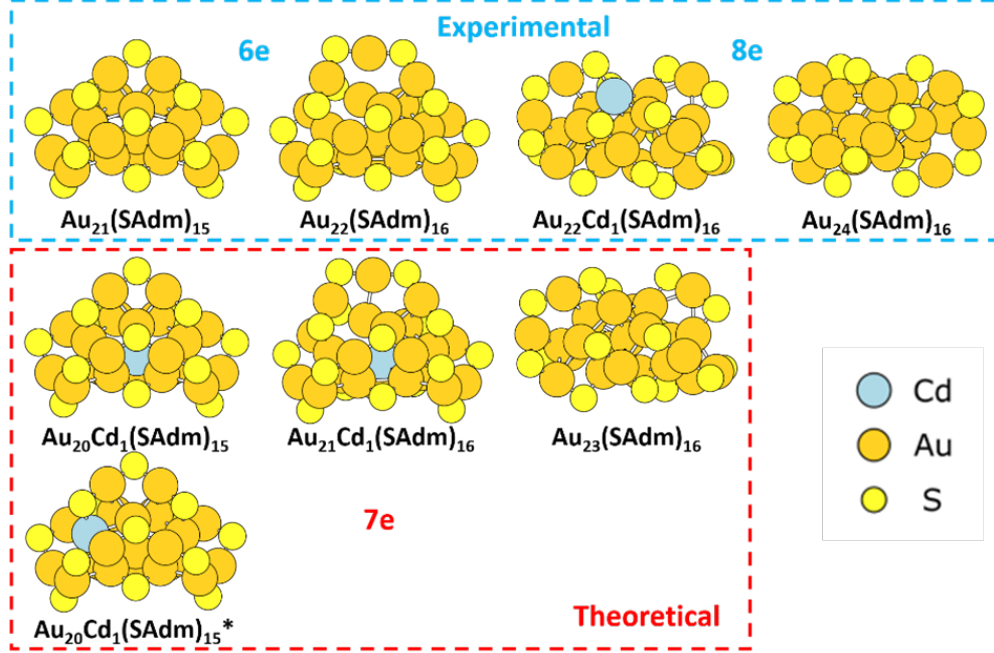


Figure 2.4: Optimized TPNC structures for IP and EA calculations. R groups (C and H atoms of SAdm ligands) are removed for clarity.

ping over 7e systems. Experimental efforts to synthesize the 7e $\text{Au}_{23}(\text{SAdm})_{16}$ by adjusting the synthetic conditions were not successful, and only when Cd(II) was used, could a 23-atom TPNC be obtained. In a previous periodic series (*i.e.*, $\text{Au}_{28}(\text{TBBT})_{20}$, $\text{Au}_{36}(\text{TBBT})_{24}$, $\text{Au}_{44}(\text{TBBT})_{28}$, and $\text{Au}_{52}(\text{TBBT})_{32}$), the free electron number increased from 8e, 12e, 16e to 20e with the same interval (4e).[73] Interestingly, the same 4e increment is observed for the series of $\text{Au}_{28}(\text{SR})_{20}$, $\text{Au}_{34}(\text{SR})_{22}$, and $\text{Au}_{42}(\text{SR})_{26}$ ($\text{SR} = \text{S-}i\text{-C}_6\text{H}_{11}$).⁴⁷ Note that in another series reported previously,[47] as more Ag atoms were doped into the kernel, the 6e $\text{Au}_{20}\text{Ag}_1(\text{SAdm})_{15}$ also transitioned to the 8e $\text{Au}_{19}\text{Ag}_4(\text{SAdm})_{15}$. The results of the new SAdm-protected series in the current work suggest that an even number of valence electrons is required,[74] even for atom-by-atom growth.

To probe the synthetically inaccessible 7e TPNCs, we modulated Cd-doping to create three theoretical structures (red dashed box in Figure 2.4). Furthermore, we studied two distinct $\text{Au}_{20}\text{Cd}_1(\text{SAdm})_{15}$ TPNCs (second denoted with *) in order to determine the effect of dopant location on IP and EA.

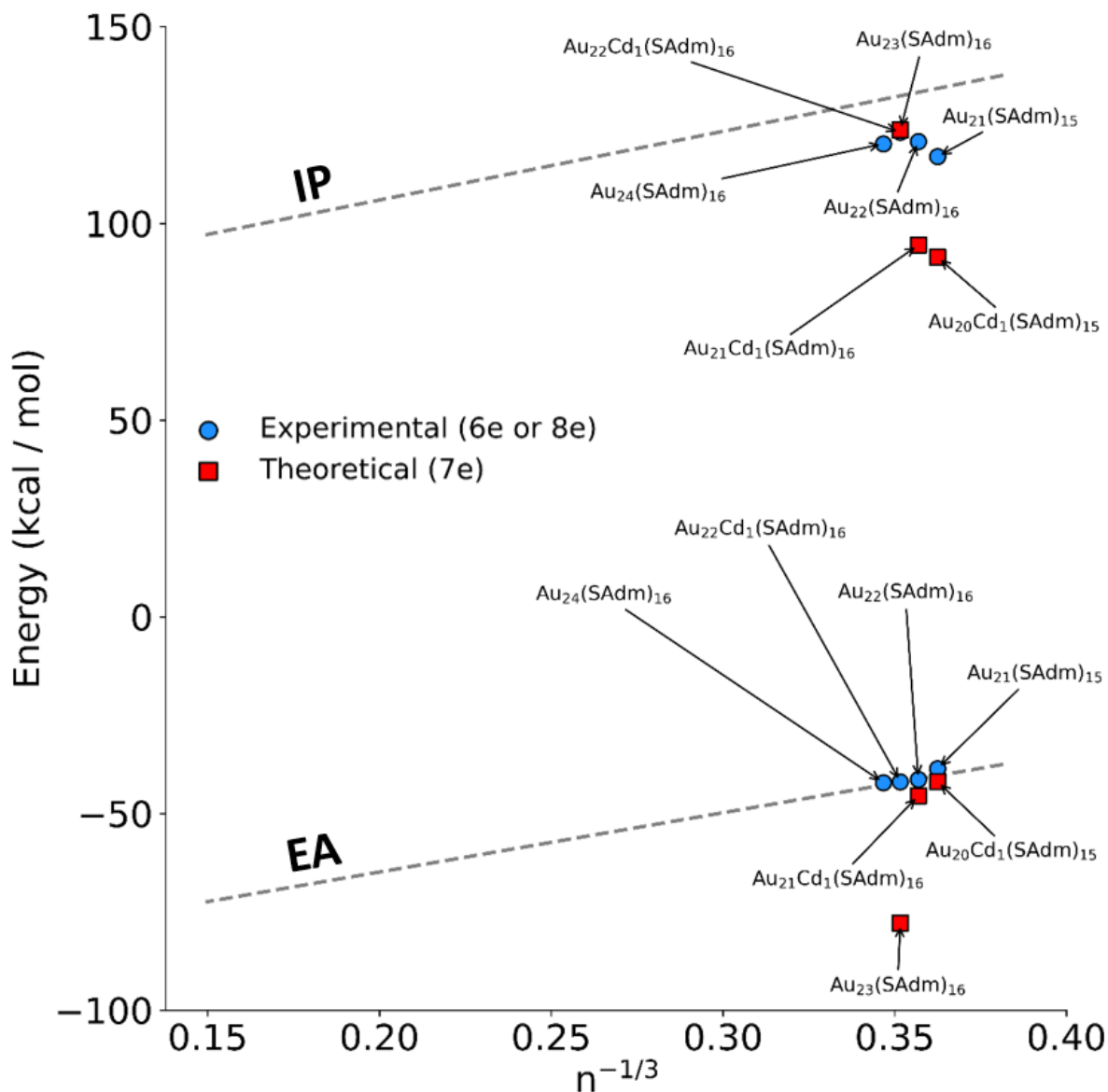


Figure 2.5: IP and EA (given in kcal mol⁻¹ of the $Au_nCd_x(SAdm)_m$ ($x = 0, 1$) TPNC series (blue circles) and theoretical 7e TPNCs (red squares) plotted against $n^{-1/3}$. The results are compared to our previously reported SPRs for neutral TPNCs (gray dashed lines; Figure 2.3)

2.2.3 Comparing IP and EA of TPNC Series to Known SPRs

Figure 2.5 shows the IP and EA for the TPNC series and their theoretical 7e derivatives compared to our previously developed SPRs. The results reveal that the Au_{21} - Au_{22} - $\text{Au}_{22}\text{Cd}_1$ - Au_{24} series follows the SPRs for stable structures. As to theoretical $\text{Au}_{20}\text{Cd}_1(\text{SAdm})_{15}$ and $\text{Au}_{21}\text{Cd}_1(\text{SAdm})_{16}$, their EAs follow the trend of the stable TPNCs (Figure 2.5, red circles), while their IPs deviate and have much lower energy compared to their 6e counterparts (Figure 5, blue circles). The results indicate that the theoretical 7e TPNCs do not intend to take in an electron to fulfill 8e shell closure, but prefer to lose an electron and achieve the same configuration as their stable TPNC counterparts. Moreover, comparison of the additional $\text{Au}_{20}\text{Cd}_1(\text{SAdm})_{15}^*$ revealed that dopant location does not play a role in IP and EA (Figure 2.5). The result aligns with theory, as Cd placement should have little effect on these properties since IP and EA are each a cumulative response by the TPNCs (charges are delocalized). $\text{Au}_{23}(\text{SAdm})_{16}$, on the other hand, shows almost identical IP as the stable $\text{Au}_{22}\text{Cd}_1(\text{SAdm})_{16}$, but much lower EA than its 8e counterpart, proving that an additional electron is desired by the 23-Au-atom TPNC.

Overall, the analysis demonstrates why 7e TPNCs cannot be readily prepared. We note that the 7e $\text{Au}_{25}(\text{PET})_{18}$ has been synthesized, but it was done so by air oxidation of its anionic 8e counterpart,[25] which only suggests that 7e TPNCs can form through redox chemistry on charged TPNCs. Further, the 7e $\text{Au}_{25}(\text{PET})_{18}$ was shown to spontaneously transform to $\text{Au}_{38}(\text{PET})_{24}$ in solution (at 65°C, as shown in the Supporting Information of Dainese *et. al.* [75]), revealing a decrease in stability relative to its 8e counterpart ($[\text{Au}_{25}(\text{PET})_{18}]^-$).

The agreement between experimentally accessible structures and our IP and EA SPRs supports the use of these models as stability metrics for neutral TPNCs. Furthermore, probing theoretical 7e TPNCs through Cd–Au replacement revealed that the IP and EA models can distinguish stability for heterometal-doped TPNCs.

2.3 Conclusions

In this chapter, we utilized systematic analyses to extend, develop, and apply SPRs – mainly towards TPNC stability. First, we demonstrated that the TSM is applicable across the complete spectrum of TPNC sizes. Indeed, the model verified the thermodynamic stability of the recently experimentally synthesized $\text{Au}_{146}(\text{SR})_{57}$, $\text{Au}_{246}(\text{SR})_{80}$, and $\text{Au}_{279}(\text{SR})_{84}$ TPNCs. Using those results from our DFT calculations, we also developed new SPRs that connect IP and EA to the number of metal atoms in Au TPNCs. These new SPRs were then used to probe the stability for an atom-by-atom evolution TPNC series. This approach was done by modulating the free electron count in the neutral series through Cd-doping (*i.e.*, shifting from 6e or 8e to 7e by adding or removing a Cd atom, respectively) to create a sample of experimentally inaccessible structures. By comparing the electronic properties of the structures, we found that the theoretical 7e systems deviate from the IP and EA SPRs while the 6e and 8e systems did not. The electronic “destabilization” of the 7e structures (relative to SPRs between stable TPNCs) rationalized why they are not experimentally observed.

3.0 Unraveling Distinct TPNC Properties Through Dipole Moments

The content of this chapter is adopted, in part, from:

- M. J. Cowan, T. Higaki, R. Jin, and G. Mpourmpakis. Understanding the solubility behavior of atomically precise gold nanoclusters. *The Journal of Physical Chemistry C*, 123:20006–20012, 2019.
- Y. Li*, M. J. Cowan*, M. Zhou, M. G. Taylor, H. Wang, Y. Song, G. Mpourmpakis, and R. Jin. Heterometal-doped M_{23} ($M = \text{Au/Ag/Cd}$) nanoclusters with large dipole moments. *ACS Nano*, 14:6599–6606, 2020.

3.1 Understanding TPNC Solubility Behavior

Among the physical properties of TPNCs, solubility has received little attention, yet it is critically important to many aspects of TPNC research. Examples include TPNC synthesis, where solvent can control thiolate-metal speciation and dictate product size,[76,77] as well as structural determination due to the sensitivity of solvent/nonsolvent pairs to successful TPNC crystallization.[78] Based on experimental observation, it is well known that the surface ligands largely determine the solubility of TPNCs, that is, organic soluble thiolate ligands (-SR) lead to TPNCs soluble in common organic solvents like toluene, and dichloromethane (DCM). However, atypical solubility has been observed for some TPNCs.[79,80] Thus, there is a need for systematic studies to elucidate general SPRs for TPNC solubility. In this work, we aim to understand the driving forces behind TPNC solubility.

*Authors contributed equally.

3.1.1 Computational Details

DFT calculations were implemented with the CP₂K package,[62] and were performed using the PBE[60] exchange–correlation functional with a 500 Ry energy cutoff, DZVP basis set, and GTH[61] pseudopotentials. PBE was selected due to its proven success in calculating electronic properties of TPNCs.[34,35,51] All TPNCs were centered in a non-periodic cubic box with a 7 Å minimum offset between the structure and boundary. The systems were then relaxed until interatomic forces were no greater than 0.02 eV/Å. Self-consistent field energies were converged to 10^{−7} Ha. The fully optimized structures were then used to calculate the electronic permanent dipole vectors and polarizability tensors of the TPNCs. Total electronic dipole moments were calculated based on the generation of maximally localized Wannier functions using the Berry phase scheme.[81,82] The dipole moment vectors (Table D.2) were found relative to the center-of-mass of each TPNC. Magnitudes of the dipole vectors (μ) were calculated by

$$\mu = \sqrt{\mu_x^2 + \mu_y^2 + \mu_z^2} \quad (3.1)$$

where μ_i is the i th (x, y, z) component of the dipole vector. Electronic polarizability tensor calculations were performed with the variational perturbation theory using a diagonalization-based preconditioned conjugate gradient approach.[83] The optimized TPNCs were placed in a polar environment, and the response wave functions were converged in a self-consistent manner to 10^{−6} Ha. The resulting tensors were diagonalized to find the molecular polarizabilities of each TPNC.[84] The average polarizability (α) and anisotropy ($\Delta\alpha$) were calculated as

$$\alpha = \frac{\alpha_{xx} + \alpha_{yy} + \alpha_{zz}}{3} \quad (3.2)$$

$$\Delta\alpha = \frac{1}{\sqrt{2}} \sqrt{(\alpha_{xx} - \alpha_{yy})^2 + (\alpha_{yy} - \alpha_{zz})^2 + (\alpha_{zz} - \alpha_{xx})^2} \quad (3.3)$$

where α_{jj} corresponds to the principal components (*i.e.*, diagonal terms) of the molecular polarizability.[84,85]

3.1.2 Typical *vs.* Atypical TPNC Solubility

We first list the experimental observations of solubility for ten TPNCs in Table 3.1. The results reveal the common solubility properties of TPNCs protected by aprotic thiolate ligands. Specifically, this class of TPNCs is typically soluble in toluene and DCM, but insoluble in protic solvents such as methanol and ethanol. These TPNCs are also generally insoluble in aprotic solvents with a relatively large dipole moment such as acetonitrile. Of particular note within Table 3.1 are the anionic $\text{Au}_{25}(\text{PET})_{18}$ stabilized with a tetraoctylammonium (TOA^+) counterion and $\text{Au}_{30}(\text{SAdm})_{18}$. For $[\text{Au}_{25}(\text{PET})_{18}]^-[\text{TOA}]^+$, we note that its neutral counterpart exhibits typical solubility, indicating the importance of the total charge state to solubility behavior. Interestingly, the $\text{Au}_{30}(\text{SAdm})_{18}$ TPNC is only soluble in nonpolar benzene, which is drastically different than the other two TPNCs protected by SAdm within this study (*i.e.*, $\text{Au}_{38}\text{S}_2(\text{SAdm})_{20}$ and $\text{Au}_{21}(\text{SAdm})_{15}$). We examine this atypical solubility behavior by first utilizing Hansen solubility parameters (HSPs), a similarity metric used to determine solubility between organic molecules.[86] In Figure 3.1, we plot HSPs of the solvents tested for $\text{Au}_{30}(\text{SAdm})_{18}$. By coloring the points based on solubility behavior of the TPNC, one can immediately see the distinct regions that appear in the HSP space. Taking the HSP of benzene as the reference point, we observe that as one traverses further away in the HSP space, the solubility behavior shifts to “slightly soluble” and then to insoluble. Although the results agree with experimental observations, they do not rationalize the unusual solubility behavior of $\text{Au}_{30}(\text{SAdm})_{18}$ when compared to other TPNCs. Instead, a more thorough analysis of all TPNCs presented in Table 3.1 is required that focuses on their inherent properties.

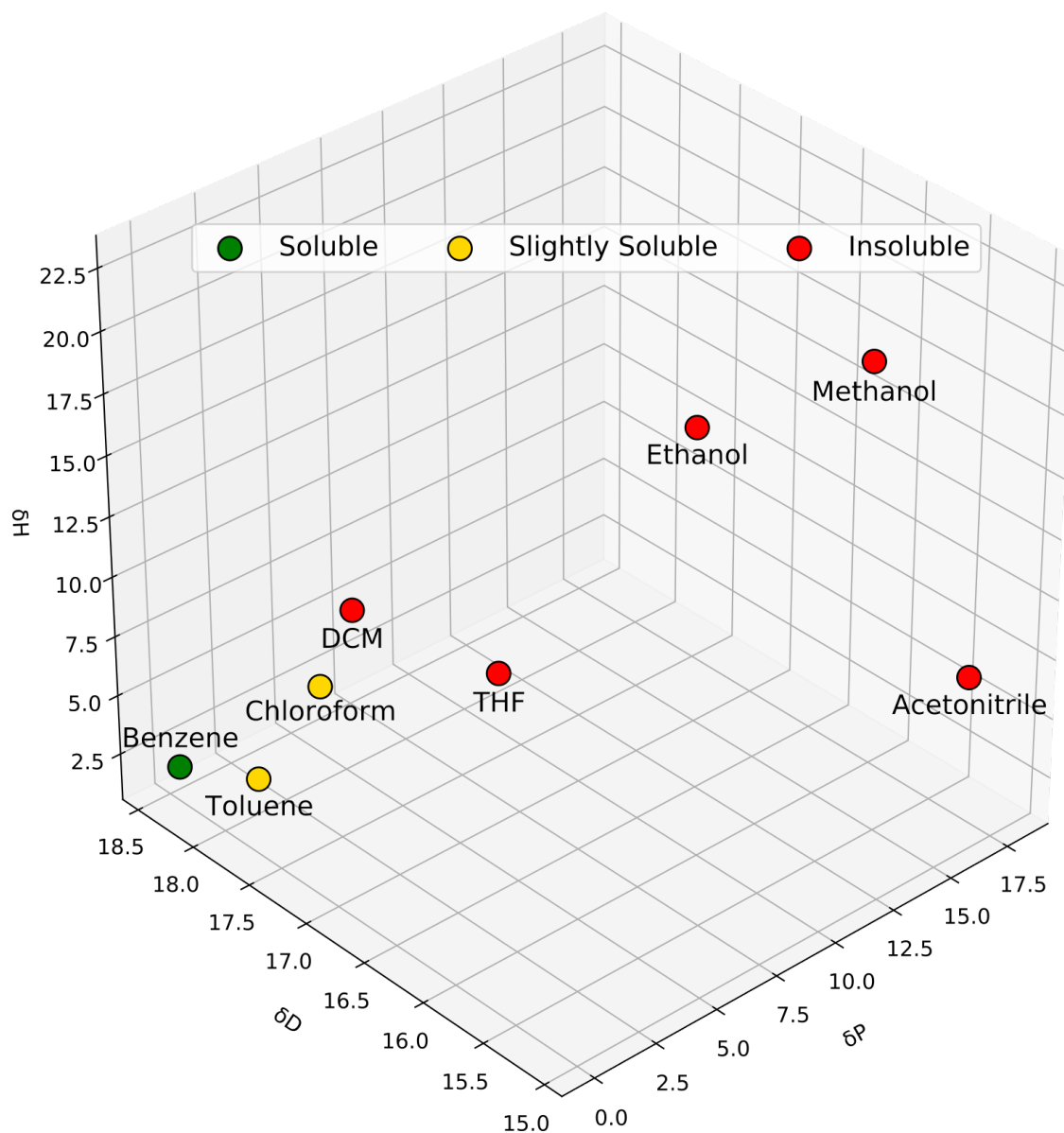


Figure 3.1: Comparing $\text{Au}_{30}(\text{SAdm})_{18}$ solubility behavior to Hansen solubility parameters of different solvents and nonsolvents. Different colors indicate experimentally observed solubility behavior.[87] The Hansen solubility parameters, δH , δD , and δP , represent energy contributions from hydrogen bond, dispersion, and polar interactions, respectively. All axes are in intensive (energy per volume) units of $\text{MPa}^{1/2}$.

Table 3.1: Experimental solubility behavior of ten TPNCs (including neutral and anionic forms of $\text{Au}_{25}(\text{PET})_{18}$). Ben: benzene, Tol: toluene, DCM: dichloromethane, MeOH: methanol, EtOH: ethanol, ACN: acetonitrile, ACE: acetone, THF: tetrahydrofuran.

*Described as “slightly soluble”

Name	Solvent	Nonsolvent	Ref(s)
$\text{Au}_{21}(\text{SAdm})_{15}$	Tol, DCM	MeOH, ACN	[34]
$\text{Au}_{25}(\text{PET})_{18}$	Ben, Tol, DCM	EtOH, ACN	[25, 80, 88]
$[\text{Au}_{25}(\text{PET})_{18}]^{-}[\text{TOA}]^{+}$	Ben, Tol, DCM, ACN	EtOH	[24, 80, 88]
$\text{Au}_{28}(\text{TBBT})_{20}$	Tol, DCM	MeOH, EtOH	[54, 89]
$\text{Au}_{30}(\text{SAdm})_{18}$	Ben	Tol*, Chloroform*, DCM, THF, MeOH, ACN, ACE	[79]
$\text{Au}_{30}\text{S}(\text{S-tBut})_{18}$	Tol, DCM, THF	MeOH, EtOH	[35, 90]
$\text{Au}_{36}(\text{TBBT})_{24}$	Tol, DCM	EtOH	[27, 89]
$\text{Au}_{38}\text{S}_2(\text{SAdm})_{20}$	Tol, DCM	MeOH	[36]
$\text{Au}_{40}(\text{o-MBT})_{24}$	Tol, DCM	MeOH	[29, 56]
$\text{Au}_{52}(\text{TBBT})_{32}$	Tol, DCM	MeOH	[56, 89]
$\text{Au}_{133}(\text{TBBT})_{52}$	Tol, DCM, THF	MeOH, EtOH, ACN	[6, 91]

3.1.3 Structural Observations

To understand the solubility properties of the TPNCs listed in Table 3.1, we optimized their experimentally determined structures using DFT. The ten (neutral) systems shown in Figure 3.2 represent a wide range of TPNCs varying in size (21 – 133 Au atoms), ligand type (five different organic ligands), and shape (*i.e.*, symmetry).

Studying TPNCs with similar structural properties but different solubility behavior enables us to systematically examine the role that specific physicochemical properties play in solubility. For example, from Table 3.1 one can observe that TPNCs protected by TBBT are found to have typical solubility, independent of size. However, this trend breaks down when

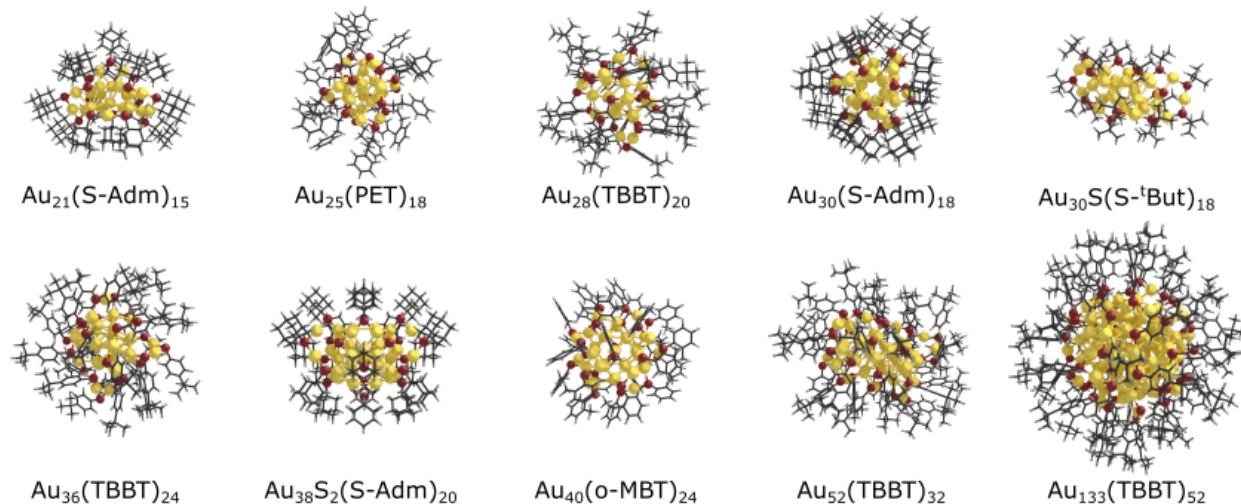


Figure 3.2: TPNCs fully optimized with DFT. Gold and red balls correspond to Au and S atoms, respectively. Black and white sticks represent hydrocarbon ligands.

one looks at SAdm-protected TPNCs. In fact, there appears to be no correlation between solubility and size, suggesting that the solubility behavior of TPNCs is size-agnostic. Focusing on TPNC shape instead leads to some interesting comparisons between structures. For instance, the atypical solubility behavior of $\text{Au}_{30}(\text{SAdm})_{18}$ could be attributed to its relatively high symmetry (*i.e.*, S_6 point group).[79] The only TPNC with a higher order of symmetry is the $\text{Au}_{25}(\text{PET})_{18}$ (D_{2h} point group). However, the anionic form of the $\text{Au}_{25}(\text{PET})_{18}$ is stabilized by the presence of a TOA^+ counterion. Due to the equal concentrations of nanocluster and TOA^+ in solution, the counterion must be considered when examining TPNC symmetry. Thus, the presence of TOA^+ breaks the D_{2h} symmetry of the system. Furthermore, the loss of an electron to form the neutral $\text{Au}_{25}(\text{PET})_{18}$ results in a slight distortion of the structure. This distortion arises from the open-shell $1\text{S}^21\text{P}^5$ superatom electron configuration.[92] Therefore, our qualitative observations suggest that symmetry plays a key role in TPNC solubility behavior.

3.1.4 Connecting Molecular Properties to Solubility Behavior

Permanent dipole moment of solutes can affect their solubility behavior.[93] Additionally, dipole moment serves as a means to address symmetry effects in charge distribution on a chemical structure. Therefore, we calculated the total electronic dipole moment of each TPNC (Figure 3.3) to quantitatively analyze these effects connecting TPNC symmetry to solubility behavior. Of the 10 neutral TPNCs studied (shown in Figure 3.3a), $\text{Au}_{38}\text{S}_2(\text{SAdm})_{20}$ exhibits the largest dipole moment of 4.31 Debye (D). This can be attributed to the two μ_3 -sulfido atoms located on a single side of the TPNC, leading to C_{2v} symmetry.[36] The presence of non-symmetrically (*i.e.*, lacking a horizontal mirror plane) distributed sulfido atoms strongly influences the dipole moment as also indicated by $\text{Au}_{30}\text{S}(\text{S}^t\text{But})_{18}$, which has a large dipole of 3.50 D. However, in the absence of sulfido atoms, TPNC symmetry appears to play the major role. In fact, the orientation of the protecting thiolate ligands can have a significant impact on the resulting electronic dipole of TPNCs, which becomes apparent in the largest TPNC that we investigated. $\text{Au}_{133}(\text{TBBT})_{52}$ has a highly symmetric Mackay icosahedral Au core, but its “swirly” distribution of surface ligands breaks the total symmetry of the system.[6] Thus, we find that $\text{Au}_{133}(\text{TBBT})_{52}$ exhibits the second largest dipole moment of 3.76 D. Although the anionic state of the $\text{Au}_{25}(\text{PET})_{18}$ TPNC has been reported to have higher symmetry than the neutral,[92, 94] the presence of the TOA^+ counterion must be considered when calculating its dipole moment calculation. As previously stated, this is due to $[\text{Au}_{25}(\text{PET})_{18}]^-$ and TOA^+ having equivalent concentrations in solution. Thus, there are 1:1 electronic interactions exhibited between the TPNCs and counterions which must be accounted for. Although the counterion and the anionic TPNC are expected to be solvated in solution, decreasing their intermolecular interactions (compared to gas phase), a dipole is expected to be developed because a negative charge is equilibrated in the vicinity of a positive charge in solution. As a result, including TOA^+ in our calculation generates a strong electronic dipole of 22.91 Debye (Figure 3.3b). We note that strong interactions also exist due to the TPNC charge and the dipole of the solvent. However, for the purposes of gaining trends with a single TPNC descriptor, we can capture these charge effects through our electronic dipole moment calculations, where the dipole moment becomes

significant between two point charges (charged TPNC and counterion). The drastic increase in the dipole moment explains why $[\text{Au}_{25}(\text{PET})_{18}]^{-}[\text{TOA}]^{+}$ has the unique ability to dissolve in the highly polar acetonitrile. Additionally, the result reveals the importance that the charge state of TPNCs has on their solubility properties. This is especially significant for larger TPNCs because determining the correct charge for some of these systems has been shown to be a difficult task.[57, 59]

As previously mentioned, $\text{Au}_{30}(\text{SAdm})_{18}$ exhibits the second highest order symmetry of the TPNCs studied herein. As a further indication of high symmetry, the $\text{Au}_{30}(\text{SAdm})_{18}$ was found to be perfectly nonpolar with a calculated dipole moment of 0.00 D. The lack of dipole can easily be realized through visualizing the electron density and charge distribution within the TPNC. Figure C.1 reveals symmetric charge density that can be seen through a continuum of charge isosurfaces (Figure C.1a) as well as atomic point charges (Figure C.1b). The result is in striking contrast to the polar $\text{Au}_{21}(\text{SAdm})_{15}$ and $\text{Au}_{38}\text{S}_2(\text{SAdm})_{20}$ TPNCs that are stabilized with the same type of ligands. Moreover, the results for SAdm-protected TPNCs strongly agree with the experimental observations, suggesting that the presence of an electronic dipole moment is essential for a TPNC to exhibit typical solubility behavior (*i.e.*, soluble in toluene and DCM). However, the neutral $\text{Au}_{25}(\text{PET})_{18}$ also exhibits no dipole with a calculated value of 0.04 D, yet it follows typical TPNC solubility. Therefore, although important, the permanent dipole moment alone does not completely explain Au-based TPNC solubility behavior.

Because polarizability has been shown to be a key factor in solubility behavior of molecular systems,[95–97] we calculated the molecular electronic polarizability of the 10 TPNCs. As expected based on previous work with organic molecules,[85] we found a strong linear correlation between the average polarizability and the size of each system (using the number of electrons in each system as a descriptor), as shown in Figure C.2. Furthermore, Figure C.2 reveals that for TPNCs with the same ligand type (SAdm and TBBT), we find perfect linear relationships but with different slopes. The slight difference in slope can be attributed to the difference in saturation of hydrocarbons between ligand types.[85]

In an effort to further understand the polarizability behavior of the TPNCs we examine the anisotropy of the polarizability as shown in Figure 3.4. One can immediately see the

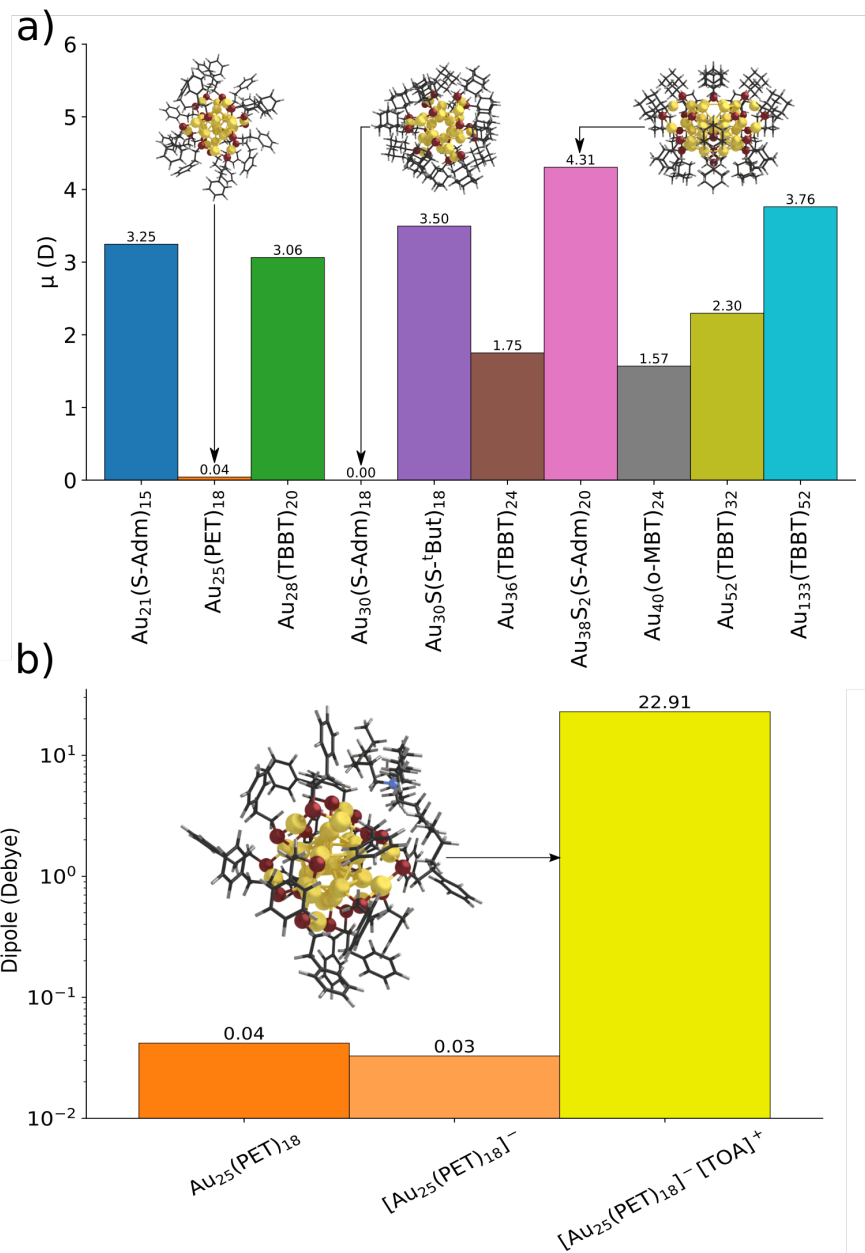


Figure 3.3: Magnitude of total electronic dipole moment vectors (in Debye, D) for (a) 10 neutral TPNCs (in the order of increasing number of Au) and (b) Au₂₅(PET)₁₈ in the neutral and anionic charge states and in the presence of a tetraoctylammonium (TOA⁺) counterion (inset structure). The structures exhibiting the minimum (Au₂₅(PET)₁₈ and Au₃₀(SAdm)₁₈) and maximum (Au₃₈S₂(SAdm)₂₀) permanent dipoles are shown as insets in the left panel.

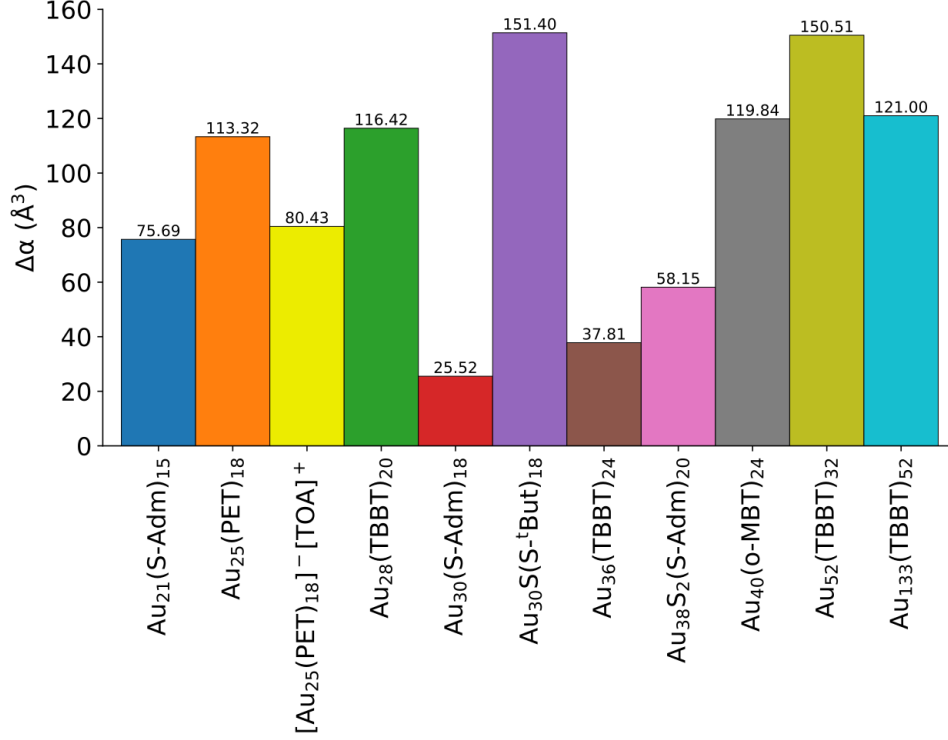


Figure 3.4: Anisotropy in polarizability ($\Delta\alpha$) of TPNCs in the order of increasing number of Au atoms. Anisotropy is given in units of \AA^3 .

unique character of the nonpolar $\text{Au}_{30}(\text{SAdm})_{18}$ TPNC as it is found to exhibit the lowest anisotropy at 25.52 \AA^3 . This is in stark contrast to the other nonpolar TPNC studied, the neutral $\text{Au}_{25}(\text{PET})_{18}$, as it has an anisotropy that is over three times greater (80.43 \AA^3). This difference in $\Delta\alpha$ can rationalize the unique behavior of the two TPNCs, $\text{Au}_{30}(\text{SAdm})_{18}$ and $\text{Au}_{25}(\text{PET})_{18}$. Specifically, to relate these results to solubility, we first note our assumption that in solution, each of the two TPNCs experiences a uniform and symmetric solvation environment. This is a legitimate assumption accounting for the fact that each TPNC is protected by a single ligand type, and the ligand coverage is generally uniform across the TPNC surface (supported by the aforementioned nano-scaling law, where the number of surface ligands scales with the number of Au atoms on $\text{Au}_n(\text{SR})_m$ TPNCs, as $m \propto n^{2/3}$). [40,42] As a result, a larger anisotropy in polarizability would lead to a stronger induced dipole within a TPNC. This outcome is due to the electronic structure of a TPNC becoming

polarized through intermolecular interactions with the solvent in an increasing manner for systems that exhibit higher anisotropy in polarizability. Thus, because $\text{Au}_{30}(\text{SAdm})_{18}$ is closer to isotropic polarizability, it experiences a smaller induced dipole in solution, which suggests its inability to dissolve in solvents with a permanent dipole moment, such as DCM and toluene. In contrast, the larger anisotropy of the neutral $\text{Au}_{25}(\text{PET})_{18}$ would experience a greater induced dipole, leading to its solubility in toluene and DCM.

To further rationalize TPNC solubility trends with our electronic property calculations, we plot dipole moment, anisotropy, and experimental solubility behavior in Figure 3.5. The plot demonstrates the clear distinctions that differentiate $\text{Au}_{30}(\text{SAdm})_{18}$ and $[\text{Au}_{25}(\text{PET})_{18}]^{-}[\text{TOA}]^{+}$ from TPNCs with typical solubility. In fact, by defining regions on Figure 3.5 that correspond to different solubility behaviors, we reveal an excellent agreement between our computational results and the experimental observations. Moreover, our findings suggest that dipole moment and anisotropy can be used in concert as parameters to predict the solubility behavior of all Au nanoclusters protected by aprotic, thiolate ligands. The approach can also be applied to other metal TPNCs. For instance, $[\text{Ag}_{25}(\text{SR})_{18}]^{-}[\text{PPh}_4]^{+}$, protected by $\text{SR} = 2\text{-4dimethylbenzenethiolate}$, has been successfully synthesized and was found to be an analogue to anionic $\text{Au}_{25}(\text{PET})_{18}$ (*i.e.*, same shape and symmetry).[98] It also shares similar solubility behavior to its Au counterpart. Specifically, the Ag TPNC is soluble in aprotic solvents (DCM, dimethylformamide, dimethyl sulfoxide, and toluene) and insoluble in methanol. Additionally, the Ag TPNC is soluble in a 1:1 v/v solution of DCM and acetonitrile,[98] supporting the role that the charge state plays in solubility behavior. Our methods can also be extended to heterometal-doped TPNCs. To test the effect of heterometal doping, we created a theoretical $\text{Au}_{29}\text{Ag}(\text{SAdm})_{18}$ TPNC, by replacing a shell Au with Ag, and compared its dipole moment and anisotropy to $\text{Au}_{30}(\text{SAdm})_{18}$ (Table 3.2). Doping a Ag atom in the shell of the TPNC breaks its symmetry, thus creating a permanent dipole moment (from 0.00 to 0.852 D). However, there is almost no change in the anisotropy of the system. Nevertheless, since both properties are vital to solubility, the results still suggest that heterometal doping could provide a means of control over the solubility behavior of TPNCs.

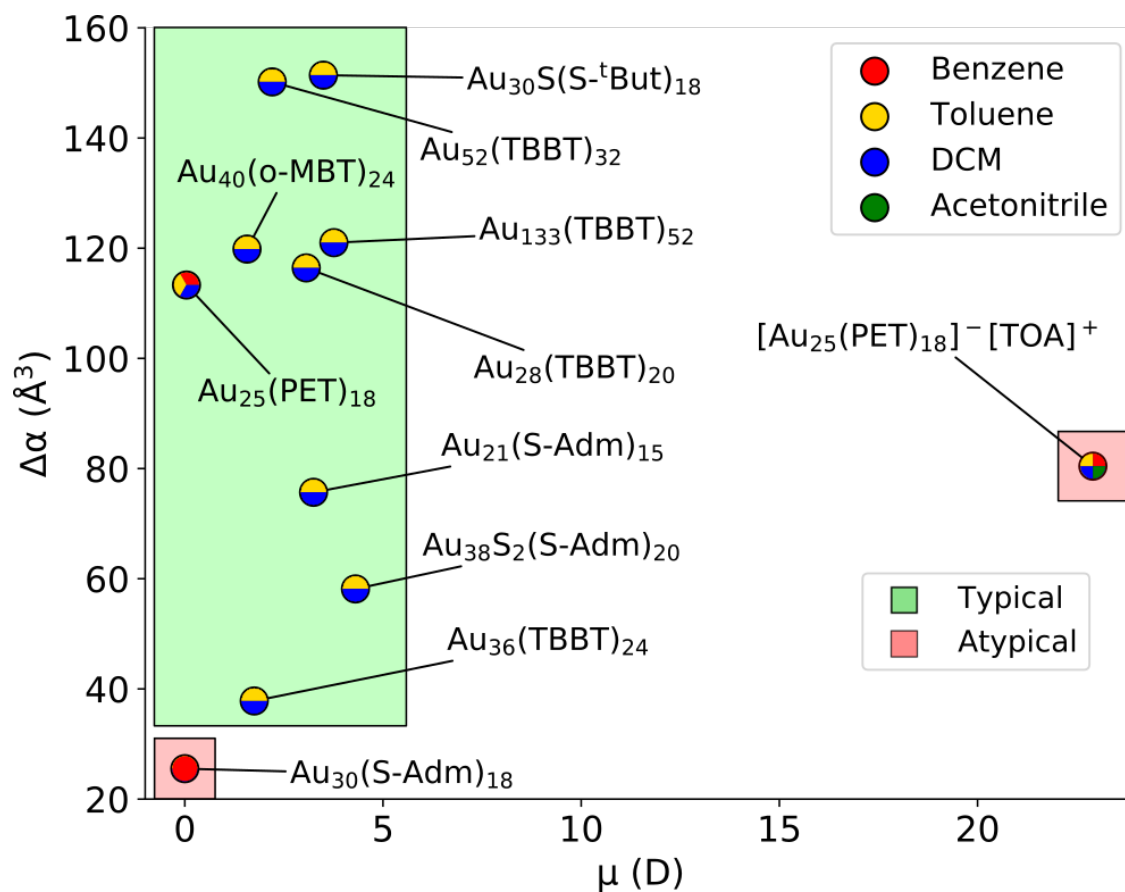


Figure 3.5: Comparing permanent dipole moment and anisotropy to TPNC solubility behavior. Data point colors indicate observed solvents for each TPNC (based on Table 3.1). Boxes represent regions of typical (green) and atypical (red) solubility behavior.

Table 3.2: Comparing a theoretical $\text{Au}_{29}\text{Ag}_1(\text{SAdm})_{18}$ and its monometallic counterpart.

Property	$\text{Au}_{30}(\text{SAdm})_{18}$	$\text{Au}_{29}\text{Ag}_1(\text{SAdm})_{18}$
μ (D)	0.00	0.852
$\Delta\alpha$ (\AA^3)	25.52	26.40

3.2 Towards TPNC Self-Assembly: Rationalizing Large Dipoles in a M_{23} Series

TPNCs are promising candidates for self-assembled supramolecular structures due to their advantageous properties and atomic precision.[1] However, controlling their assembly is a major challenge.[99] Importantly, other nanomaterials have achieved self-assembly through strong dipole-dipole interactions.[100] In the previous Section (3.1), we highlight the role of electronic properties on physical TPNC behavior. Following a similar logic, our next work[101] investigated a M_{23} TPNC series that all exhibit significantly large dipole moments ($\mu > 10$ Debye) relative to neutral TPNCs in the same size regime ($\mu = 0\text{--}5$ Debye, as shown in Figure 3.5). Specifically, we rationalized the origin of these large permanent dipoles and connected them to unique physical and optical properties, namely alignment in the crystalline state and solvatochromism, respectively. Our results highlight the potential for self-assembly of TPNC supramolecular structures driven by dipole-dipole interactions.

3.2.1 Computational Details

All DFT calculations were performed in Turbomole v7.2[72] following the same methods described in Section 2.2.1. Initial structures were taken from the experimentally determined crystalline structures reported in our work[101] and in literature.[47] Ligands were substituted to methylthiolate ($\text{SR} = \text{SCH}_3$). After geometry relaxations, electronic dipole moments (μ) were determined using Turbomole. Atomic charges were calculated using the natural bond orbital (NBO) analysis,[102] as implemented in Turbomole.

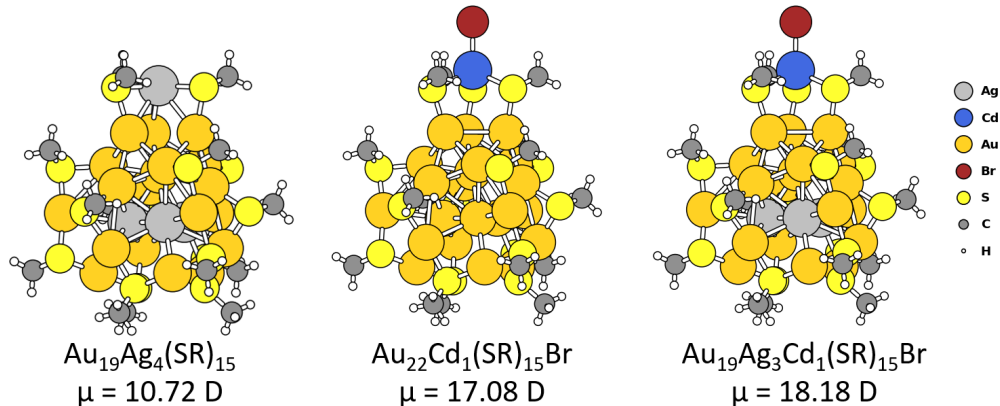


Figure 3.6: Optimized structures and calculated dipole moments (μ) of $\text{Au}_{19}\text{Ag}_4(\text{SR})_{15}$, $\text{Au}_{22}\text{Cd}_1(\text{SR})_{15}\text{Br}$, and $\text{Au}_{19}\text{Ag}_3\text{Cd}_1(\text{SR})_{15}\text{Br}$ ($\text{SR} = \text{SCH}_3$).

3.2.2 Large Dipole Moments

The M_{23} TPNC series, shown in Figure 3.6, all possess quasi- C_3 symmetry with an icosahedral M_{13} kernel ($\text{M} = \text{Ag}, \text{Au}$) protected by three trimer motifs ($\text{Au}_3(\text{SR})_4$) and a “capping” $\text{Y}(\text{SR})_3$ motif at the top ($\text{Y} = \text{Ag}, \text{Cd-Br}$). The structures enable systematic comparison, which reveals the importance of the $\text{Cd}_1(\text{SAdm})_3\text{Br}$ motif in achieving giant dipole moments in these systems. However, only acknowledging the presence of heterometals does not take into account symmetry effects, which was found to be crucial for μ in our solubility work (Section 3.1).

To obtain deeper insight into the unusually high μ of the M_{23} TPNCs, we sought for NBO charge analysis.[102] As shown in Figure 3.7, significant ground state electron transfer is observed in the M_{23} series, which is in large part due to the heterometals. Not only can the negative and positive centers be clearly observed in the M_{23} series, but the polar bonds are oriented in the same direction, hence giving rise to very high total dipole moments. In other words, the charge separation is mainly along the quasi- C_3 axis of the M_{23} series (*i.e.*, axis along Cd-Br bond in $\text{Au}_{22}\text{Cd}_1(\text{SR})_{15}\text{Br}$), resulting in a large μ along this principal axis. These results explain why the trimetallic TPNC exhibits the largest μ since its arrangement of heterometals, and thus ground state charge transfer, are all along the quasi- C_3 axis.

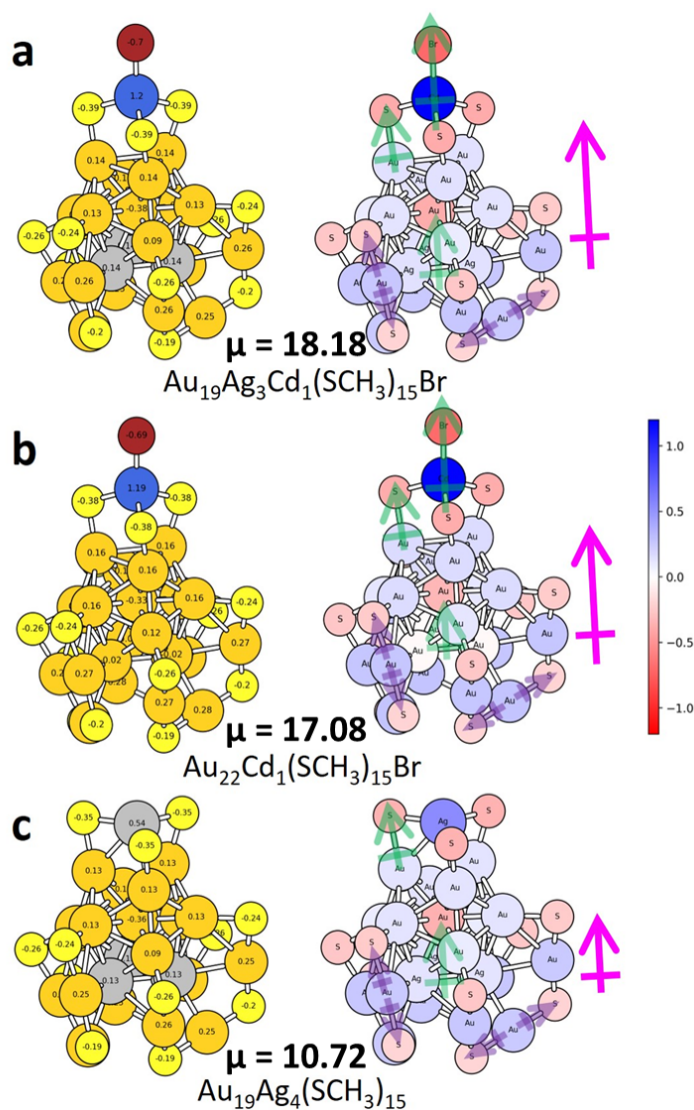


Figure 3.7: Optimized structures with calculated μ and NBO charge analysis for (a) $\text{Au}_{19}\text{Ag}_3\text{Cd}_1(\text{SR})_{15}\text{Br}$, (b) $\text{Au}_{22}\text{Cd}_1(\text{SR})_{15}\text{Br}$, and (c) $\text{Au}_{19}\text{Ag}_4(\text{SR})_{15}$. Ligands are omitted for clarity. NBO charges are labeled (left) and marked by color (right, blue = positive and red = negative). Selected dipoles along the C_3 axis are indicated by green arrows which contribute to μ (magenta arrows); Local dipoles that are expected to cancel out are indicated by purple arrows.

3.2.3 Connecting to Crystalline Alignment and Solvatochromism

It is important to note that the TPNCs in the M_{23} series are synthesized by modulating heterometal concentrations. Thus, the series offers tunable dipole moments while maintaining a similar overall structure. Upon further analysis of the M_{23} series, we can understand some unique physical and optical properties that emerge in the structures due to their large dipole moments. For example, high μ leads to interesting alignment of TPNCs in the experimentally determined crystals (Figure C.3). Specifically, the trimetallic $\text{Au}_{19}\text{Ag}_3\text{Cd}_1(\text{SAdm})_{15}\text{Br}$ TPNCs, which exhibit the largest dipole ($\mu = 18.18$ D), are aligned into “head-to-tail” cluster chains. Crystals of the subsequent TPNCs in the series move further from this “head-to-tail” arrangement based on their respective μ . Therefore, tuning μ enables control over TPNC alignment, revealing the potential of μ as a tunable property towards self-assembled TPNC supramolecular materials. In addition to structure alignment, the large dipoles explained the solvatochromic effects observed for these TPNCs. Shifts in experimental UV-Vis absorption spectrum peaks were found to linearly correlate with solvent polarity parameters, supporting strong μ - μ interactions between TPNC and solvent.

3.3 Conclusions

In this chapter, we first used DFT calculations to rationalize the solubility behavior of 10 TPNCs. Our results show the essential roles that permanent dipole moment and polarizability play in determining which solvents can dissolve a given TPNC. $\text{Au}_{30}(\text{SAdm})_{18}$, a TPNC with atypical solubility, was found to be nonpolar and additionally has extremely low anisotropy, which leads to its inability to dissolve in polar organic solvents. Neutral $\text{Au}_{25}(\text{PET})_{18}$ was also found to be nonpolar, but it exhibits high anisotropy. This finding suggests that a dipole can be induced in the TPNC, explaining why it can dissolve in the common TPNC solvents, that is, toluene and DCM. Importantly, our calculations rationalize a series of experimental observations with regards to the solubility behavior of TPNCs that exhibit diverse structures (*i.e.*, size, shape, and ligands). Our study offers a rapid and powerful means to address solubility trends within different TPNCs by calculating their electronic properties, such as dipole moment and polarizability.

In a similar manner, we also employed DFT to determine significantly large permanent dipole moments within a M_{23} alloy TPNC series. The three TPNCs, $\text{Au}_{19}\text{Ag}_3\text{Cd}_1(\text{SAdm})_{15}\text{Br}$, $\text{Au}_{22}\text{Cd}_1(\text{SAdm})_{15}\text{Br}$, and $\text{Au}_{19}\text{Ag}_4(\text{SAdm})_{15}$, had dipole moments of 18.18 D, 17.08 D, and 10.72 D, respectively. The large dipoles were explained through NBO charge analysis as well as symmetry and heteroatom arrangement arguments. Furthermore, the TPNC dipole moments were connected to experimentally observed behavior: alignment in the crystalline state and solvatochromic effects.

4.0 Decoding Chemical Ordering in Alloy TPNCs

The content of this chapter is adopted, in part, from:

- M. J. Cowan*, A. V. Nagarajan*, and G. Mpourmpakis. Correlating structural rules with electronic properties of ligand-protected alloy nanoclusters. *Journal of Chemical Physics*, 155:024303, 2021.

4.1 Correlating Structural Rules with IP and EA of Alloy TPNCs

Despite having a vast domain of materials space for exploration upon heterometal doping, there is a dearth of bimetallic TPNCs that have proven to show enhanced characteristics for different applications. Although some efforts have been made,[69] developing SPRs for bimetallic TPNCs has not been sufficiently explored and provide great promise in the field of nanoscience. From an experimental standpoint, such a task can be time-consuming and expensive thus leading to a rather impractical and complex approach. On the other hand, computational methods such as DFT offer an accelerated approach to nanomaterials discovery through SPR development at a small fraction of experimental time and expense. For example, Panapitiya *et. al.* developed a machine learning model that captures DFT CO adsorption energy on AgAu TPNCs.[103] The model was trained on a dataset of hypothetical alloy structures and importantly was found to work across a range of different TPNC sizes. Following in a similar path, in this study, we perform DFT calculations to explore structural effects on electronic properties, specifically IP and EA, of our own AgAu TPNC dataset. The main goal is to extend our previously developed SPRs (Section 2.1.3) to capture trends in alloy TPNCs.

*Authors contributed equally.

4.1.1 Computational Details

All electronic structure calculations were performed at the DFT level using CP₂K v6.1.[62] The PBE[60] functional in conjunction with a DZVP basis set, GTH pseudopotentials,[61] which importantly capture relativistic effects in the heavy elements, and 500 Ry cutoff was used to describe the electronic structure of all systems. All TPNC structures were positioned in the center of a computational box that awarded at least 7 Å of space from the walls. A convergence criterion of 0.025 eV Å⁻¹ was used for all geometry optimizations with a self-consistent field (SCF) threshold of 10⁻⁷ Ha. We note that the same methodology has been previously employed in literature to capture electronic properties of TPNCs.[104–106] All TPNCs possess a total charge of 0. Vertical IPs and EAs were calculated per Equations 2.1 and 2.2, respectively, wherein the electronic energies of the TPNCs in their (-1) or (+1) charge state were subtracted from the electronic energy of the neutral TPNCs ($q = 0$).

4.1.2 Generating the Bimetallic TPNC Dataset

We created bimetallic TPNCs by modulating the experimentally determined Au₃₆(SR)₂₄, Au₁₀₂(SR)₄₄, Au₂₄₆(SR)₈₀, and Au₂₇₉(SR)₈₄ structures.[23,27,58,59] Examples of each TPNC size are shown in Figure 4.1. The four structures exhibit FCC cores protected by combinations of similar staple motifs (bridging thiolates, monomers, and/or dimers; Figure 4.2 and Table D.1). Furthermore, they encompass the size regime where TPNCs display a sharp transition from molecular-like to metallic behavior (*i.e.*, Au₂₄₆ to Au₂₇₉).[107] To reduce computational cost while maintaining the accuracy of DFT calculations, we used -SCH₃ (methylthiolate) ligands as protecting groups on the surface of the TPNCs. This approach has been widely utilized to capture the electronic properties of TPNCs.[45, 50, 51] Ag was used as a dopant to create different hypothetical TPNC structures due to the synthetic accessibility across Ag-Au compositions in literature.[47, 108–110] Specifically, 9 different compositions (approximately 10% increments; see Table C.1 for exact compositions) and 10 different chemical orderings at each composition were chosen to create the materials domain. The chemical orderings were generated randomly to ensure uniform sampling of the bimetallic configuration space. Our efforts resulted in a final dataset of 368 unique TPNCs.

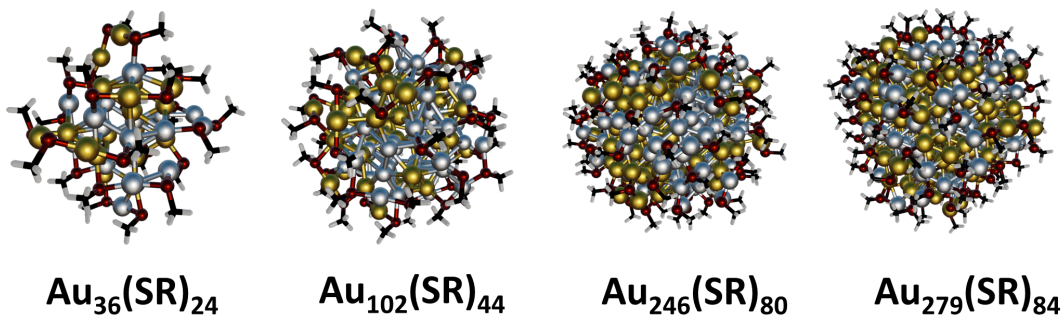


Figure 4.1: Examples of the different TPNC sizes used in this study. The selected samples have 50% Ag composition and a randomly generated chemical ordering. Color scheme: Au: yellow, Ag: grey, S: red, C: black, H: white.

4.1.3 Exploring IP/EA Trends

After generating the hypothetical AgAu TPNC dataset, we performed DFT calculations to optimize each of the 368 structures. We then calculated vertical IP and EA of each system (Equations 2.1 and 2.2, respectively; see Section 4.1.1 for calculation details). Before attempting to build general SPRs that can predict these properties, we sought to first explore the data by visualizing IP *vs.* EA for each TPNC, as shown in Figure 4.3. Immediately from the plot, one can observe that metal composition (color of data points) systematically affects the TPNC electronic properties. The general trend reveals that higher concentrations of Ag lead to a higher IP and more negative (favorable) EA. Of note, the results follow an opposite trend compared to atomic Ag and Au ($\text{IP}_{\text{Ag}} < \text{IP}_{\text{Au}}$ and $\text{EA}_{\text{Ag}} > \text{EA}_{\text{Au}}$ for metal atoms). Furthermore, the IP does not align with the trend between metal work functions ($\phi_{\text{Ag}} < \phi_{\text{Au}}$).^[111] Previous work revealed that Ag and Au exhibit different interactions with thiolate ligands,^[112] which could play a role in this counterintuitive behavior (*i.e.*, increased charge transfer from Ag to ligand through Ag-S bond could make it more difficult to donate an electron and cause higher IP). However, the M_{36} TPNC does not follow the general IP trend and instead exhibits minimal change in IP across compositions, with the monometallic systems (points with black border) showing approximately the same IP. Since

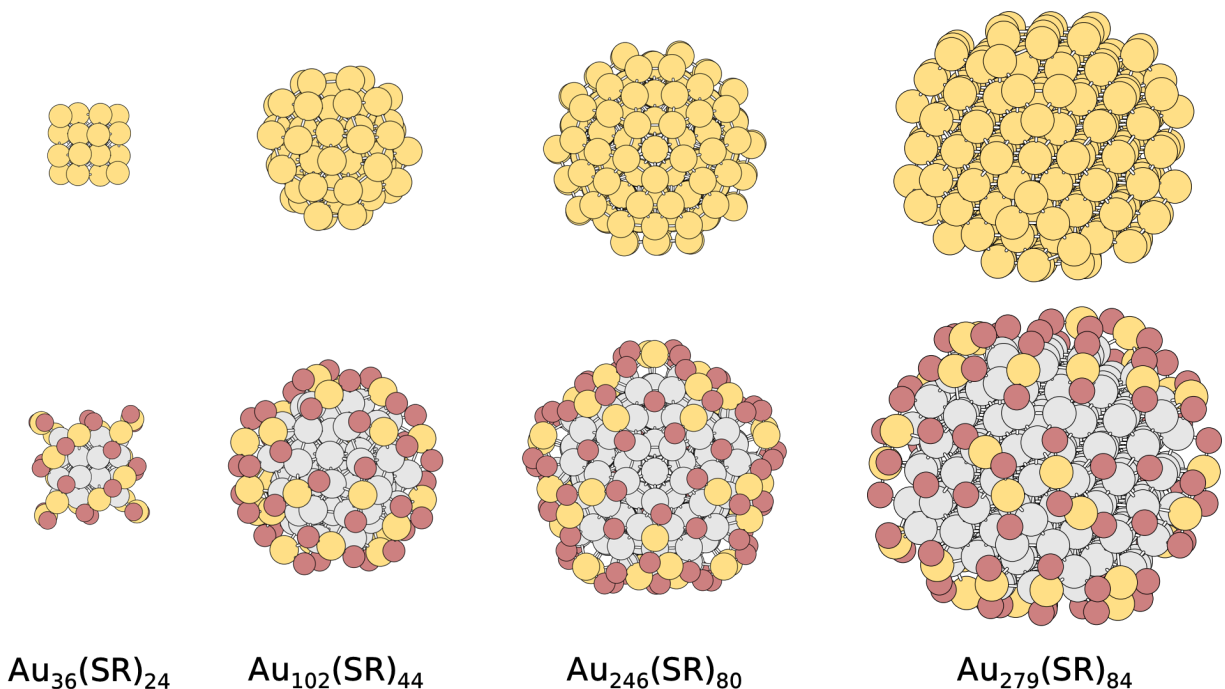


Figure 4.2: Demonstration of FCC cores (top row) and shell motifs (bottom row; core atoms shown in light gray for contrast) of the four Au TPNCs used to generate the hypothetical AgAu TPNC dataset in Chapter 4 (see Section 4.1.2 for more details on the dataset). Color scheme: Au: yellow, S: red. R groups omitted for clarity.

IP and EA relate to HOMO and LUMO energies,[113] respectively, the results suggest that Ag-doping the $\text{Au}_{36}(\text{SR})_{24}$ increases the LUMO energy while preserving the HOMO energy of the system – an observation reported for other Ag-doped TPNCs of similar size.[114] These interesting findings can be further explored by comparing between TPNC sizes. Based on Figure 4.3, there is a clear, converging behavior in the electronic properties, which occurs as TPNC size increases. Indeed, at smaller sizes, dopant position (*i.e.*, chemical ordering) plays a significant role in the electronic properties, which is highlighted by the spread of M_{36} and M_{102} points in Figure 4.3. This result is due to the emergence of quantum confinement effects and discrete electronic states within the smaller-sized TPNCs. As we move to the larger systems, the orbitals lose their discrete energies and localization, becoming more

diffuse and causing the emergence of band-like behavior (*i.e.*, towards metallic behavior). Thus, M_{246} and M_{279} TPNCs do not experience chemical ordering effects on EA and IP due to the dominating influence of bulk core atoms. Instead, the larger structures follow a composition-dependent $IP \propto -xEA$ trend, where $x \approx 1$. Overall, the results reveal the importance of understanding core-shell makeup for electronic properties of AgAu TPNCs, especially at smaller size regimes with molecular-like electronic behavior.

4.1.4 Extending IP/EA SPRs to capture AgAu TPNCs

In our previous work (Section 2.1.3), SPRs were developed that capture IP and EA across monometallic Au TPNCs solely from the number of metal atoms (n).^[51] We leverage the same descriptor, $n^{-1/3}$, in Figure 4.4 to compare our bimetallic dataset to the previously reported relationships (black dotted lines). As expected, the monometallic Au TPNCs (gold points with black border) tend to follow the linear trend. We note that the SPRs underpredict IP and EA of $Au_{36}(SR)_{24}$, but these values border the 95% confidence interval of the previously developed models in Figure 2.3. Furthermore, all AgAu TPNCs appear to roughly match the trend, indicating that the descriptor is a good metric to capture size effects on IP and EA. Clearly, though, additional information is required to accurately predict these electronic properties across AgAu TPNCs. Although X_{Ag} (color of points in Figure 4.4) appears to differentiate IP and EA behavior for the larger TPNCs, the trend breaks down for the smaller systems. Specifically, we see non-linear behavior (*i.e.*, not $IP|EA \propto X_{Ag}$) arising in the IP of M_{36} (monometallic IPs are almost identical) and EA of M_{102} (Ag_{102} is around the median EA rather than the minimum), which is further illustrated in Figure 4.3. Therefore, X_{Ag} alone cannot capture dopant effects for IP and EA across all TPNC sizes.

Based on our analysis of size and composition effects on IP and EA, there is a clear need to distill further structural information that accounts for the dopant-position-based nuances in electronic properties. As previously described, all TPNCs follow the divide and protect theory,^[33] meaning one can distinguish core from shell atoms based on the experimentally determined structure. This structural rule is important for electronic properties of TPNCs, especially those that are dependent on frontier orbitals of the systems. For example, time-

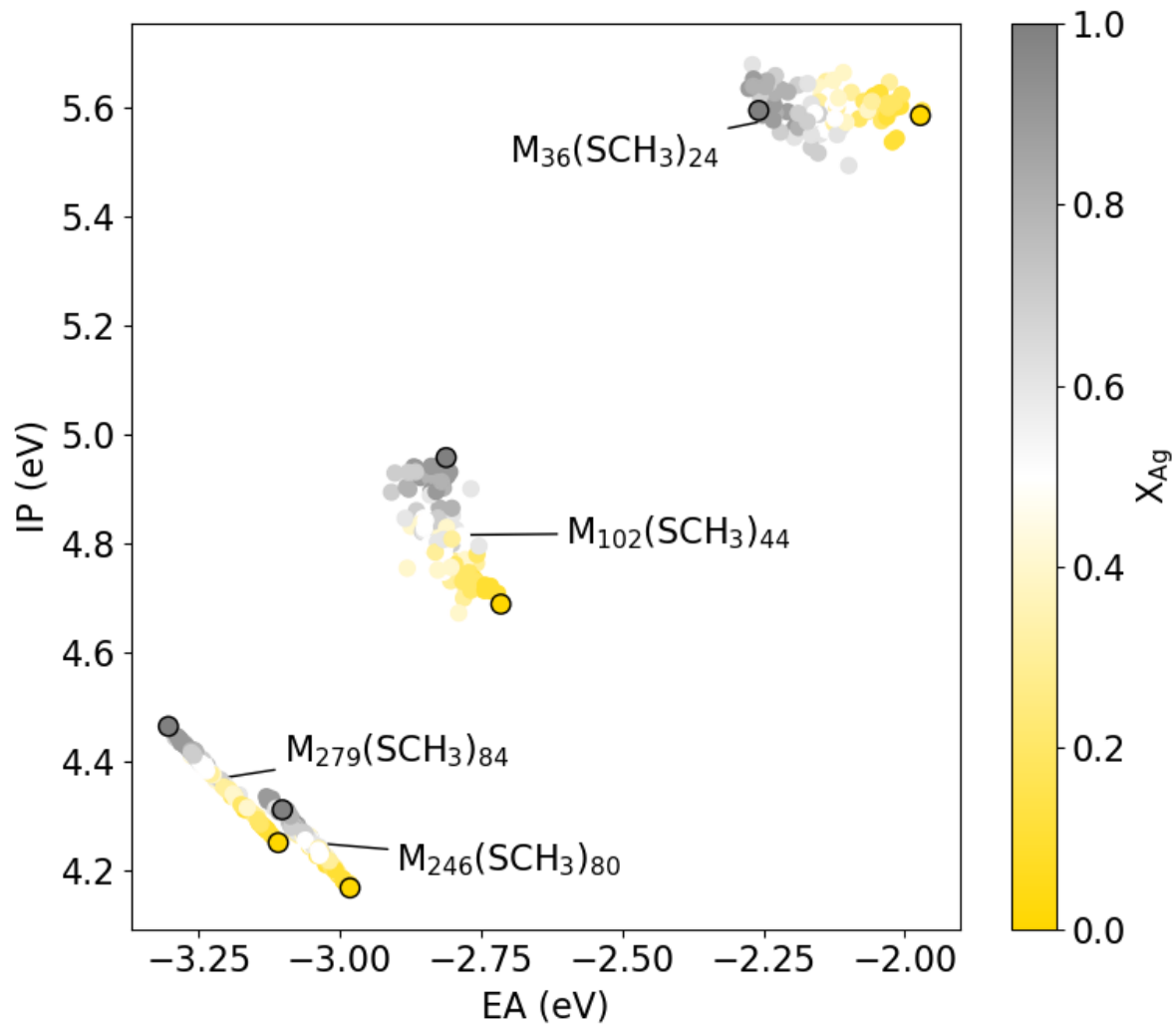


Figure 4.3: Comparing EA and IP of hypothetical AgAu TPNCs. Data color corresponds to composition of Ag (X_{Ag}). Clusters of data labeled by TPNC size. Monometallic data points are highlighted with a black border. M denotes Ag and Au.

dependent DFT (TDDFT) has revealed that low-energy electron excitations (HOMOs to LUMOs) occur by a core-to-shell transition in TPNCs.[24, 115] Since IP and EA directly probe HOMO and LUMO energetics in molecular systems,[113] there is strong physical motivation to distinguish the core and shell regions when attempting to predict these electronic properties. In addition, core and shell metal atoms exhibit different interactions with thiolate ligands. From an electronic standpoint, DFT has shown that shell metal atoms form M(I)-S covalent bonds while core metals instead form dative M(0)-S bonds.[43, 116] Furthermore, by conducting a bond distance analysis of our AgAu TPNC dataset (Figure D.1), we reveal two distinct M-S regimes in each TPNC (green and purple bimodal distributions) that differentiate core and shell M-S bonding. The structural analysis also highlights the similar bond distributions observed across the four TPNCs, including the consistently shorter Au-S bond lengths compared to Ag-S (core Au *vs.* core Ag and shell Au *vs.* shell Ag). Taken together, the different electronic and structural character of M-S interactions indicate the importance of distinguishing core and shell contributions to EA and IP.

By leveraging the core-shell nature of TPNCs, we generated a series of structural descriptors that capture size, composition, and structural makeup of our bimetallic systems. A summary of the descriptors is given in Table D.3. Apart from our global size and composition descriptors ($n^{-1/3}$ and X_{Ag} , respectively), we introduced two new terms that describe metal compositions of the TPNC core and shell. Importantly, we can compute these terms from experimental TPNC structural data (Table D.1, meaning they do not require any DFT calculations. To compare the new descriptors to X_{Ag} and identify their significance to EA and IP, we generated linear regression models (Figure D.2) using just the $M_{36}(SR)_{24}$ TPNC data. We chose to focus on the $M_{36}(SR)_{24}$ due to its unique IP behavior (Figure 4.3). Starting with EA, we find that there is little difference in the predictive ability between X_{Ag} and X_{Ag}^{shell} based on their model coefficients in Figure D.2a, b. The results are expected based on our prior analysis of Ag composition effects (Figure 4.3 and 4.4). In contrast, there is a clear significance of the core-shell properties for IP prediction. While X_{Ag} is unable to differentiate IPs of the different systems, X_{Ag}^{core} and X_{Ag}^{shell} together can capture the IP trend across the $M_{36}(SR)_{24}$ TPNCs. The results agree with our expected physical motivations, where the core and shell of a TPNC influence its IP and EA, respectively.

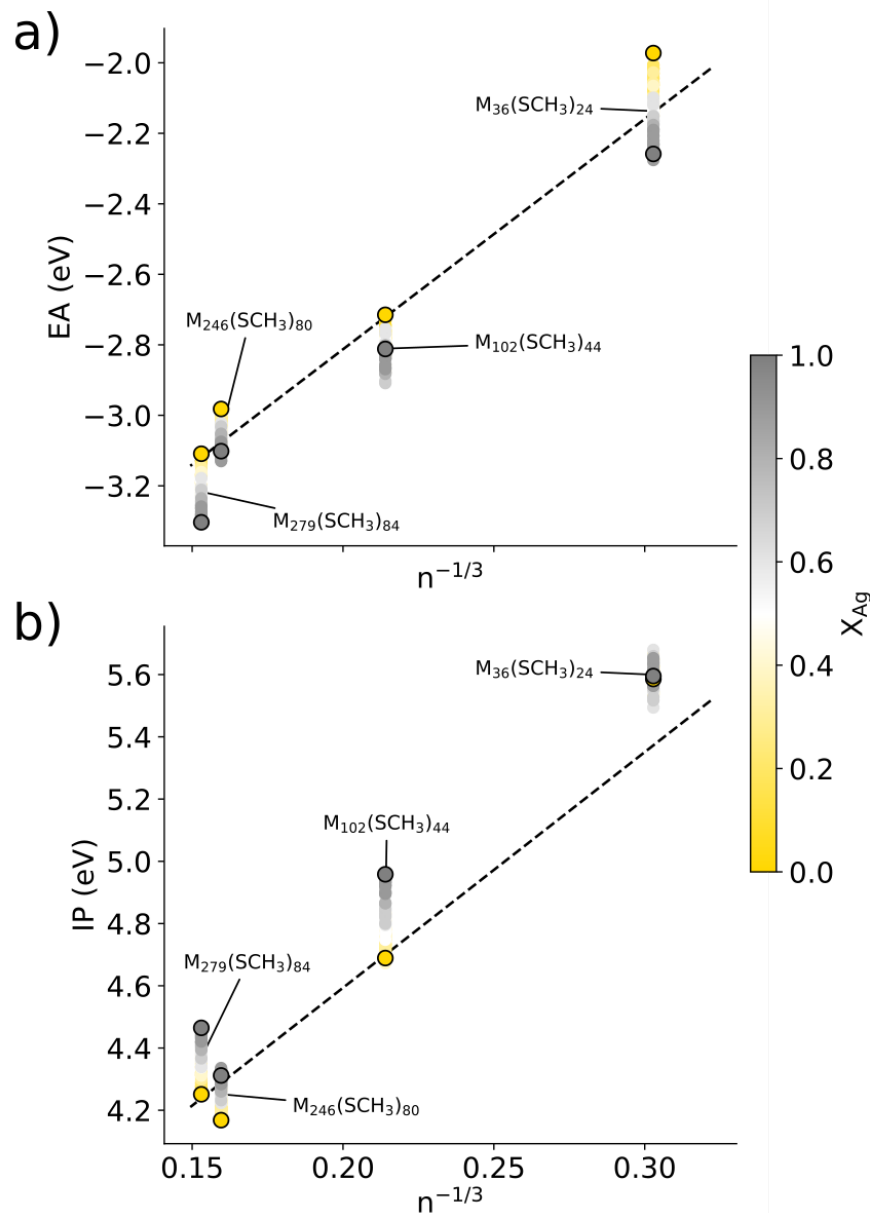


Figure 4.4: Comparing number of metal atoms to the power of $-1/3$ ($n^{-1/3}$) to a) EA and b) IP for our sample of hypothetical AgAu TPNCs. Data color corresponds to composition of Ag (X_{Ag}). Monometallic data points are highlighted with a black border. We note that the monometallic Au_{36} IP point is directly underneath the Ag_{36} point. Clusters of data labeled by TPNC size. Dotted lines represent previously reported EA/IP structure-property relationships for Au TPNCs (see Section 2.1.3).[51]

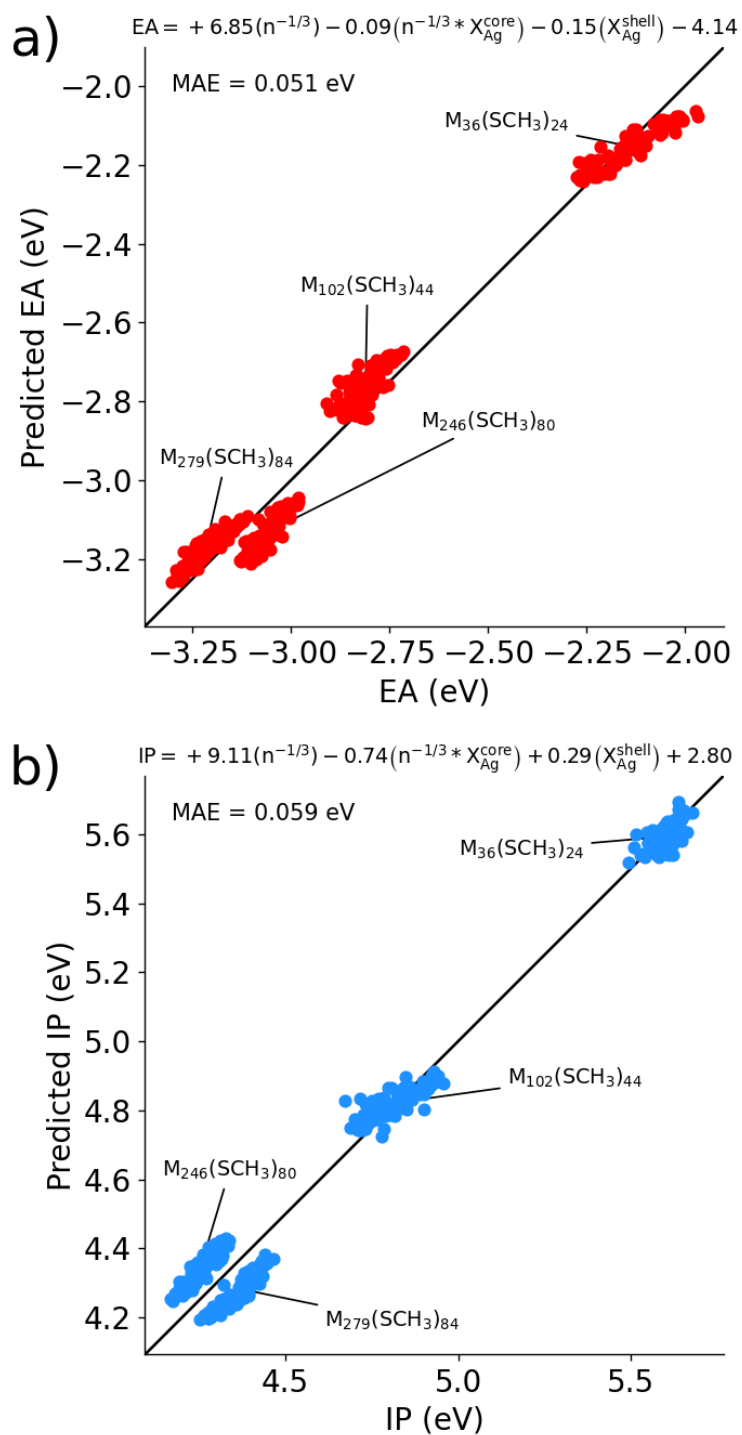


Figure 4.5: Linear regression models (top of plots) that capture a) EA and b) IP of AgAu TPNCs based on simple structural descriptors. Clusters of data labeled by TPNC size. Mean absolute error (MAE) of models are inlaid.

Combining the insights determined from our prior analyses, we employed linear regression to introduce new SPRs that can predict IP and EA across our AgAu TPNC dataset. The models, shown in Figure 4.5, capture these trends with a high degree of accuracy (MAE < 0.06 eV). In addition, they do so by utilizing the same three fundamental descriptors, which capture size ($n^{-1/3}$), composition and core-shell makeup (X_{Ag}^{core} and X_{Ag}^{shell}) of the TPNCs. As expected from the underlying physics, the shell descriptor plays a significant role in predicting EA while the core descriptor does the same for IP, which can potentially relate to the HOMO and LUMO energy levels, respectively. Importantly, we found that our models perform better when the core feature can differentiate size – hence why we use the product of our size and core descriptors as a single feature. The necessary size dependence can be explained by the converging behavior of IP properties observed across the TPNCs in Figure 4.3. By incorporating size, our core term can distinguish large TPNCs from smaller systems where quantum effects and discrete electronic states play a more significant role, therefore achieving stronger correlation across the complete AgAu TPNC dataset. Despite the similar structural properties of the four TPNCs in the dataset, the IP/EA SPRs are expected to work across various Ag-doped Au TPNCs, including different shapes, core packing, and X-mer motif types. This is due to the fact that i) all TPNCs follow divide and protect theory,[33] which was used to develop the new core shell descriptors, and ii) previous IP/EA SPRs for Au TPNCs were shape agnostic.[51] The size regime of AgAu TPNCs probed in this work spans from smaller, molecular-type TPNCs (Au_{36} , Au_{102} and Au_{246}), to the larger metallic-type Au_{279} TPNC. Including Au_{279} in our analysis, which behaves more like an alloy nanoparticle than a typical TPNC (surface plasmon resonance, continuous bands rather than discrete energy levels, etc.), suggests that the trends observed between metal composition and IP/EA could extend to larger Au/Ag nanoparticles (NPs). However, our results do not concretely prove that these systems will have similar IP/EA trends, and therefore additional studies are needed to investigate larger alloy nanomaterials.

When fitting models, it is important to think critically about the dataset. If a dataset is too small, or if it does not correctly represent a domain space, using it to fit a model can lead to misguided conclusions and poor predictive performance in the future. Although it is not possible to perform DFT on the entire bimetallic TPNC configuration space, the

dataset herein was produced in an effort to maximize the area of materials space sampled (*i.e.*, ranging size, composition, and chemical ordering). Furthermore, the simple models have only three degrees of freedom that are physically motivated for the target electronic properties. Though we note that more high quality data is always better as it can lead to higher accuracies, all aforementioned results indicate that the bimetallic TPNC dataset is adequately sized to develop the IP/EA SPRs.

Overall, our new SPRs provide key insights into the physics that dictate TPNC electronic properties. Moreover, they offer powerful screening tools that can aid in experimental design of AgAu TPNCs for targeted applications. Future efforts will focus on predicting highly accurate IP and EA of TPNCs using higher levels of theory that are computationally more expensive. Such data can be used in combination with this high throughput screening approach to accurately relate application-oriented IP/EA behavior (for example, in electrocatalysis and photocatalysis) to the TPNC structure.

4.2 Towards a Universal Stability Model for Alloy TPNCs

The recent efforts to modulate TPNC properties through heterometal doping have yielded remarkable results, including enhanced catalytic activity[117] and realization of new magic sizes.[118] However, with the increase in structural complexity, new challenges arise for structural determination with atomic precision. This problem is magnified at larger TPNC sizes (> 100 metal atoms), which offer a massive configuration space of potential alloy chemical orderings (*i.e.*, how the metals position themselves in a TPNC). Dropping the constraint of a single structure causes an explosion in the size of the potential materials space. Although DFT is an effective approach to study TPNCs, both monometallic and alloy, its computational expense makes exploring large portions of the hypothetical configuration space intractable. Thus, there is a need for accelerated methods capable of determining the most favorable chemical orderings (*i.e.*, maintaining atomic precision) in alloy TPNCs while exploring the vast alloy materials space. Furthermore, the approach should ideally extend across the monometallic space as well, towards a generalized method that captures stability of all TPNCs – opening avenues for accelerated structure prediction. In this work, we lay the foundation towards a computational framework to predict thermodynamically favorable structural configurations of TPNCs, including dopant positions and concentrations in alloy structures.

4.2.1 Computational Details

All DFT calculations, namely geometry optimizations, were performed in CP₂K v6.1 following methodology from prior work.[119] See Section 4.1.1 for complete details.

4.2.1.1 TPNC Formation Energy (E_f)

The TPNC formation energy, E_f , references atomic metals and thiols (HSR) to measure the preference of forming TPNCs and molecular hydrogen. It is a measure of TPNC thermodynamic stability and can importantly differentiate between metal composition, chemical ordering, and ligand type. E_f can be computed with DFT following Equation 4.1, where E_j

is the electronic energy of species j and number of ligands (m) is used as a scaling factor. TPNC formation energy can also be conceptualized as the sum of M-M and M-S bond energies (*i.e.*, the energetic preference of forming M-M and M-S bonds in reference to HSR and atomic metals, M).

$$E_f^{DFT} = \frac{1}{m} \left[\left(E_{M_n(SR)_m} + \frac{1}{2} m E_{H_2} \right) - \left(\sum_i^n E_{M_i} + m E_{HSR} \right) \right] \quad (4.1)$$

4.2.1.2 Bond-Centric Model (BCM)

Cohesive energy (CE) is a metric of thermodynamic stability that describes how stable a metal NP is relative to its atoms infinitely separated apart (*i.e.*, atomic M). Similar to E_f , it can be conceptualized as the sum of M-M bond energies in the NP (scaled by number of atoms, N_{atoms}). The Bond-Centric Model (BCM)[120] calculates the CE of a metal NP with N_{atoms} by summing contributions from all bonds in the system (Equation 4.2). Bond energy contributions between atoms a and b (each term in Equation 4.3) are calculated by their respective coordination number (CN) in the system as well as bulk properties of each metal (periodic crystalline form), including bulk CN and CE (CN_{bulk} and CE_{bulk} , respectively). To account for the difference in bond energies between homoatomic and heteroatomic bond types, the BCM employs a weighting term, γ . A pair of the terms, given as $\gamma_{(a-b)}$ and $\gamma_{(b-a)}$, is calculated for each unique metal-metal combination (*e.g.*, Ag-Au) and is a function of metal dimer bond dissociation energies (BDE, Equations 4.4 and 4.5) as well as a “sum-to-two” constraint (Equation 4.6). Because the BCM leverages easily tabulated values, it provides a rapid means to predict NP stability – surpassing DFT with its faster computation time as well as larger range of measurable NP sizes. Further, since the model measures each explicit bond energy, it can differentiate metal composition and chemical ordering.[48]

$$CE_{NP} = \frac{1}{N_{atoms}} \sum_k^{N_{bonds}} (BondEnergy_{(a-b)})_k \quad (4.2)$$

$$BondEnergy_{(a-b)} = \frac{\gamma_{(a-b)} CE_{bulk,a}}{\sqrt{CN_a CN_{bulk,a}}} + \frac{\gamma_{(b-a)} CE_{bulk,b}}{\sqrt{CN_b CN_{bulk,b}}} \quad (4.3)$$

$$BDE_{(a-b)} = E_a + E_b - E_{(a-b)} \quad (4.4)$$

$$BDE_{(a-a)}\gamma_{(a-b)} + BDE_{(b-b)}\gamma_{(b-a)} = 2 \times BDE_{(a-b)} \quad (4.5)$$

$$\gamma_{(a-b)} + \gamma_{(b-a)} = 2 \quad (4.6)$$

4.2.2 Curating a TPNC Dataset

The study herein includes a variety of TPNC structures from prior works, including the SCH₃-protected TPNCs from Section 2.1 as well as the AgAu dataset from Section 4.1.2 to probe alloy effects. Additional experimentally determined TPNCs protected by PET and TBBT ligands were also included to probe ligand effects across different sizes. These structures were taken from literature.[25–27, 54–56, 91, 121, 122] A summary of the complete TPNC dataset (392 unique structures) is given in Table 4.1.

Table 4.1: Summary of TPNCs included in this study grouped by experimental ligand type or hypothetical ligand/doping (denoted with *).

TPNC Group	# Structures	Reference(s)
*SCH ₃ -protected Au	15	Section 2.1
*SCH ₃ -protected AgAu (alloy)	368	Section 4.1.2
PET-protected Au	4	[25, 26, 55, 121]
TBBT-protected Au	5	[27, 54, 56, 91, 122]

We first calculate E_f^{DFT} for the range of TPNCs. The results are given in Figure 4.6 as a plot of E_f^{DFT} vs. number of metal atoms (n). The graph reveals that E_f^{DFT} generally decreases (becomes more exothermic) as a function of TPNC size (represented by n), which is comparable to CE trends in metal NPs. This general trend is expected since E_f^{DFT} measures bond energies in the structure and upon an increase in size, the number of bonds increases

at a consistently higher rate than n (*i.e.*, each metal atom is always forming more than one bond). When looking at just alloy structures (light blue points), one can see that E_f^{DFT} is able to differentiate various alloy TPNCs of the same metal-ligand composition, which shows the potential for E_f^{DFT} as a reasonable metric to compare stability between TPNC alloys.

4.2.3 Extending the BCM to TPNCs (E_f Model)

As previously mentioned, the BCM[120] provides an accelerated means to predict metal NP stability. The model does so by computing CE, which measures the M-M bond energies of a given metal NP. Similarly, E_f measures bond energies in a TPNC, including M-M as well as M-S bonds, to probe stability. Thus, if the BCM can be extended to also capture M-S bond energies, it should in theory be able to predict E_f for TPNCs.

In order to extend the BCM to capture M-S bonds, or more specifically the M-SR bond, one can adjust the reference utilized in the model. For the case of metals, the BCM references the bulk crystalline form (*e.g.*, Au in its FCC unit cell). Since thiolates are derived from thiols during TPNC synthesis,[19] it is reasonable to treat a thiol as the reference state for SR units, which importantly matches the reference of E_f (Equation 4.1). With a selected reference, we can now map the BCM parameters to their S-equivalent analogues. CN_{bulk}^S is set to 2 (Equation 4.7) due to the two S bonds present in thiols (H-S-R). Since metal CE_{bulk} is the average bond strength per single atom, it can be thought of – conceptually – as the bond strength that a metal forms in its reference state. Therefore, the same measure can be achieved for S by calculating the H-SR bond formation energy (BFE), as shown in Equation 4.8. Of note, BFE utilizes H_2 as a hydrogen feedstock, which is a similar concept to the E_f formulation, just in an opposite manner. To determine metal-ligand γ values, we can leverage BDEs of metal-thiolate complexes as well as thiols (*i.e.*, analogues to “heteroatomic” and “homoatomic” metal dimers, respectively). BDEs are computed via Equation 4.4, treating $M + SR$ and $H + SR$ as a and b units for metal-thiolate complexes and thiols, respectively. Combining Equations 4.5 and 4.6, we can compute γ values for any metal ligand pair. Taken together, the new parameterizations can be used with the BCM to predict M-S bond energies, extending the model to TPNCs. Moreover, since the parameters only depend on simple

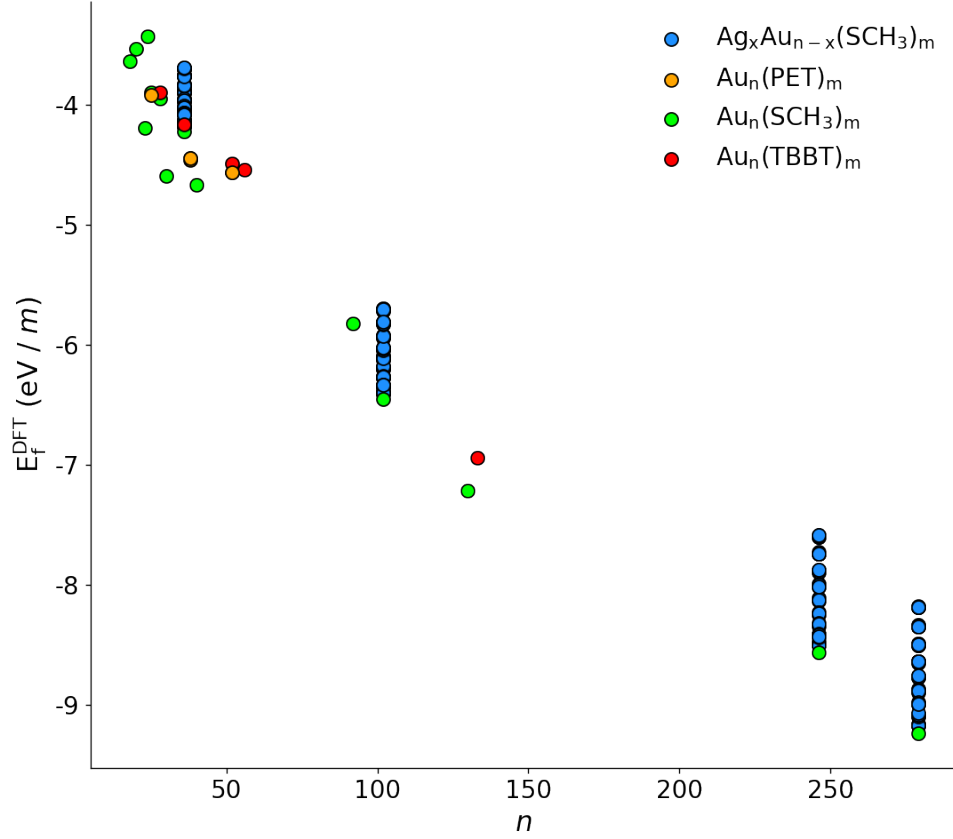


Figure 4.6: DFT-calculated TPNC formation energy (E_f^{DFT}) *vs.* number of metal atoms (m). Data color separates by AgAu TPNCs (blue), PET-protected Au TPNCs: orange, SCH_3 -protected Au TPNCs: green, TBBT-protected Au TPNCs: red.

calculations of small molecules, the extended model maintains its computational efficiency. A summary of all values used to parameterize the BCM for TPNCs are provided in Table D.4.

$$CN_{bulk}^S = 2 \quad (4.7)$$

$$CE_{bulk}^S = BFE_{HSR} = E_{HSR} - E_{SR} - 0.5E_{H_2} \quad (4.8)$$

With all required parameters tabulated, we next utilize the extended BCM, aptly named the E_f model, to calculate formation energies for our complete dataset of TPNCs (Table 4.1). The results are reported in Figure 4.7 as a parity plot between E_f calculated by the model and DFT. The plot reveals the excellent performance by the model across the TPNC groups, with all mean absolute percent errors (MAPEs) $\leq 8.10\%$ (Equation 4.9). It is crucial to note that there is no model fitting. The results are instead based on parameters from the previously determined properties of small molecules (*i.e.*, metal dimers, metal-ligand complexes, and thiols). Furthermore, since the E_f model parameters reference specific thiol molecules, this single model can easily compute the stability of TPNCs protected by each of the three ligands. Importantly, the E_f model also appears to capture the correct trends between the hypothetical AgAu TPNCs. Indeed, the model is able to differentiate between metal compositions. However, it is difficult to determine model performance based on chemical ordering due to the small differences in E_f between AgAu TPNCs that only differ in atomic arrangement (*i.e.*, same size and composition). These results are not surprising, though, considering experimental observations that Ag can be doped into Au TPNCs across a large range of compositions.[47, 108–110] Nevertheless, the overall results reveal the potential of the E_f model as a universal method to predict stability for any TPNC structure.

$$MAPE = \sum_i \left(\frac{|model - actual|}{actual} \times 100\% \right) \quad (4.9)$$

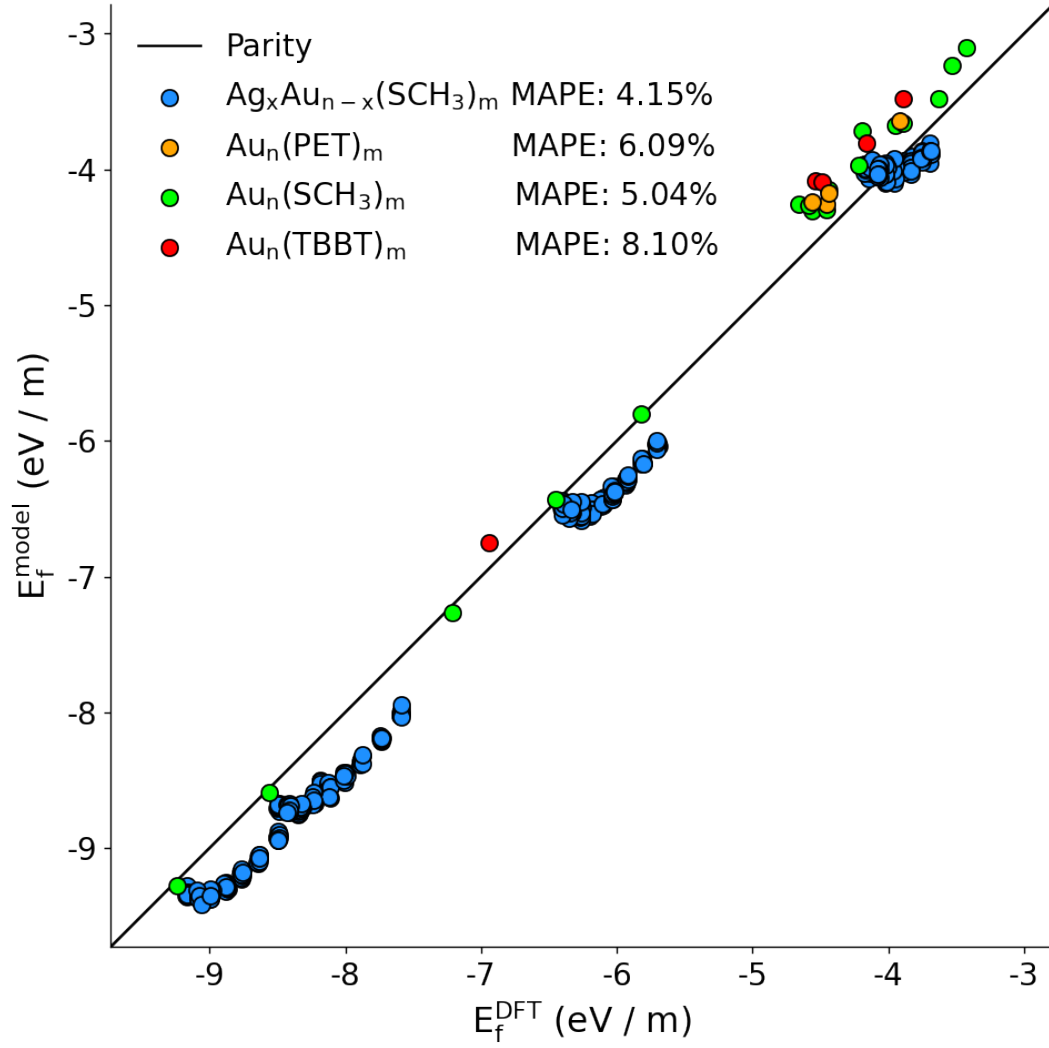


Figure 4.7: Parity plot comparing extended BCM model performance to DFT based on TPNC formation energy (E_f).

4.2.4 Applying the E_f Model to $\text{Au}_{38}(\text{PET})_{24}$ Isomers

When comparing between chemical orderings of a given TPNC structure (same size, shape, and composition), the type and number of atoms remains constant. Thus, comparing E_f values is identical to comparing the electronic energy of each TPNC (based on Equation 4.1). One can then make direct comparisons of stability through E_f values, which is the key component behind the potential of the E_f model for predicting favorable dopant positions in TPNCs. Zooming out to a more general view, the E_f model offers a route to compare stability between *any* TPNC structural isomers regardless of metal composition. Therefore, successfully predicting E_f can aid in generalized structure prediction of new TPNCs.

The TPNC dataset in this work includes two $\text{Au}_{38}(\text{PET})_{24}$ isomers (Figure 4.9), denoted Q[26] and T[55] (based on the names of the first authors who experimentally determined their structures[55]). Each structure consists of a 23-atom core, but with different configurations (bottom row of Figure 4.9). They also exhibit unique protecting shells with various motif types (middle row). The Q is made of three monomers and six dimers while the T consists of three monomers, three dimers, two trimers, and a single bridging thiolate. Comparing the unique core-shell components of the nanoclusters highlights the stark structural difference possible between TPNC isomers. Beyond experimental synthesis and structural determination, the relative stability of the isomers has also been tested experimentally. Tian *et. al.* revealed that, upon elevated temperatures (50°C), the T will spontaneously transform to the Q TPNC.[55] However, the reversible transformation was not possible, indicating that the Q is more thermodynamically stable. Due to these experimental observations, the $\text{Au}_{38}(\text{PET})_{24}$ isomers make up a perfect case to test the E_f model for its ability to measure relative stability between isomers.

Figure 4.8 depicts the E_f of the $\text{Au}_{38}(\text{PET})_{24}$ isomers calculated with DFT (blue bars) and with the model (green bars). Beginning with the former, we find that E_f^{DFT} accurately predicts the Q to be more thermodynamically stable than the T. Despite the systematic error (in reference to DFT), the model is still capturing the correct trend. Indeed, the E_f model is clearly predicting the Q as the more thermodynamically stable TPNC isomer. We also calculated E_f of the isomers protected by SCH_3 (Figure D.3). The additional results show that both DFT and the model correctly predict the SCH_3 -protected Q isomer to be more stable. This result not only provides further support of the E_f model’s accuracy, but it also provides further evidence that SCH_3 is a reasonable substitution for PET when computing electronic property calculations. Overall, the E_f model results are in excellent agreement with both theory and experimental observation, supporting its use as a general guide for TPNC structure prediction.

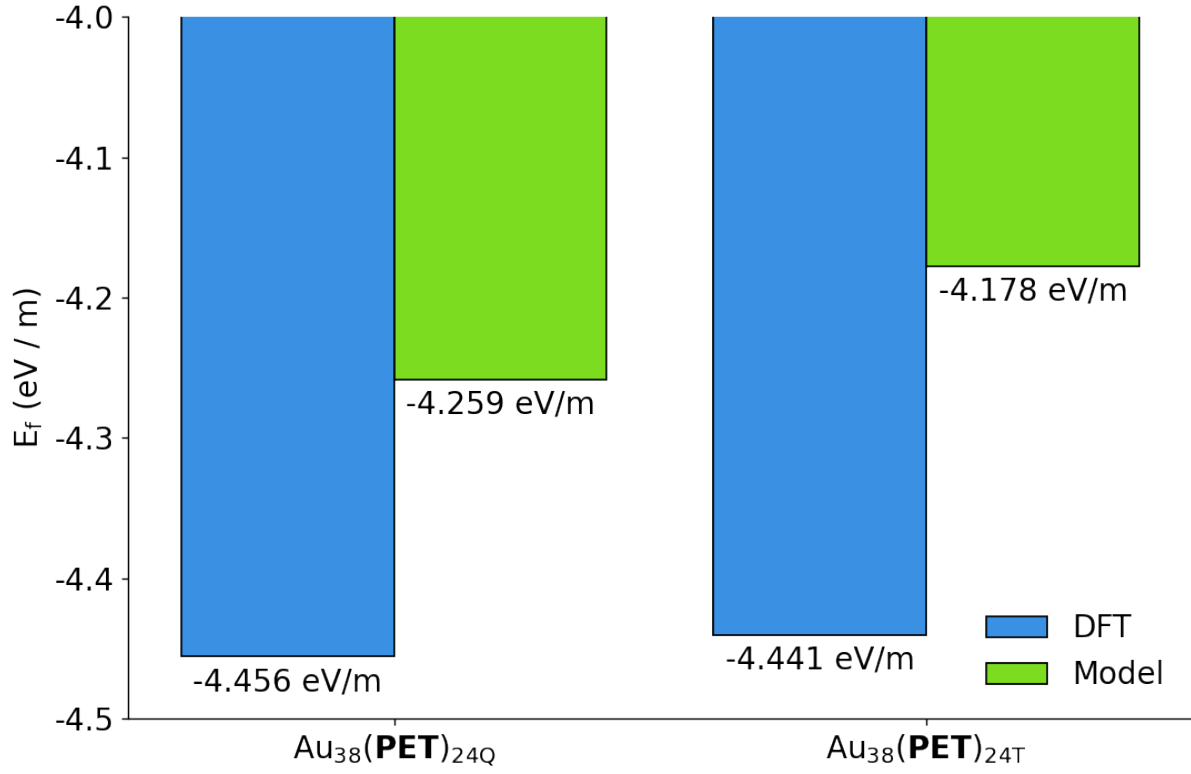


Figure 4.8: TPNC formation energy (E_f in eV/ m , where m is the number of ligands) of two experimentally determined $\text{Au}_{38}(\text{PET})_{24}$ isomers: Q (left) and T (right). Blue bars = E_f^{DFT} , Green bars = E_f^{model} .

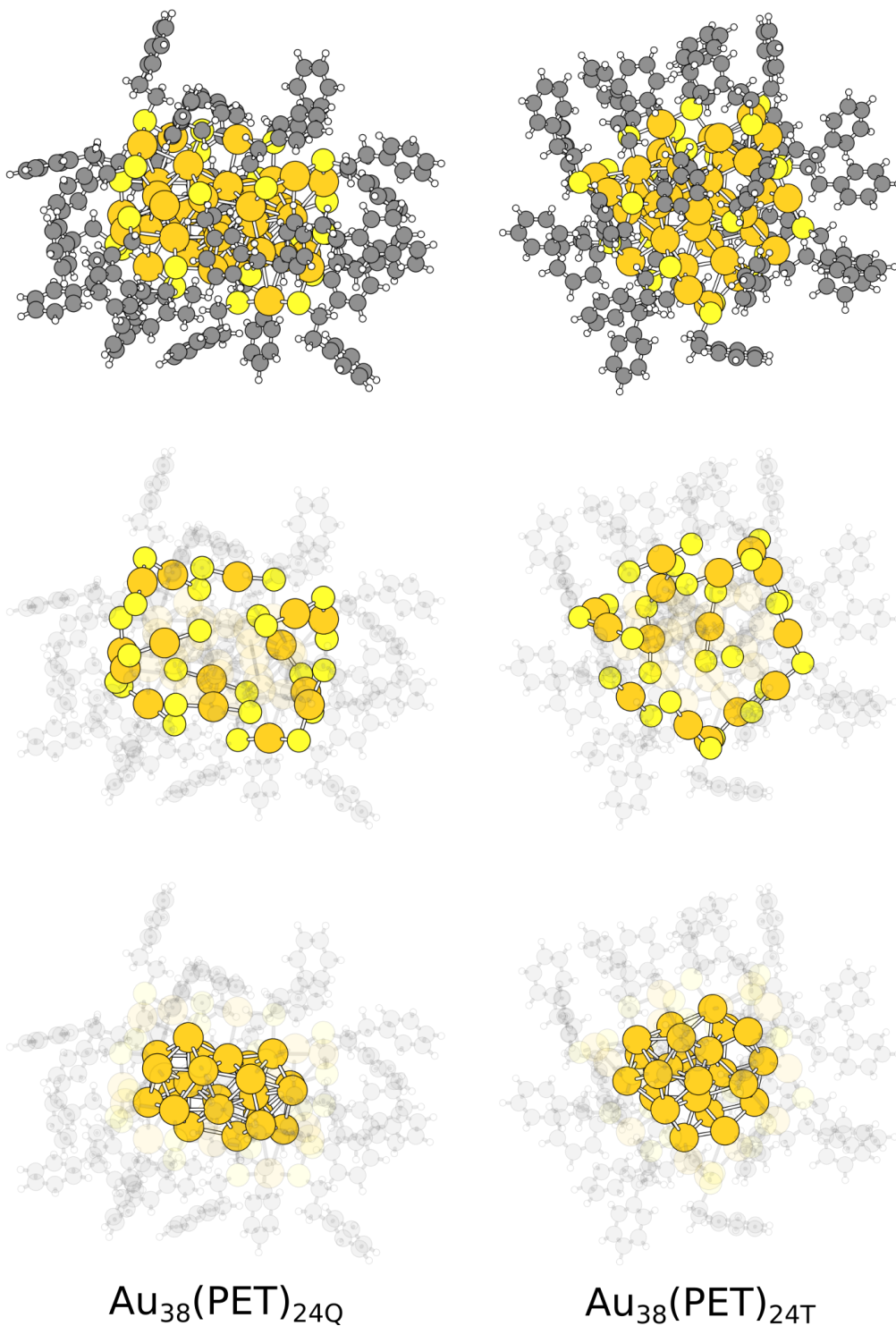


Figure 4.9: TPNC structures (top row) of two experimentally determined $\text{Au}_{38}(\text{PET})_{24}$ isomers: Q (left) and T (right). MS motifs (middle row) and cores (bottom row) of each TPNC are shown to illustrate the structural differences between isomers.

4.3 Conclusions

In summary, we explored structural effects on electronic properties of AgAu TPNCs to unravel new SPRs based on simple, atom counting descriptors. We first generated a dataset of 368 hypothetical AgAu TPNCs ranging in size ($M_{36}(\text{SR})_{24}$, $M_{102}(\text{SR})_{44}$, $M_{246}(\text{SR})_{80}$, and $M_{279}(\text{SR})_{84}$) composition ($\approx 10\%$ Ag increments) and chemical ordering. Using DFT, we optimized the structures of each TPNC and subsequently calculated their IP and EA. These electronic properties were then visualized to reveal unique, size-dependent behavior across our sample space. The diverging behavior, especially for IP, was rationalized by the emergence of quantum effects and discrete electronic energy levels for smaller TPNCs. Next, we compared our dataset to IP/EA SPRs previously developed on Au TPNCs, showing general agreement with the models. In order to extend these SPRs to capture alloy effects, we introduced new composition-based features that account for the core-shell nature of TPNCs. After revealing the significance of our new features for IP prediction in $M_{36}(\text{SR})_{24}$, we employed linear regression to produce new SPRs that can accurately predict IP and EA of AgAu TPNCs. The IP/EA models each utilize the same three descriptors that do not rely on DFT calculations. Importantly, we connect the role of each descriptor in predicting IP and EA to the underlying physics that govern the TPNC electronic behavior. Overall, the developed SPRs provide physical insights on TPNC electronic properties and open avenues towards application-targeted design of AgAu TPNCs with finely tuned IP and EA behavior.

Seeking to maintain atomic precision, we developed the E_f model, which captures the thermodynamic stability of TPNCs. The model is an extension of the BCM and was able to predict E_f across a range of TPNCs with $\text{MAPE} \leq 8.10\%$. Importantly, the model involves no fitting, and instead relies on simple calculations on metal dimers, metal-ligand complexes, and thiol molecules. Apart from predicting E_f across TPNCs protected by various ligand types, the model can also capture trends of hypothetical alloy (AgAu) TPNCs. Furthermore, the model correctly predicts stability preference between a pair of experimentally determined $\text{Au}_{38}(\text{PET})_{24}$ isomers, revealing its potential as a tool for TPNC structure prediction. Overall, our results lay the foundation for further development of the E_f model towards a universal method to capture TPNC stability.

5.0 Future Work

5.1 Capture Role of Ligand Effects on TPNC IP and EA

The work herein introduced IP/EA SPRs for monometallic TPNCs (Section 2.1.3).[51] Since the models were able to rationalize stability of a M_{21} - M_{24} TPNC series that includes a heterometal-doped structure,[69] the natural next step was to extend these SPRs to alloy systems. This process was completed for AgAu TPNCs in Section 4.1.[119] Of note, all development of the SPRs was done using TPNCs with SCH_3 -substituted ligands (rather than the experimental “full” ligands). Importantly, prior work in literature revealed that certain ligands can affect IP and EA of TPNCs[65, 66] as well as TPNC optical properties.[115] Therefore, in order to achieve a complete understanding of IP/EA trends across TPNCs, it is imperative to investigate ligand effects on these electronic properties. Next steps should focus on identifying and studying TPNC series protected by the same ligand type (*e.g.*, TBBT series[73]) to systematically unravel the role of ligands on IP and EA. The future work should also invoke analyses across a range of structures (similar to the approaches herein) and previously developed SPRs to aid in discovering general relationships that capture TPNC IP and EA across any size, ligand type, and metal composition. Doing so will provide on-demand prediction of TPNC electronic properties to fuel application-targeted structure design.

5.2 Improved E_f Model that Distinguishes TPNC Core and Shell

Despite the promising performance of the E_f model across monometallic and AgAu TPNCs (Section 4.2), there is still significant room for improvement. The current methodology behind the model differentiates M-M and M-S bonds based solely on metal type and coordination. However, divide and protect theory[33] clearly explains that there are two distinct regions within a TPNC: a core and shell. Other works from literature have revealed that core and shell metals have different oxidation states, specifically M(0) and M(I), respectively, giving different electronic properties.[43] This difference leads to different bonding nature between sulfurs and core metals *vs.* shell metals, which can be illustrated through a bond distance analysis (green and purple bimodal distributions in Figure D.1). Since we can easily determine the core and shell regions from experimental structures (illustrated by the work in Section 4.1), distinguishing bond types based on core-shell properties will not harm the computational efficiency of the model. Instead, it should significantly aid in the overall performance of the E_f model since there is a clear difference in core *vs.* shell bond properties. Thus, by further modifying the E_f model to differentiate bonding in core-shell regions of TPNCs, we can inject richer information into the model to boost its ability to predict E_f across all TPNCs. Future efforts should strive to incorporate core-shell information into the E_f model by developing new reference states that differentiate core and shell metal electronic structures. Upon success, the approach should enhance the accuracy of the stability model, which is necessary to unlock its use as a tool for dopant position/concentration elucidation and structure prediction of colloidal systems.

6.0 Summary of Publications from PhD

1. M. J. Cowan and G. Mpourmpakis. Structure-property relationships on thiolate-protected gold nanoclusters. *Nanoscale Advances*, 1:184–188, 2019.
2. M. J. Cowan, T. Higaki, R. Jin, and G. Mpourmpakis. Understanding the solubility behavior of atomically precise gold nanoclusters. *The Journal of Physical Chemistry C*, 123:20006–20012, 2019.
3. Y. Li*, M. J. Cowan*, M. Zhou, M. G. Taylor, H. Wang, Y. Song, G. Mpourmpakis, and R. Jin. Heterometal-doped M_{23} ($M = \text{Au/Ag/Cd}$) nanoclusters with large dipole moments. *ACS Nano*, 14:6599–6606, 2020.
4. Y. Li*, M. J. Cowan*, M. Zhou, Y. Song, T. Y. Luo, H. Wang, N. L. Rosi, G. Mpourmpakis, and R. Jin. Atom-by-atom evolution in the adamantanethiolate-protected $\text{Au}_{21} - \text{Au}_{22} - \text{Au}_{22}\text{Cd}_1 - \text{Au}_{24}$ nanocluster series. *Journal of the American Chemical Society*, 142(48):20426–20433, 2020.
5. M. J. Cowan*, A. V. Nagarajan*, and G. Mpourmpakis. Correlating structural rules with electronic properties of ligand-protected alloy nanoclusters. *Journal of Chemical Physics*, 155:024303, 2021.
6. A. V. Nagarajan, R. Juarez-Mosqueda, M. J. Cowan, R. Jin, D. R. Kauffman, and G. Mpourmpakis. Elucidating the stability of ligand-protected Au nanoclusters under electrochemical reduction of CO_2 . *SN Applied Sciences*, 2:680, 2020.
7. J. Dean*, M. J. Cowan*, J. Estes, M. Ramadan, and G. Mpourmpakis. Rapid prediction of bimetallic mixing behavior at the nanoscale. *ACS Nano*, 14:8171–8180, 2020.
8. M. J. Cowan and G. Mpourmpakis. Towards elucidating structure of ligand-protected nanoclusters. *Dalton Transactions*, 49:9191–9202, 2020.
9. J. McKay, M. J. Cowan, and G. Mpourmpakis. Predicting ligand removal energetics in thiolate-protected nanoclusters from molecular complexes. *Nanoscale*, 13:2034–2043, 2021.

*Authors contributed equally.

10. A. V. Nagarajan, D. J. Loevlie, M. J. Cowan, and G. Mpourmpakis. Electrocatalytic imprecision in atomically precise metal nanoclusters. *Current Opinion in Chemical Engineering*, 2021, *Accepted*.
11. M. Salem, M. J. Cowan, and G. Mpourmpakis. Predicting segregation energy in single atom alloys using physics and machine learning. *ACS Omega*, 2021, *Under Review*.
12. M. J. Cowan and G. Mpourmpakis. Towards a universal stability model for thiolate-protected alloy nanoclusters. *Under Preparation*.

Works 1–5, 12 are highlighted in this dissertation.

Appendix A Abbreviations and Nomenclature

BCC	body-centered cubic
BCM	Bond-Centric Model
BDE	bond dissociation energy
BE	binding energy
BFE	bond formation energy
CE	cohesive energy
CN	coordination number
DCM	dichloromethane
DFT	Density Functional Theory
DZVP	double- ζ valence polarized
EA	electron affinity
FCC	face-centered cubic
GTH	Goedecker-Tetter-Hutter
HCP	hexagonal close packed
HOMO	highest occupied molecular orbital
HSP	Hansen solubility parameter
IP	ionization potential
LUMO	lowest unoccupied molecular orbital
MAPE	mean absolute percent error
NBO	natural bond orbital
NP	nanoparticle
p-MBA	<i>para</i> -mercaptobenzoic acid
PBE	Perdew-Burke-Ernzerhof
PET	phenylethanethiolate
SAdm	1-adamantanethiolate
SCF	self-consistent field
SPR	structure-property relationship
TBBT	4- <i>tert</i> -butylbenzenethiolate

TOA⁺	tetraoctylammonium
TPNC	thiolate-protected metal nanocluster
TSM	Thermodynamic Stability Model

α	molecular polarizability
$\Delta\alpha$	anisotropy in polarizability
μ	magnitude of dipole moment vector
m	number of ligands
n	number of metal atoms
q	charge state of TPNC

Appendix B Rationalizing TPNC Stability Through SPRs

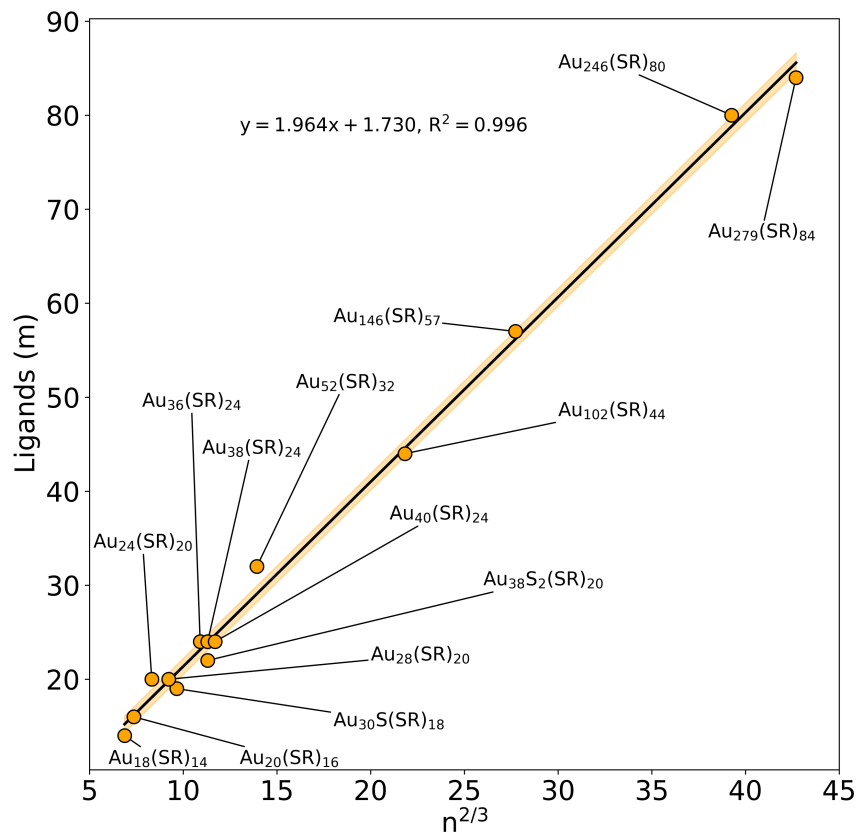


Figure B.1: Metal-ligand relationship of experimentally determined TPNCs (labeled $\text{Au}_n(\text{SR})_m$). Number of ligands (m) linearly correlates with $n^2/3$ (depicted by the solid black line) with an R^2 of 0.995. The shaded orange region represents the 95% confidence interval of the linear regression fit.

Appendix C Unraveling Distinct TPNC Properties Through Dipole Moments

Table C.1: Dipole moment calculations. μ_i corresponds to the i th (x, y, z) component of the dipole vector. μ is the magnitude of each vector. All values are in units of Debye.

Name	μ_x	μ_y	μ_z	μ
Au ₂₁ (SAdm) ₁₅	2.8561	0.1961	1.5321	3.25
Au ₂₅ (PET) ₁₈	0.0389	0.0004	0.0154	0.04
[Au ₂₅ (PET) ₁₈] [−]	0.0025	0.0215	0.0246	0.03
[Au ₂₅ (PET) ₁₈] [−] [TOA] ⁺	22.8743	1.2534	0.2104	22.91
Au ₂₈ (TBBT) ₂₀	0.0991	2.3169	2.0022	3.06
Au ₃₀ (SAdm) ₁₈	0.0003	0.0002	0.0000	0.00
Au ₃₀ S(S-tBut) ₁₈	2.8926	0.2697	1.9444	3.50
Au ₃₆ (TBBT) ₂₄	1.4552	0.6026	0.7653	1.75
Au ₃₈ S ₂ (SAdm) ₂₀	2.4365	0.1577	3.5460	4.31
Au ₄₀ (o-MBT) ₂₄	1.4197	0.6611	0.0967	1.57
Au ₅₂ (TBBT) ₃₂	0.1876	1.4081	1.8054	2.30
Au ₁₃₃ (TBBT) ₅₂	3.2016	1.8117	0.7847	3.76

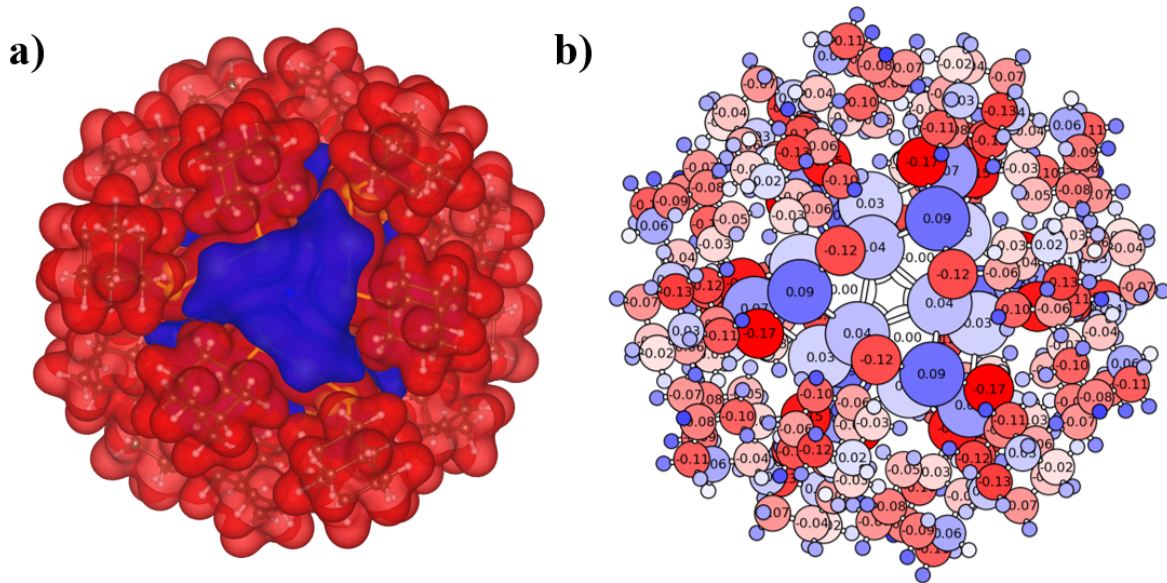


Figure C.1: Charge density maps of $\text{Au}_{30}(\text{SAdm})_{18}$. a) Electrostatic potential map and b) atomic point charges calculated with Bader charge analysis. Blue and red colors correspond to positive and negative charge, respectively.

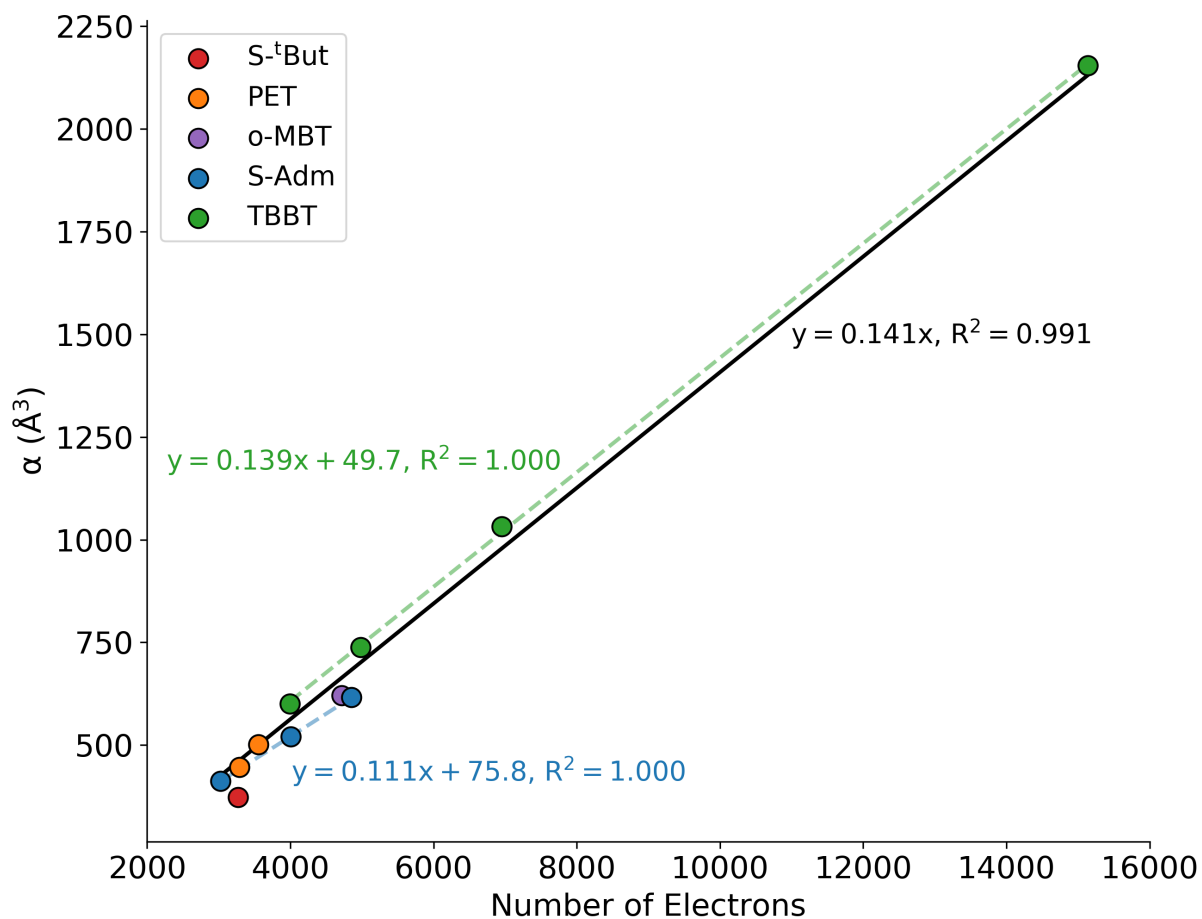


Figure C.2: Average polarizability compared to number of electrons in each TPNC. Different colors correspond to different ligand type. A linear regression was calculated for all data (solid black line) as well as TPNCs protected by TBBT (dotted green line) and SAdm (dotted blue line).

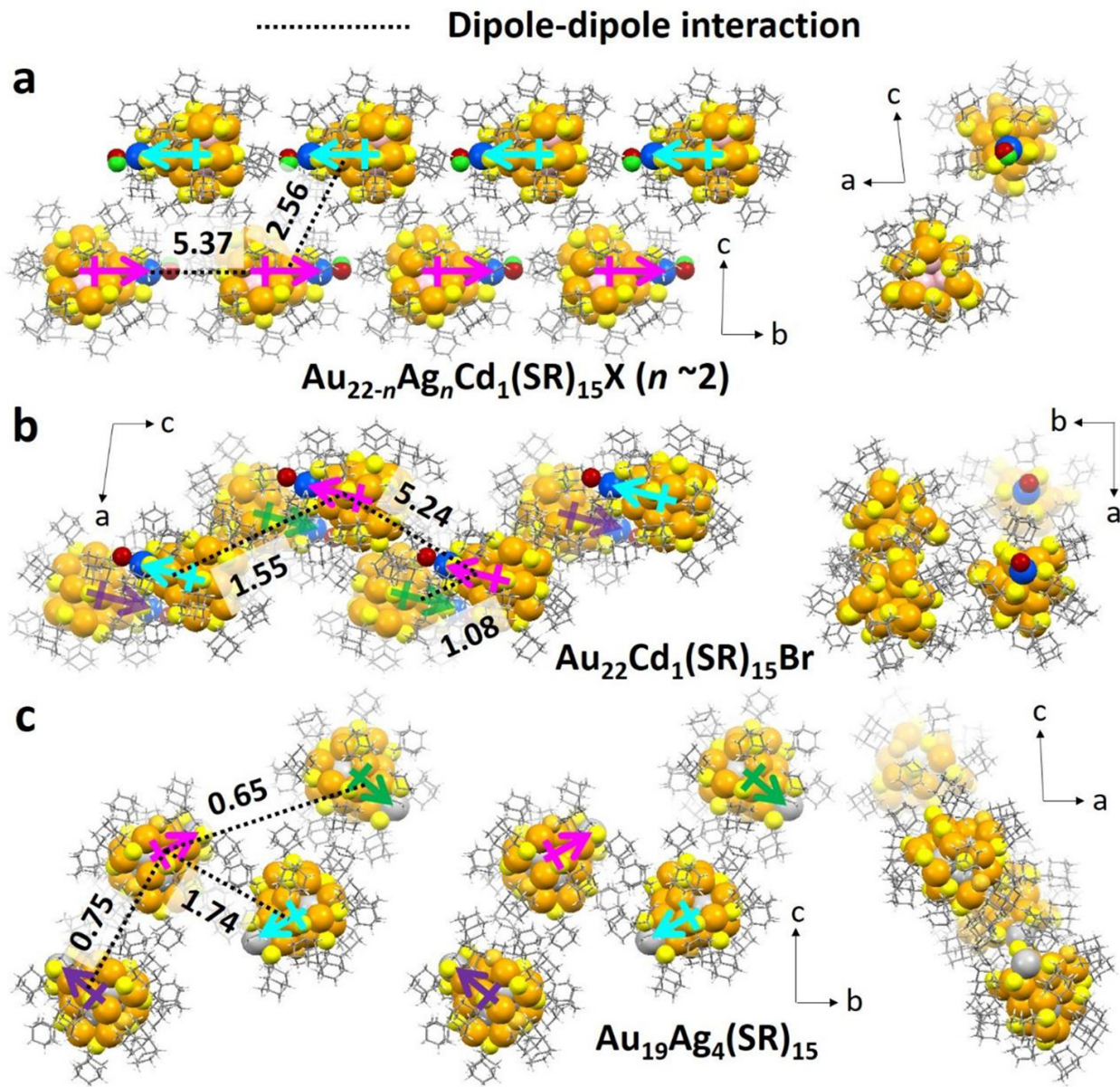


Figure C.3: TPNC dipole alignment in the crystal states of (a) $\text{Au}_{22-n}\text{Ag}_n\text{Cd}_1(\text{SAdm})_{15}\text{Br}$ ($n = 1-4$), (b) $\text{Au}_{22}\text{Cd}_1(\text{SAdm})_{15}\text{Br}$, and (c) $\text{Au}_{19}\text{Ag}_4(\text{SAdm})_{15}$. All TPNCs are marked with their dipole vectors, and the energy of attraction interactions between two NC dipoles are indicated in the unit of kJ/mol. Color labels: yellow = Au, light gray = Ag, pink = Au/Ag, blue = Cd, maroon = Br, green = Cl, light yellow = S, and gray = C.

Appendix D Decoding Chemical Ordering in Alloy TPNCs

Table D.1: Exact compositions generated for the bimetallic TPNC dataset from Chapter 4.

Approximate X_{Ag}	Composition			
	$M_{36}(SR)_{24}$	$M_{102}(SR)_{44}$	$M_{246}(SR)_{80}$	$M_{279}(SR)_{84}$
10%	Ag_4Au_{32}	$Ag_{10}Au_{92}$	$Ag_{25}Au_{221}$	$Ag_{28}Au_{251}$
20%	Ag_7Au_{29}	$Ag_{20}Au_{82}$	$Ag_{49}Au_{197}$	$Ag_{56}Au_{223}$
30%	$Ag_{11}Au_{25}$	$Ag_{31}Au_{71}$	$Ag_{74}Au_{172}$	$Ag_{84}Au_{195}$
40%	$Ag_{14}Au_{22}$	$Ag_{41}Au_{61}$	$Ag_{98}Au_{148}$	$Ag_{112}Au_{167}$
50%	$Ag_{18}Au_{18}$	$Ag_{51}Au_{51}$	$Ag_{123}Au_{123}$	$Ag_{140}Au_{139}$
60%	$Ag_{22}Au_{14}$	$Ag_{61}Au_{41}$	$Ag_{148}Au_{98}$	$Ag_{167}Au_{112}$
70%	$Ag_{25}Au_{11}$	$Ag_{71}Au_{31}$	$Ag_{172}Au_{74}$	$Ag_{195}Au_{84}$
80%	$Ag_{29}Au_7$	$Ag_{82}Au_{20}$	$Ag_{197}Au_{49}$	$Ag_{223}Au_{56}$
90%	$Ag_{32}Au_4$	$Ag_{92}Au_{10}$	$Ag_{221}Au_{25}$	$Ag_{251}Au_{28}$

Table D.2: Core-shell details of the four Au TPNC used to generate the AgAu TPNC dataset generated in Chapter 4.

Composition	Core Atoms	Bridging SR	Monomers	Dimers
$M_{36}(\text{SR})_{24}$	20	0	0	8
$M_{102}(\text{SR})_{44}$	79	0	19	2
$M_{246}(\text{SR})_{80}$	206	10	20	10
$M_{279}(\text{SR})_{84}$	243	18	24	6

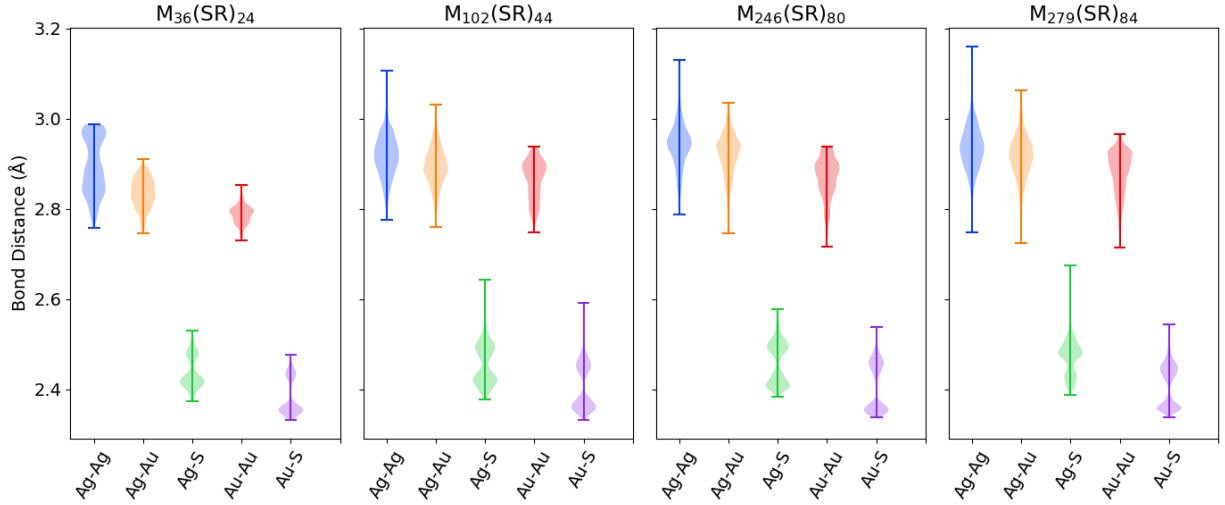


Figure D.1: Bond analysis of the optimized AgAu TPNC dataset from Chapter 4. Violin plots show the distribution of bond distances between different element pairs, including the range (capped lines) and relative frequency of bond lengths (shaded regions).

Table D.3: List of structural properties explored for EA/IP SPRs for AgAu TPNCs.

Property	Formula	Description
$\mathbf{n}^{-1/3}$	-	Metal atom count raised to the power of -1/3
\mathbf{X}_{Ag}	N_{Ag}/N_M	Ag composition
\mathbf{X}_{Ag}^{core}	N_{Ag}^{core}/N_{core}	Ag composition of core
\mathbf{X}_{Ag}^{shell}	$N_{Ag}^{shell}/N_M^{shell}$	Ag composition of shell

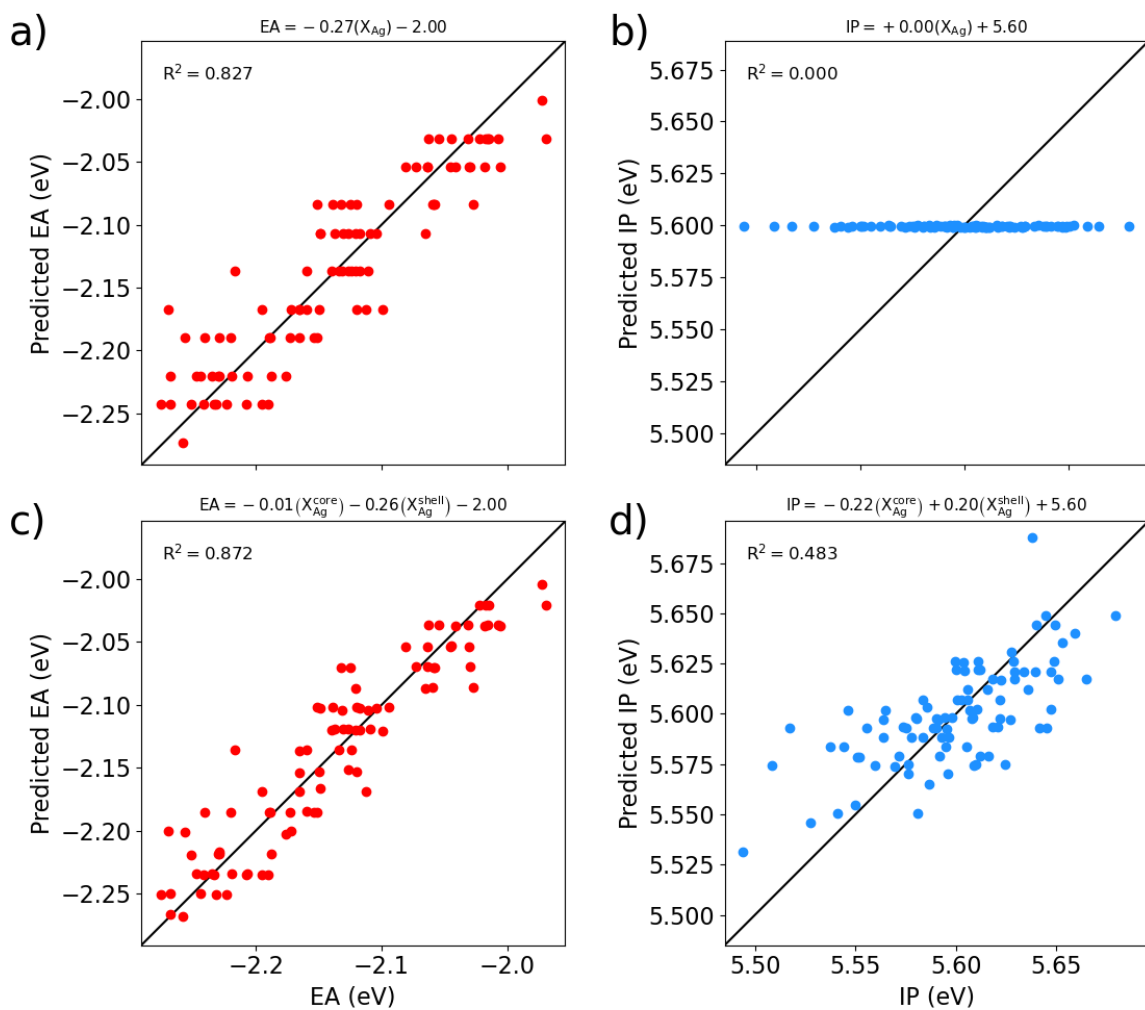


Figure D.2: Comparing X_{Ag} (a, b) to core-shell descriptors (c, d) for capturing EA and IP trends in $M_{36}(SR)_{24}$.

Table D.4: Complete list of values used to parameterize the BCM for TPNCs in Section 4.2. CE_{bulk} for Ag and Au are PBE-calculated values taken from literature.[123]

Parameter	Value	Units
CN_{bulk}^{Ag}	12	-
CN_{bulk}^{Au}	12	-
CN_{bulk}^{SR}	2	-
CE_{bulk}^{Ag}	-2.49	eV/atom
CE_{bulk}^{Au}	-2.99	eV/atom
$CE_{bulk}^{SCH_3} = BFE_{(H-SCH_3)}$	-1.91	eV
$CE_{bulk}^{PET} = BFE_{(H-PET)}$	-1.92	eV
$CE_{bulk}^{TBBT} = BFE_{(H-TBBT)}$	-1.47	eV
$\gamma_{(Ag-Au)}$	0.06	-
$\gamma_{(Au-Ag)}$	1.94	-
$\gamma_{(Ag-SCH_3)}$	1.58	-
$\gamma_{(SCH_3-Ag)}$	0.42	-
$\gamma_{(Au-SCH_3)}$	1.62	-
$\gamma_{(SCH_3-Au)}$	0.38	-
$\gamma_{(Ag-PET)}$	1.55	-
$\gamma_{(PET-Ag)}$	0.45	-
$\gamma_{(Au-PET)}$	1.60	-
$\gamma_{(PET-Au)}$	0.40	-
$\gamma_{(Ag-TBBT)}$	1.78	-
$\gamma_{(TBBT-Ag)}$	0.22	-
$\gamma_{(Au-TBBT)}$	1.86	-
$\gamma_{(TBBT-Au)}$	0.14	-

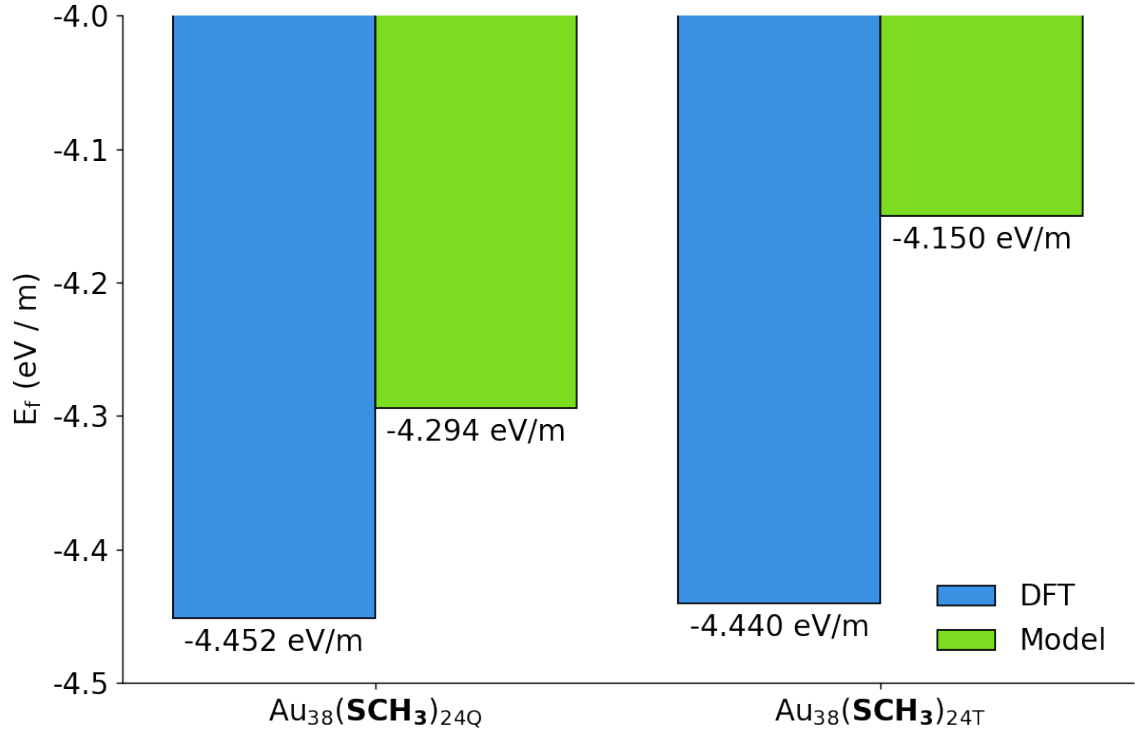


Figure D.3: TPNC formation energy (E_f) of $\text{Au}_{38}(\text{SR})_{24}$ isomers, Q (left) and T (right), protected by SCH_3 as a theoretical substitution to PET. Blue bars = E_f^{DFT} , Green bars = E_f^{model} .

Bibliography

- [1] Q. Yao, T. Chen, X. Yuan, and J. Xie. Toward Total Synthesis of Thiolate-Protected Metal Nanoclusters. *Accounts of Chemical Research*, 51(6):1338–1348, 2018.
- [2] Tu Le, V. Chandana Epa, Frank R. Burden, and David A. Winkler. Quantitative Structure–Property Relationship Modeling of Diverse Materials Properties. *Chemical Reviews*, 112(5):2889–2919, 2012.
- [3] R. Jin, C. Zeng, M. Zhou, and Y. Chen. Atomically Precise Colloidal Metal Nanoclusters and Nanoparticles: Fundamentals and Opportunities. *Chemical Reviews*, 116(18):10346–413, 2016.
- [4] R. Jin. Atomically precise metal nanoclusters: stable sizes and optical properties. *Nanoscale*, 7(5):1549–65, 2015.
- [5] Xi Kang, Yingwei Li, Manzhou Zhu, and Rongchao Jin. Atomically precise alloy nanoclusters: syntheses, structures, and properties. *Chemical Society Reviews*, 49(17):6443–6514, 2020.
- [6] Chenjie Zeng, Yuxiang Chen, Kristin Kirschbaum, Kannatassen Appavoo, Matthew Y. Sfeir, and Rongchao Jin. Structural patterns at all scales in a nonmetallic chiral Au₁₃₃(SR)₅₂ nanoparticle. *Science Advances*, 1(2):e1500045, 2015.
- [7] M. Zhou, T. Higaki, G. Hu, M. Y. Sfeir, Y. Chen, D. E. Jiang, and R. Jin. Three-orders-of-magnitude variation of carrier lifetimes with crystal phase of gold nanoclusters. *Science*, 364(6437):279–282, 2019.
- [8] S. Knoppe, H. Hakkinen, T. Verbiest, and K. Clays. Role of Donor and Acceptor Substituents on the Nonlinear Optical Properties of Gold Nanoclusters. *Journal of Physical Chemistry C*, 122(7):4019–4028, 2018.
- [9] K. Kwak and D. Lee. Electrochemistry of Atomically Precise Metal Nanoclusters. *Accounts of Chemical Research*, 52(1):12–22, 2019.
- [10] Muhammad A. Abbas, Prashant V. Kamat, and Jin Ho Bang. Thiolated Gold Nanoclusters for Light Energy Conversion. *ACS Energy Letters*, 3(4):840–854, 2018.

- [11] Yu Su, Tiantian Xue, Yuxin Liu, Jinxia Qi, Rongchao Jin, and Zhenkun Lin. Luminescent metal nanoclusters for biomedical applications. *Nano Research*, 12(6):1251–1265, 2019.
- [12] S. Chattoraj, M. A. Amin, S. Mohapatra, S. Ghosh, and K. Bhattacharyya. Cancer Cell Imaging Using in Situ Generated Gold Nanoclusters. *ChemPhysChem*, 17(1):61–8, 2016.
- [13] X. Jiang, X. Wang, C. Yao, S. Zhu, L. Liu, R. Liu, and L. Li. Surface-Engineered Gold Nanoclusters with Biological Assembly-Amplified Emission for Multimode Imaging. *Journal of Physical Chemistry Letters*, 10(17):5237–5243, 2019.
- [14] D. Li, B. Kumari, J. M. Makabenta, A. Gupta, and V. Rotello. Effective detection of bacteria using metal nanoclusters. *Nanoscale*, 11(46):22172–22181, 2019.
- [15] Y. Du, H. Sheng, D. Astruc, and M. Zhu. Atomically Precise Noble Metal Nanoclusters as Efficient Catalysts: A Bridge between Structure and Properties. *Chemical Reviews*, 120(2):526–622, 2020.
- [16] G. Li, C. Zeng, and R. Jin. Thermally robust Au₉₉(SPh)₄₂ nanoclusters for chemoselective hydrogenation of nitrobenzaldehyde derivatives in water. *Journal of the American Chemical Society*, 136(9):3673–9, 2014.
- [17] C. Liu, X. Ren, F. Lin, X. Fu, X. Lin, T. Li, K. Sun, and J. Huang. Structure of the Au_{23-x}Ag_x(S-Adm)₁₅ Nanocluster and Its Application for Photocatalytic Degradation of Organic Pollutants. *Angewandte Chemie (International Edition)*, 58(33):11335–11339, 2019.
- [18] Shuo Zhao, Renxi Jin, and Rongchao Jin. Opportunities and Challenges in CO₂ Reduction by Gold- and Silver-Based Electrocatalysts: From Bulk Metals to Nanoparticles and Atomically Precise Nanoclusters. *ACS Energy Letters*, 3(2):452–462, 2018.
- [19] Mathias Brust, Merryll Walker, Donald Bethell, David J. Schiffrin, and Robin Whyman. Synthesis of thiol-derivatised gold nanoparticles in a two-phase Liquid–Liquid system. *Journal of the Chemical Society, Chemical Communications*, 0(7):801–802, 1994.
- [20] T. Gregory Schaaff, Grady Knight, Marat N. Shafigullin, Raymond F. Borkman, and Robert L. Whetten. Isolation and Selected Properties of a 10.4 kDa Gold:Glutathione Cluster Compound. *The Journal of Physical Chemistry B*, 102(52):10643–10646, 1998.

- [21] T. Gregory Schaaff and Robert L. Whetten. Giant Gold-Glutathione Cluster Compounds: Intense Optical Activity in Metal-Based Transitions. *The Journal of Physical Chemistry B*, 104(12):2630–2641, 2000.
- [22] Yuichi Negishi, Katsuyuki Nobusada, and Tatsuya Tsukuda. Glutathione-Protected Gold Clusters Revisited: Bridging the Gap between Gold(I)-Thiolate Complexes and Thiolate-Protected Gold Nanocrystals. *Journal of the American Chemical Society*, 127(14):5261–5270, 2005.
- [23] Pablo D. Jadzinsky, Guillermo Calero, Christopher J. Ackerson, David A. Bushnell, and Roger D. Kornberg. Structure of a Thiol Monolayer-Protected Gold Nanoparticle at 1.1 Å Resolution. *Science*, 318(5849):430, 2007.
- [24] Manzhou Zhu, Christine M. Aikens, Frederick J. Hollander, George C. Schatz, and Rongchao Jin. Correlating the Crystal Structure of A Thiol-Protected Au₂₅ Cluster and Optical Properties. *Journal of the American Chemical Society*, 130(18):5883–5885, 2008.
- [25] Manzhou Zhu, William T. Eckenhoff, Tomislav Pintauer, and Rongchao Jin. Conversion of Anionic [Au₂₅(SCH₂CH₂Ph)₁₈][−] cluster to charge neutral cluster via air oxidation.
- [26] Huifeng Qian, William T. Eckenhoff, Yan Zhu, Tomislav Pintauer, and Rongchao Jin. Total Structure Determination of Thiolate-Protected Au₃₈ Nanoparticles. *Journal of the American Chemical Society*, 132(24):8280–8281, 2010.
- [27] Chenjie Zeng, Huifeng Qian, Tao Li, Gao Li, Nathaniel L. Rosi, Bokwon Yoon, Robert N. Barnett, Robert L. Whetten, Uzi Landman, and Rongchao Jin. Total Structure and Electronic Properties of the Gold Nanocrystal Au₃₆(SR)₂₄. *Angewandte Chemie (International Edition)*, 51(52):13114–13118, 2012.
- [28] Rongchao Jin, Huifeng Qian, Zhikun Wu, Yan Zhu, Manzhou Zhu, Ashok Mohanty, and Niti Garg. Size Focusing: A Methodology for Synthesizing Atomically Precise Gold Nanoclusters. *The Journal of Physical Chemistry Letters*, 1(19):2903–2910, 2010.
- [29] Y. Chen, C. Zeng, D. R. Kauffman, and R. Jin. Tuning the Magic Size of Atomically Precise Gold Nanoclusters via Isomeric Methylbenzenethiols. *Nano Letters*, 15(5):3603–3609, 2015.

- [30] T. Higaki, Q. Li, M. Zhou, S. Zhao, Y. Li, S. Li, and R. Jin. Toward the Tailoring Chemistry of Metal Nanoclusters for Enhancing Functionalities. *Accounts of Chemical Research*, 51(11):2764–2773, 2018.
- [31] Joani Mato and Emilie B. Guidez. Accuracy of the PM6 and PM7 Methods on Bare and Thiolate-Protected Gold Nanoclusters. *The Journal of Physical Chemistry A*, 124(13):2601–2615, 2020.
- [32] A. V. Nagarajan, R. Juarez-Mosqueda, M. J. Cowan, R. Jin, D. R. Kauffman, and G. Mpourmpakis. Elucidating the stability of ligand-protected au nanoclusters under electrochemical reduction of CO_2 . *SN Applied Sciences*, 2:680, 2020.
- [33] Hannu Häkkinen, Michael Walter, and Henrik Grönbeck. Divide and Protect: Capping Gold Nanoclusters with Molecular Gold-Thiolate Rings. *Journal of Physical Chemistry B*, 110(20):9927–9931, 2006.
- [34] Shuang Chen, Lin Xiong, Shuxin Wang, Zhongyun Ma, Shan Jin, Hongting Sheng, Yong Pei, and Manzhou Zhu. Total Structure Determination of $\text{Au}_{21}(\text{S-Adm})_{15}$ and Geometrical/Electronic Structure Evolution of Thiolated Gold Nanoclusters. *Journal of the American Chemical Society*, 138(34):10754–10757, 2016.
- [35] David Crasto, Sami Malola, Grace Brofsky, Amala Dass, and Hannu Häkkinen. Single Crystal XRD Structure and Theoretical Analysis of the Chiral $\text{Au}_{30}\text{S}(\text{S-}t\text{-Bu})_{18}$ Cluster. *Journal of the American Chemical Society*, 136(13):5000–5005, 2014.
- [36] Chao Liu, Tao Li, Gao Li, Katsuyuki Nobusada, Chenjie Zeng, Guangsheng Pang, Nathaniel L. Rosi, and Rongchao Jin. Observation of Body-Centered Cubic Gold Nanocluster. *Angewandte Chemie (International Edition)*, 54(34):9826–9829, 2015.
- [37] Zibao Gan, Jishi Chen, Juan Wang, Chengming Wang, Man-Bo Li, Chuanhao Yao, Shengli Zhuang, An Xu, Lingling Li, and Zhikun Wu. The fourth crystallographic closest packing unveiled in the gold nanocluster crystal. *Nature Communications*, 8(1):14739, 2017.
- [38] Chenjie Zeng, Chong Liu, Yuxiang Chen, Nathaniel L. Rosi, and Rongchao Jin. Gold-Thiolate Ring as a Protecting Motif in the $\text{Au}_{20}(\text{SR})_{16}$ Nanocluster and Implications. *Journal of the American Chemical Society*, 136(34):11922–11925, 2014.

- [39] D. E. Jiang, M. L. Tiago, W. Luo, and S. Dai. The “staple” motif: a key to stability of thiolate-protected gold nanoclusters. *Journal of the American Chemical Society*, 130(9):2777–9, 2008.
- [40] Amala Dass. Nano-scaling law: geometric foundation of thiolated gold nanomolecules. *Nanoscale*, 4(7):2260–2263, 2012.
- [41] N. A. Sakthivel and A. Dass. Aromatic Thiolate-Protected Series of Gold Nanomolecules and a Contrary Structural Trend in Size Evolution. *Accounts of Chemical Research*, 51(8):1774–1783, 2018.
- [42] M. Rambukwella, N. A. Sakthivel, J. H. Delcamp, L. Sementa, A. Fortunelli, and A. Dass. Ligand Structure Determines Nanoparticles’ Atomic Structure, Metal-Ligand Interface and Properties. *Frontiers in Chemistry*, 6:330, 2018.
- [43] M. Walter, J. Akola, O. Lopez-Acevedo, P. D. Jadzinsky, G. Calero, C. J. Ackerson, R. L. Whetten, H. Gronbeck, and H. Hakkinen. A unified view of ligand-protected gold clusters as superatom complexes. *Proceedings of the National Academy of Sciences*, 105(27):9157–62, 2008.
- [44] Anindita Das, Tao Li, Katsuyuki Nobusada, Chenjie Zeng, Nathaniel L. Rosi, and Rongchao Jin. Nonsuperatomic $[\text{Au}_{23}(\text{SC}_6\text{H}_{11})_{16}]^-$ Nanocluster Featuring Bipyramidal Au_{15} Kernel and Trimeric $\text{Au}_3(\text{SR})_4$ Motif. *Journal of the American Chemical Society*, 135(49):18264–18267, 2013.
- [45] Michael G. Taylor and Giannis Mpourmpakis. Thermodynamic Stability of Ligand-Protected Metal Nanoclusters. *Nature Communications*, 8:15988, 2017.
- [46] W. Fei, S. Antonello, T. Dainese, A. Dolmella, M. Lahtinen, K. Rissanen, A. Venzo, and F. Maran. Metal Doping of $\text{Au}_{25}(\text{SR})_{18}^-$ Clusters: Insights and Hintsights. *Journal of the American Chemical Society*, 141(40):16033–16045, 2019.
- [47] Yingwei Li, Tian-Yi Luo, Meng Zhou, Yongbo Song, Nathaniel L. Rosi, and Rongchao Jin. A Correlated Series of Au/Ag Nanoclusters Revealing the Evolutionary Patterns of Asymmetric Ag Doping. *Journal of the American Chemical Society*, 140(43):14235–14243, 2018.
- [48] J. Dean, M. J. Cowan, J. Estes, M. Ramadan, and G. Mpourmpakis. Rapid prediction of bimetallic mixing behavior at the nanoscale. *ACS Nano*, 14:8171–8180, 2020.

- [49] S. Hossain, T. Ono, M. Yoshioka, G. Hu, M. Hosoi, Z. Chen, L. V. Nair, Y. Niihori, W. Kurashige, D. E. Jiang, and Y. Negishi. Thiolate-Protected Trimetallic Au₂₀Ag₄Pd and Au₂₀Ag₄Pt Alloy Clusters with Controlled Chemical Composition and Metal Positions. *Journal of Physical Chemistry Letters*, 9(10):2590–2594, 2018.
- [50] Michael G. Taylor and Giannis Mpourmpakis. Rethinking Heterometal Doping in Ligand-Protected Metal Nanoclusters. *The Journal of Physical Chemistry Letters*, 9(23):6773–6778, 2018.
- [51] M. J. Cowan and G. Mpourmpakis. Structure-property relationships on thiolate-protected gold nanoclusters. *Nanoscale Advances*, 1:184–188, 2019.
- [52] A. Das, C. Liu, H. Y. Byun, K. Nobusada, S. Zhao, N. Rosi, and R. Jin. Structure determination of [Au₁₈(SR)₁₄]. *Angewandte Chemie (International Edition)*, 54(10):3140–4, 2015.
- [53] A. Das, T. Li, G. Li, K. Nobusada, C. Zeng, N. L. Rosi, and R. Jin. Crystal structure and electronic properties of a thiolate-protected Au₂₄ nanocluster. *Nanoscale*, 6(12):6458–62, 2014.
- [54] C. Zeng, T. Li, A. Das, N. L. Rosi, and R. Jin. Chiral Structure of Thiolate-Protected 28-Gold-Atom Nanocluster Determined by X-ray Crystallography. *Journal of the American Chemical Society*, 135(27):10011–10013, 2013.
- [55] Shubo Tian, Yi-Zhi Li, Man-Bo Li, Jinyun Yuan, Jinlong Yang, Zhikun Wu, and Rongchao Jin. Structural isomerism in gold nanoparticles revealed by X-ray crystallography. *Nature Communications*, 6:8667, 2015.
- [56] C. Zeng, Y. Chen, C. Liu, K. Nobusada, N. L. Rosi, and R. Jin. Gold tetrahedra coil up: Kekule-like and double helical superstructures. *Science Advances*, 1(9):e1500425, 2015.
- [57] S. Vergara, D. A. Lukes, M. W. Martynowycz, U. Santiago, G. Plascencia-Villa, S. C. Weiss, M. J. de la Cruz, D. M. Black, M. M. Alvarez, X. Lopez-Lozano, C. O. Barnes, G. Lin, H. C. Weissker, R. L. Whetten, T. Gonen, M. J. Yacaman, and G. Calero. MicroED Structure of Au₁₄₆(p-MBA)₅₇ at Subatomic Resolution Reveals a Twinned FCC Cluster. *Journal of Physical Chemistry Letters*, 8(22):5523–5530, 2017.

- [58] C. J. Zeng, Y. X. Chen, K. Kirschbaum, K. J. Lambright, and R. C. Jin. Emergence of hierarchical structural complexities in nanoparticles and their assembly. *Science*, 354(6319):1580–1584, 2016.
- [59] N. A. Sakthivel, S. Theivendran, V. Ganeshraj, A. G. Oliver, and A. Dass. Crystal Structure of Faradaurate-279: $\text{Au}_{279}(\text{SPh-}^t\text{Bu})_{84}$ Plasmonic Nanocrystal Molecules. *Journal of the American Chemical Society*, 139(43):15450–15459, 2017.
- [60] John P. Perdew, Kieron Burke, and Matthias Ernzerhof. Generalized Gradient Approximation Made Simple. *Physical Review Letters*, 77(18):3865–3868, 1996. PRL.
- [61] S. Goedecker, M. Teter, and J. Hutter. Separable Dual-Space Gaussian Pseudopotentials. *Physical Review B*, 54(3):1703–1710, 1996. PRB.
- [62] T. D. Kühne, M. Iannuzzi, M. Del Ben, V. V. Rybkin, P. Seewald, F. Stein, T. Laino, R. Z. Khaliullin, O. Schütt, F. Schiffmann, D. Golze, J. Wilhelm, S. Chulkov, M. H. Bani-Hashemian, V. Weber, U. Borštnik, M. Taillefumier, A. S. Jakobovits, A. Lazaro, H. Pabst, T. Müller, R. Schade, M. Guidon, S. Andermatt, N. Holmberg, G. K. Schenter, A. Hehn, A. Bussy, F. Belleflamme, G. Tabacchi, A. Glöß, M. Lass, I. Bethune, C. J. Mundy, C. Plessl, M. Watkins, J. VandeVondele, M. Krack, and J. Hutter. CP2K: An electronic structure and molecular dynamics software package - Quickstep: Efficient and accurate electronic structure calculations. *The Journal of Chemical Physics*, 152(19):194103, 2020.
- [63] I. Chakraborty and T. Pradeep. Atomically Precise Clusters of Noble Metals: Emerging Link between Atoms and Nanoparticles. *Chemical Reviews*, 117(12):8208–8271, 2017.
- [64] Y. Du, H. Sheng, D. Astruc, and M. Zhu. Atomically Precise Noble Metal Nanoclusters as Efficient Catalysts: A Bridge between Structure and Properties. *Chemical Reviews*, 120(2):526–622, 2020.
- [65] Rui Guo and Royce W. Murray. Substituent Effects on Redox Potentials and Optical Gap Energies of Molecule-like $\text{Au}_{38}(\text{SPhX})_{24}$ Nanoparticles. *Journal of the American Chemical Society*, 127(34):12140–12143, 2005.
- [66] Alfredo Tlahuice-Flores, Robert L. Whetten, and Miguel Jose-Yacamán. Ligand Effects on the Structure and the Electronic Optical Properties of Anionic $\text{Au}_{25}(\text{SR})_{18}$ Clusters. *Journal of Physical Chemistry C*, 117(40):20867–20875, 2013.

- [67] Wen Wu Xu and Yi Gao. Unraveling the Atomic Structures of the $\text{Au}_{68}(\text{SR})_{34}$ Nanoparticles. *The Journal of Physical Chemistry C*, 119(25):14224–14229, 2015.
- [68] Y. Chen, C. Zeng, C. Liu, K. Kirschbaum, C. Gayathri, R. R. Gil, N. L. Rosi, and R. Jin. Crystal Structure of Barrel-Shaped Chiral $\text{Au}_{130}(\text{p-MBT})_{50}$ Nanocluster. *Journal of the American Chemical Society*, 137(32):10076–9, 2015.
- [69] Y. Li, M. J. Cowan, M. Zhou, Y. Song, T. Y. Luo, R. Juarez-Mosqueda, H. Wang, N. L. Rosi, G. Mpourmpakis, and R. Jin. Atom-by-atom evolution in adamantanethiolate-protected Au_{21} - Au_{22} - $\text{Au}_{22}\text{Cd}_1$ - Au_{24} nanocluster series. *Journal of the American Chemical Society*, 142:20426–20433, 2020.
- [70] Florian Weigend, Marco Häser, Holger Patzelt, and Reinhart Ahlrichs. RI-MP2: optimized auxiliary basis sets and demonstration of efficiency. *Chemical Physics Letters*, 294(1):143–152, 1998.
- [71] Florian Weigend and Marco Häser. RI-MP2: first derivatives and global consistency. *Theoretical Chemistry Accounts*, 97(1):331–340, 1997. RI approximation.
- [72] Reinhart Ahlrichs, Michael Bär, Marco Häser, Hans Horn, and Christoph Kölmel. Electronic structure calculations on workstation computers: The program system turbomole. *Chemical Physics Letters*, 162(3):165–169, 1989.
- [73] Chenjie Zeng, Yuxiang Chen, Kenji Iida, Katsuyuki Nobusada, Kristin Kirschbaum, Kelly J. Lambright, and Rongchao Jin. Gold Quantum Boxes: On the Periodicities and the Quantum Confinement in the Au_{28} , Au_{36} , Au_{44} , and Au_{52} Magic Series. *Journal of the American Chemical Society*, 138(12):3950–3953, 2016.
- [74] Z. Luo, V. Nachammai, B. Zhang, N. Yan, D. T. Leong, D. E. Jiang, and J. Xie. Toward understanding the growth mechanism: tracing all stable intermediate species from reduction of $\text{Au}(\text{I})$ -thiolate complexes to evolution of Au_{25} nanoclusters. *Journal of the American Chemical Society*, 136(30):10577–80, 2014.
- [75] T. Dainese, S. Antonello, S. Bogialli, W. Fei, A. Venzo, and F. Maran. Gold Fusion: From $\text{Au}_{25}(\text{SR})_{18}$ to $\text{Au}_{38}(\text{SR})_{24}$, the Most Unexpected Transformation of a Very Stable Nanocluster. *ACS Nano*, 12(7):7057–7066, 2018.
- [76] Giannis Mpourmpakis, Stavros Caratzoulas, and Dionisios G. Vlachos. What Controls Au Nanoparticle Dispersity during Growth? *Nano Letters*, 10(9):3408–3413, 2010.

- [77] Yong Jiang, Yuanyuan Huang, Hao Cheng, Qinghua Liu, Zhi Xie, Tao Yao, Zheng Jiang, Yuying Huang, Qing Bian, Guoqiang Pan, Zhihu Sun, and Shiqiang Wei. Solvent Influence on the Role of Thiols in Growth of Thiols-Capped Au Nanocrystals. *The Journal of Physical Chemistry C*, 118(1):714–719, 2014.
- [78] N. Yan, N. Xia, L. Liao, M. Zhu, F. Jin, R. Jin, and Z. Wu. Unraveling the long-pursued Au₁₄₄ structure by x-ray crystallography. *Science Advances*, 4(10):eaat7259, 2018.
- [79] Tatsuya Higaki, Chong Liu, Chenjie Zeng, Renxi Jin, Yuxiang Chen, Nathaniel L. Rosi, and Rongchao Jin. Controlling the Atomic Structure of Au₃₀ Nanoclusters by a Ligand-Based Strategy. *Angewandte Chemie International Edition*, 55(23):6694–6697, 2016.
- [80] Huifeng Qian, Matthew Y. Sfeir, and Rongchao Jin. Ultrafast Relaxation Dynamics of [Au₂₅(SR)₁₈]^q Nanoclusters: Effects of Charge State. *The Journal of Physical Chemistry C*, 114(47):19935–19940, 2010.
- [81] Victor Berry Michael. Quantal phase factors accompanying adiabatic changes. *Proceedings of the Royal Society of London. A. Mathematical and Physical Sciences*, 392(1802):45–57, 1984.
- [82] Nicola Marzari and David Vanderbilt. Maximally localized generalized Wannier functions for composite energy bands. *Physical Review B*, 56(20):12847–12865, 1997. PRB.
- [83] Anna Putrino, Daniel Sebastiani, and Michele Parrinello. Generalized variational density functional perturbation theory. *The Journal of Chemical Physics*, 113(17):7102–7109, 2000.
- [84] Kenneth J. Miller. Calculation of the molecular polarizability tensor. *Journal of the American Chemical Society*, 112(23):8543–8551, 1990.
- [85] M. Gussoni, M. Rui, and G. Zerbi. Electronic and relaxation contribution to linear molecular polarizability. An analysis of the experimental values. *Journal of Molecular Structure*, 447(3):163–215, 1998.
- [86] C. M. Hansen. *Hansen Solubility Parameters: A User’s Handbook, 2nd ed.* CRC Press, Boca Raton, FL, 2007.

- [87] M. J. Cowan, T. Higaki, R. Jin, and G. Mpourmpakis. Understanding the solubility behavior of atomically precise gold nanoclusters. *The Journal of Physical Chemistry C*, 123:20006–20012, 2019.
- [88] Paolo Pengo, Cristian Bazzo, Mariangela Boccalon, and Lucia Pasquato. Differential reactivity of the inner and outer positions of $\text{Au}_{25}(\text{SCH}_2\text{CH}_2\text{Ph})_{18}$ dimeric staples under place exchange conditions. *Chemical Communications*, 51(15):3204–3207, 2015.
- [89] M. Zhou, C. Zeng, M. Y. Sfeir, M. Cotlet, K. Iida, K. Nobusada, and R. Jin. Evolution of Excited-State Dynamics in Periodic Au_{28} , Au_{36} , Au_{44} , and Au_{52} Nanoclusters. *Journal of Physical Chemistry Letters*, 8(17):4023–4030, 2017.
- [90] Huayan Yang, Yu Wang, Alison J. Edwards, Juanzhu Yan, and Nanfeng Zheng. High-yield synthesis and crystal structure of a green Au_{30} cluster co-capped by thiolate and sulfide. *Chemical Communications*, 50(92):14325–14327, 2014.
- [91] Amala Dass, Shevanuja Theivendran, Praneeth Reddy Nimmala, Chanaka Kumara, Vijay Reddy Jupally, Alessandro Fortunelli, Luca Sementa, Giovanni Barcaro, Xiaobing Zuo, and Bruce C. Noll. $\text{Au}_{133}(\text{SPh-tBu})_{52}$ Nanomolecules: X-ray Crystallography, Optical, Electrochemical, and Theoretical Analysis. *Journal of the American Chemical Society*, 137(14):4610–4613, 2015.
- [92] M. A. Tofanelli, K. Salorinne, T. W. Ni, S. Malola, B. Newell, B. Phillips, H. Hakkinen, and C. J. Ackerson. Jahn-Teller effects in $\text{Au}_{25}(\text{SR})_{18}$. *Chem Sci*, 7(3):1882–1890, 2016.
- [93] J. Zhu, X. Ou, J. Su, and J. Li. The impacts of surface polarity on the solubility of nanoparticle. *Journal of Chemical Physics*, 145(4):044504, 2016.
- [94] X. Kang, H. Chong, and M. Zhu. $\text{Au}_{25}(\text{SR})_{18}$: the captain of the great nanocluster ship. *Nanoscale*, 10(23):10758–10834, 2018.
- [95] Mortimer J. Kamlet, Ruth M. Doherty, R. W. Taft, Michael H. Abraham, and William J. Koros. Solubility properties in polymers and biological mediums. 3. Predictional methods for critical temperatures, boiling points, and solubility properties (RG values) based on molecular size, polarizability, and dipolarity. *Journal of the American Chemical Society*, 106(5):1205–1212, 1984.
- [96] Peter J. Dyer, Hugh Docherty, and Peter T. Cummings. The importance of polarizability in the modeling of solubility: Quantifying the effect of solute polarizability on

- the solubility of small nonpolar solutes in popular models of water. *The Journal of Chemical Physics*, 129(2):024508, 2008.
- [97] Cao Chenzhong and Li Zhiliang. Molecular polarizability. 1. relationship to water solubility of alkanes and alcohols. *Journal of Chemical Information and Computer Sciences*, 38(1):1–7, 1998.
 - [98] Chakra P. Joshi, Megalamane S. Bootharaju, Mohammad J. Alhilaly, and Osman M. Bakr. $[\text{Ag}_{25}(\text{SR})_{18}]^-$: The “Golden” Silver Nanoparticle. *Journal of the American Chemical Society*, 137(36):11578–11581, 2015.
 - [99] P. Chakraborty, A. Nag, A. Chakraborty, and T. Pradeep. Approaching materials with atomic precision using supramolecular cluster assemblies. *Accounts of Chemical Research*, 52(1):2–11, 2019.
 - [100] Z. Tang, N. A. Kotov, and M. Giersig. Spontaneous organization of single CdTe nanoparticles into luminescent nanowires. *Science*, 297(5579):237–240, 2002.
 - [101] Y. Li, M. J. Cowan, M. Zhou, M. G. Taylor, H. Wang, Y. Song, G. Mpourmpakis, and R. Jin. Heterometal-doped m_{23} ($\text{m} = \text{au/ag/cd}$) nanoclusters with large dipole moments. *ACS Nano*, 14:6599–6606, 2020.
 - [102] Alan E. Reed, Robert B. Weinstock, and Frank Weinhold. Natural population analysis. *The Journal of Chemical Physics*, 83(2):735–746, 1985.
 - [103] G. Panapitiya, G. Avendano-Franco, P. Ren, X. Wen, Y. Li, and J. P. Lewis. Machine-Learning Prediction of CO Adsorption in Thiolated, Ag-Alloyed Au Nanoclusters. *Journal of the American Chemical Society*, 140(50):17508–17514, 2018.
 - [104] Xiao Cai, Weigang Hu, Shun Xu, Dan Yang, Mingyang Chen, Miao Shu, Rui Si, Weiping Ding, and Yan Zhu. Structural relaxation enabled by internal vacancy available in a 24-atom gold cluster reinforces catalytic reactivity. *Journal of the American Chemical Society*, 142(9):4141–4153, 2020.
 - [105] Naga Arjun Sakthivel, Luca Sementa, Bokwon Yoon, Uzi Landman, Alessandro Fortunelli, and Amala Dass. Isomeric thiolate monolayer protected au_{92} and au_{102} nanomolecules. *The Journal of Physical Chemistry C*, 124(2):1655–1666, 2020.
 - [106] David Crasto, Giovanni Barcaro, Mauro Stener, Luca Sementa, Alessandro Fortunelli, and Amala Dass. $\text{Au}_{24}(\text{SAdm})_{16}$ Nanomolecules: X-ray Crystal Structure, Theo-

- retical Analysis, Adaptability of Adamantane Ligands to Form Au₂₃(SAdm)₁₆ and Au₂₅(SAdm)₁₆, and Its Relation to Au₂₅(SR)₁₈. *Journal of the American Chemical Society*, 136(42):14933–14940, 2014.
- [107] Tatsuya Higaki, Meng Zhou, Kelly J. Lambright, Kristin Kirschbaum, Matthew Y. Sfeir, and Rongchao Jin. Sharp Transition from Nonmetallic Au₂₄₆ to Metallic Au₂₇₉ with Nascent Surface Plasmon Resonance. *Journal of the American Chemical Society*, 140(17):5691–5695, 2018.
- [108] Kaiyuan Zheng and Jianping Xie. Composition-Dependent Antimicrobial Ability of Full-Spectrum Au_xAg_{25-x} Alloy Nanoclusters. *ACS Nano*, 14(9):11533–11541, 2020.
- [109] Shuxin Wang, Qi Li, Xi Kang, and Manzhou Zhu. Customizing the structure, composition, and properties of alloy nanoclusters by metal exchange. *Accounts of Chemical Research*, 51(11):2784–2792, 2018.
- [110] Tatsuya Higaki, Chong Liu, David J. Morris, Guiying He, Tian-Yi Luo, Matthew Y. Sfeir, Peng Zhang, Nathaniel L. Rosi, and Rongchao Jin. Au_{130-x}Ag_x Nanoclusters with Non-Metallicity: A Drum of Silver-Rich Sites Enclosed in a Marks-Decahedral Cage of Gold-Rich Sites. *Angewandte Chemie International Edition*, 58(52):18798–18802, 2019.
- [111] M. Uda, A. Nakamura, T. Yamamoto, and Y. Fujimoto. Work function of polycrystalline ag, au and al. *Journal of Electron Spectroscopy and Related Phenomena*, 88-91:643–648, 1998. Proceedings of the Seventh International Conference on Electron Spectroscopy.
- [112] J. McKay, M. J. Cowan, and G. Mpourmpakis. Predicting ligand removal energetics in thiolate-protected nanoclusters from molecular complexes. *Nanoscale*, 13:2034–2043, 2021.
- [113] Ji Luo, Zeng Quan Xue, Wei Min Liu, Jin Lei Wu, and Zhong Qin Yang. Koopmans’ theorem for large molecular systems within density functional theory. *The Journal of Physical Chemistry A*, 110(43):12005–12009, 2006.
- [114] Yingwei Li, Michael G. Taylor, Tian-Yi Luo, Yongbo Song, Nathaniel L. Rosi, Giannis Mpourmpakis, and Rongchao Jin. Heteroatom tracing reveals the 30-atom au–ag bimetallic nanocluster as a dimeric structure. *The Journal of Physical Chemistry Letters*, 11(17):7307–7312, 2020.

- [115] Rosalba Juarez-Mosqueda and Giannis Mpourmpakis. Elucidating the optical spectra of [Au₂₅(SR)₁₈]Q nanoclusters. *Phys. Chem. Chem. Phys.*, 21:22272–22282, 2019.
- [116] Thomas Bürgi. Properties of the gold–sulphur interface: from self-assembled monolayers to clusters. *Nanoscale*, 7:15553–15567, 2015.
- [117] Site Li, Dominic Alfonso, Anantha Venkataraman Nagarajan, Stephen D. House, Judith C. Yang, Douglas R. Kauffman, Giannis Mpourmpakis, and Rongchao Jin. Monopalladium Substitution in Gold Nanoclusters Enhances CO₂ Electroreduction Activity and Selectivity. *ACS Catalysis*, 10(20):12011–12016, 2020.
- [118] Qi Li, Tian-Yi Luo, Michael G. Taylor, Shuxin Wang, Xiaofan Zhu, Yongbo Song, Giannis Mpourmpakis, Nathaniel L. Rosi, and Rongchao Jin. Molecular “surgery” on a 23-gold-atom nanoparticle. *Science Advances*, 3(5):e1603193, 2017.
- [119] M. J. Cowan, A. V. Nagarajan, and G. Mpourmpakis. Correlating structural rules with electronic properties of ligand-protected alloy nanoclusters. *Journal of Chemical Physics*, 155:024303, 2021.
- [120] Zihao Yan, Michael G. Taylor, Ashley Mascareno, and Giannis Mpourmpakis. Size-, shape-, and composition-dependent model for metal nanoparticle stability prediction. *Nano Letters*, 18(4):2696–2704, 2018.
- [121] Shengli Zhuang, Lingwen Liao, Man-Bo Li, Chuanhao Yao, Yan Zhao, Hongwei Dong, Jin Li, Haiteng Deng, Lingling Li, and Zhikun Wu. The fcc structure isomerization in gold nanoclusters. *Nanoscale*, 9:14809–14813, 2017.
- [122] Lingwen Liao, Chengming Wang, Shengli Zhuang, Nan Yan, Yan Zhao, Ying Yang, Jin Li, Haiteng Deng, and Zhikun Wu. An Unprecedented Kernel Growth Mode and the Layer-Number-Order-Dependent Properties in Gold Nanoclusters. *Angewandte Chemie International Edition*, 59(2):731–734, 2020.
- [123] Patanachai Janthon, Sijie (Andy) Luo, Sergey M. Kozlov, Francesc Viñes, Jumras Limtrakul, Donald G. Truhlar, and Francesc Illas. Bulk properties of transition metals: A challenge for the design of universal density functionals. *Journal of Chemical Theory and Computation*, 10(9):3832–3839, 2014.